

國立交通大學

機械工程學系

碩士論文

具單個或雙個斜葉圓盤渦輪攪拌槽流場分析

Flow Analysis of Stirred Tanks with Single or
Dual Pitched-Blade Disc Turbine

研究生：林士超

指導教授：崔燕勇

中華民國九十五年七月

具單個或雙個斜葉圓盤渦輪攪拌槽流場分析

Flow Analysis of Stirred Tanks with Single or Dual Pitched-Blade
Disc Turbine

研 究 生：林士超

Student: Shih-Chao Lin

指導教授：崔燕勇

Advisor: Yeng-Yung Tsui

國立交通大學

機械工程學系

碩士論文



Submitted to Institute of Mechanical Engineering

College of Engineering

National Chiao Tung University

In Partial Fulfillment of the Requirements

for the Degree of

Master of Science

in

Mechanical Engineering

July, 2006

Hsinchu, Taiwan, Republic of China

中華民國九十五年七月

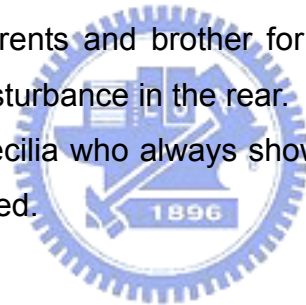
Acknowledgements

I would like to express gratitude to Prof. Yeng-Yung Tsui for his patience, suggestions and criticisms during this two years not only on the study but also on ways of getting along with people.

Thanks to the Doctoral Candidate, Yu-Chang Hu, for his teaching and helping on the program. I would like to appreciate George and Ching-Shiang Yang who encourage me to study hard. Thanks to Dong-Ting Cheng for his assistance in Lab finance and thanks to Eatrol and Just for their friendships.

I am grateful to my parents and brother for all that they had done. With their support, I have no fear of disturbance in the rear.

I would like to thank Cecilia who always shows consideration for me and be my listener when I was depressed.



Flow Analysis of Stirred Tanks with Single or Dual Pitched-Blade Disc Turbine

Student: Shis-Chou Lin

Advisor: Dr. Yeng-Yung Tsui

Institute of Mechanical Engineering
National Chiao Tung University

Abstract

This study aimed at the prediction of flow field agitated by single or dual pitched blade disc turbine by Multiple Reference Frame. Pitched blade disc turbine was only used in stirred tank with single impeller. The flow was assumed as quasi-steady state and we applied the Multiple Reference Frame to calculate flow field. Rotational frame was use to calculate flow of impeller swept region, and flow surrounding it; stationary frame was use to calculate flow of the rest region that neat the baffle or the wall. The turbulent model used was High Reynolds $k-\epsilon$ model; wall function is used to calculate the flow near the wall. Because of the axial symmetric of the stirred tank, the computational domain was only half of the tank and periodic boundary was used.

Four parameters were changed to observe the transform of flow field in stirred tanks with single disc turbine. They are oblique angle of the impeller blades, clearance between impeller and vessel bottom, diameter of impeller disc, and diameter of impeller. When the blade angle increased, reaching a specific angle, the flow field changed from axial flow to radial flow rapidly. The significant oblique angle of impeller blade that made the flow field changed was defined as the critical angle. Decrease of the clearance made the critical angle become bigger and the effect of disc also increase. Larger impeller disc and larger impeller made the critical angle smaller. Different definition of MRF from Shen[19] was applied and its results shown good agreement with the experimental data.

MRF technique was also used to predict the flow field of stirred tank agitated by dual impellers. Three stable flow field of stirred tank with dual turbines were predicted, they are parallel flow, merging flow and diverging flow. The prediction results were compared with experimental data and prediction of IO and SG technique. The results show that the MRF technique can predict the flow field agitated by dual impeller, but the power numbers were not good except the parallel flow.

具單個或雙個斜葉圓盤渦輪攪拌槽流場分析

研究生：林士超

指導教授：崔燕勇 博士

國立交通大學機械學系

摘 要

本研究為對具單個或雙個圓盤渦輪的攪拌槽做流場模擬分析，其中在單個渦輪的部份，螺槳葉片將在具有不同角度的情況下計算。假設流場為擬似穩態，應用多重參考座標系，以旋轉座標系計算葉片旋轉區域及其附近之流場，以靜止座標系計算其餘靠近壁面及擋板之流場；紊流模式使用高雷諾數之 $k-\varepsilon$ 模式，對靠近壁面的流場使用壁函數來處理，由於攪拌槽具備軸對稱的特性，故本模擬只取一半的攪拌槽作為計算範圍以減少計算量。

在單渦輪攪拌槽的情況下，改變四種參數以觀察流場的改變，分別是：渦輪葉片的傾斜角度、渦輪距離攪拌槽底的距離、渦輪的直徑以及渦輪圓盤的直徑。當渦輪葉片的角度變逐漸變大(越接近垂直時)，到達某一特定角度時，流場會從軸向流場變成徑向流場，我們稱此特定角度為臨界角。當渦輪與攪拌槽底的間隙越小時臨界角越大，而渦輪碟盤對於流場的影響也越明顯，當渦輪尺寸與渦輪碟盤尺寸越大時，臨界角越小。本研究所定義的多重參考座標系與沈[19]所定義的不同，而本研究與實驗的比對較沈[19]來的好。

多重參考座標系亦應用在雙渦輪圓盤攪拌槽中，模擬雙渦輪攪拌槽中會出現的三個穩定流場，分別是平行流，結合流及分離流；將其與實驗結果、內外交替疊代法(數值模擬)、滑動網格法(數值模擬)比較，發現多重參考座標系能準確的模擬平行流，但是在結合流及分離流方面，雖然流場與實驗結果相似，但是功率數與實驗結果比較卻不甚相同。

Contents

Abstract.....	I
List of Figures.....	VI
Nomenclature.....	X
Chapter 1 introduction.....	1
1.1 Preface.....	1
1.2 Definition of Radial flow and Axial flow.....	2
1.3 Review of previous work.....	2
1.3.1 Experiments.....	2
1.3.2 Numerical modeling.....	7
1.4 Study objective.....	11
Chapter 2 Mathematical Model.....	13
2.1 Basic assumptions.....	13
2.2 The governing equations of the MRF (Multiple Reference Frame) Model.....	13
2.2.1 The govern equation in the stationary frame.....	13
2.2.2 Time-average eddy viscosity turbulent model: the k- ϵ model.....	14
2.2.3 The governing equation in the rotational frame.....	16
2.3 Boundary condition.....	17
2.3.1 Periodic boundary conditions.....	17
2.3.2 Boundary conditions on the solid walls.....	18
Chapter 3 Numerical methods.....	19
3.1 Discretization of governing equations.....	10
3.1.1 Convection term.....	19
3.1.2 Diffusion term.....	20
3.1.3 Source term.....	21
3.1.4 Difference equation.....	22
3.2 Calculation of the rate of flux through control surface.....	23
3.3 Pressure correction equation.....	24
3.4 Boundary condition.....	27
3.4.1 Periodic boundary condition.....	27
3.4.2 Solid wall boundary condition.....	28
3.5 Transformation between rotational frame and stationary frame.....	30
3.6 Solution approach.....	31

Chapter 4 Results and discussion for single impeller.....	33
4.1 Introduction.....	33
4.2 Geometry of stirred tank with single disc turbine.....	33
4.2.1 Comparison with experimental data of Ranade et al...	34
4.2.2 Grid test cases.....	37
4.3 The effects of blade angle on flow pattern for different off-bottom clearance (D=T/3, d=2D/3).....	37
4.3.1 The effects of blade angle on flow patterns when C=T/2 (D=T/3, d=2D/3).....	37
4.3.2 The effects of blade angle on flow patterns when C=T/3 (D=T/3, d=2D/3).....	38
4.3.3 The effects of blade angle on flow patterns when C=T/4 (D=T/3, d=2D/3).....	40
4.3.4 The effects of pitched blade disc turbine position on flow patterns.....	41
4.4 The effects of blade angle on flow pattern for different off-bottom clearance (D=T/3, d=3D/4).....	42
4.4.1 The effects of blade angle on flow patterns when C=T/2 (D=T/3, d=2D/3).....	42
4.4.2 The effects of blade angle on flow patterns when C=T/3 (D=T/3, d=2D/3).....	42
4.4.3 The effects of blade angle on flow patterns when C=T/4 (D=T/3, d=2D/3).....	43
4.4.4 The effects of disc size on flow patterns.....	44
4.5 The effects of blade angle on flow pattern for different off-bottom clearance (D=T/2, d=3D/4).....	45
4.5.1 The effects of blade angle on flow patterns when C=T/2 (D=T/3, d=2D/3).....	45
4.5.2 The effects of blade angle on flow patterns when C=T/3 (D=T/3, d=2D/3).....	45
4.5.3 The effects of blade angle on flow patterns when C=T/2 (D=T/3, d=2D/3).....	46
4.5.4 The effects of impeller diameter on flow patterns....	46
4.6 Discussion.....	47
Chapter 5 Result and discussion for dual impeller.....	50

5.1 Introduction.....	50
5.2 Multiple reference frames.....	50
5.3 The geometry of the stirred tank.....	51
5.4 Result and discussion.....	51
Chapter 6 Conclusion.....	54
Reference.....	56



List of figures

Figure 1.1 Various impellers.....	59
Figure 1.2 Axial flow and radial flow.....	60
Figure 1.3 Flow patterns for three geometry configuration studied.....	61
Figure 1.4 Dual Rushton turbine vessel with variable baffle length.....	62
Figure 1.5 Rotational and stationary frame of Shen's model.....	63
Figure 1.6 Rotational and stationary frame of present work.....	64
Figure 2.1 Periodic boundary conditions.....	65
Figure 3.1 Over-relaxed approach.....	66
Figure 3.2 Calculation of boundary pressure.....	66
Figure 3.3 Calculation of wall shear stress.....	67
Figure 3.4 Calculation grids in rotational frame.....	68
Figure 3.5 Calculation grids in stationary frame.....	68
Figure 4.1 Geometric of single impeller stirred tank.....	69
Figure 4.2 Geometrical parameters of stirred tank.....	70
Figure 4.3 Calculation domain and grids of straight-blade disc turbine.....	71
Figure 4.4 Calculation domain and grids of straight-blade disc turbine.....	72
Figure 4.5 Radial profiles of radial, tangential, and axial velocity compare with prediction of Shen and experimental data of Ranade et al.....	73
Figure 4.6 The position of various Z/R.....	74
Figure 4.7 Radial profiles of radial, tangential, and axial velocity of four kinds of grids.....	75
Figure 4.8 Stream lines of various blade angles at the vertical plane of $\Phi=-30^\circ$ ($D=T/3$ $d=2D/3$ $C=T/2$).....	76
Figure 4.9 The power number, pumping number, and pumping efficiency of various blade angles ($D=T/3$ $d=2D/3$ $C=T/2$).....	77
Figure 4.10 The angular profile of power number and pumping number compare with Shen's work ($D=T/3$ $d=2D/3$ $C=T/2$).....	78
Figure 4.11 The pressure contour of $\alpha=47^\circ$ and $\alpha=48^\circ$ at the vertical plane of $\Phi=-30^\circ$ ($D=T/3$ $d=2D/3$ $C=T/2$).....	79
Figure 4.12 Stream lines of various blade angles at the vertical plane of $\Phi=-30^\circ$ ($D=T/3$ $d=2D/3$ $C=T/3$).....	80
Figure 4.13 The power number, pumping number, and pumping efficiency of various	

blade angles ($D=T/3$ $d=2D/3$ $C=T/3$).....	81
Figure 4.14 The angular profile of power number and pumping number compare with Shen's work ($D=T/3$ $d=2D/3$ $C=T/3$).....	82
Figure 4.15 The pressure contour of $\alpha=72^\circ$ and $\alpha=73^\circ$ at the vertical plane of $\Phi=-30^\circ$ ($D=T/3$ $d=2D/3$ $C=T/3$).....	83
Figure 4.16 Stream lines of various blade angles at the vertical plane of $\Phi=-30^\circ$ ($D=T/3$ $d=2D/3$ $C=T/4$).....	84
Figure 4.17 The power number, pumping number, and pumping efficiency of various blade angles ($D=T/3$ $d=2D/3$ $C=T/4$).....	85
Figure 4.18 The angular profile of power number and pumping number compare with Shen's work ($D=T/3$ $d=2D/3$ $C=T/4$).....	86
Figure 4.19 The pressure contour of $\alpha=88^\circ$ and $\alpha=89^\circ$ at the vertical plane of $\Phi=-30^\circ$ ($D=T/3$ $d=2D/3$ $C=T/4$).....	87
Figure 4.20 The flow field changes from axial flow to radial flow of different impeller location.....	88
Figure 4.21 The flow field of blade angle $\alpha=60^\circ$ when the impeller is posited at three different location.....	89
Figure 4.22 Stream lines of various blade angles at the vertical plane of $\Phi=-30^\circ$ ($D=T/3$ $d=3D/4$ $C=T/2$).....	90
Figure 4.23 The power number, pumping number, and pumping efficiency of various blade angles ($D=T/3$ $d=3D/4$ $C=T/2$).....	91
Figure 4.24 The angular profile of power number and pumping number compare with Shen's work ($D=T/3$ $d=3D/4$ $C=T/2$).....	92
Figure 4.25 The pressure contour of $\alpha=37^\circ$ and $\alpha=38^\circ$ at the vertical plane of $\Phi=-30^\circ$ ($D=T/3$ $d=2D/3$ $C=T/4$).....	93
Figure 4.26 Stream lines of various blade angles at the vertical plane of $\Phi=-30^\circ$ ($D=T/3$ $d=3D/4$ $C=T/3$).....	94
Figure 4.27 The power number, pumping number, and pumping efficiency of various blade angles ($D=T/3$ $d=3D/4$ $C=T/3$).....	95
Figure 4.28 The angular profile of power number and pumping number compare with Shen's work ($D=T/3$ $d=3D/4$ $C=T/3$).....	96
Figure 4.29 The pressure contour of $\alpha=65^\circ$ and $\alpha=66^\circ$ at the vertical plane of $\Phi=-30^\circ$ ($D=T/3$ $d=2D/3$ $C=T/3$).....	97
Figure 4.30 Stream lines of various blade angles at the vertical plane of $\Phi=-30^\circ$	

(D=T/3 d=3D/4 C=T/4).....	98
Figure 4.31 The power number, pumping number, and pumping efficiency of various blade angles (D=T/3 d=3D/4 C=T/4).....	99
Figure 4.32 The angular profile of power number and pumping number compare with Shen's work (D=T/3 d=3D/4 C=T/4).....	100
Figure 4.33 The pressure contour of $\alpha=84^\circ$ and $\alpha=85^\circ$ at the vertical plane of $\Phi=-30^\circ$ (D=T/3 d=2D/3 C=T/4).....	101
Figure 4.34 Stream lines of various blade angles at the vertical plane of $\Phi=-30^\circ$ (D=T/2 d=3D/4 C=T/2).....	102
Figure 4.35 The power number, pumping number, and pumping efficiency of various blade angles (D=T/2 d=3D/4 C=T/2).....	103
Figure 4.36 The angular profile of power number and pumping number compare with Shen's work (D=T/2 d=3D/4 C=T/2).....	104
Figure 4.37 Stream lines of various blade angles at the vertical plane of $\Phi=-30^\circ$ (D=T/2 d=3D/4 C=T/3).....	105
Figure 4.38 The power number, pumping number, and pumping efficiency of various blade angles (D=T/2 d=3D/4 C=T/3).....	106
Figure 4.39 The angular profile of power number and pumping number compare with Shen's work (D=T/2 d=3D/4 C=T/3).....	107
Figure 4.40 Stream lines of various blade angles at the vertical plane of $\Phi=-30^\circ$ (D=T/2 d=3D/4 C=T/4).....	108
Figure 4.41 The power number, pumping number, and pumping efficiency of various blade angles (D=T/2 d=3D/4 C=T/4).....	109
Figure 4.42 The angular profile of power number and pumping number compare with Shen's work (D=T/2 d=3D/4 C=T/4).....	110
Figure 4.43 Flow field behind the blade (D=T/3 d=3D/4 C=T/3).....	111
Figure 4.44 Pressure contours of different blade angles (D=T/3 d=3D/4 C=T/3)....	112
Figure 4.45 Pressure contours on blade surface for different blade angles (D=T/3 d=3D/4 C=T/3).....	113
Figure 4.46 Stream lines on blade surface for different blade angles.....	114
Figure 4.47 The definition of flow out angle.....	115
Figure 4.48 Angular profiles of flow out angle for different off-bottom clearance.....	116
Figure 4.49 Radial profiles of power number for different off-bottom clearance.....	117

Figure 4.50 Radial profiles of pumping number for different off-bottom clearance.....	118
Figure 4.51 Radial profiles of k^* for different off-bottom clearance.....	119
Figure 4.52 Radial profiles of ε^* for different off-bottom clearance....	120
Figure 4.53 Radial profiles of pumping efficiency for different off-bottom clearance.....	121
Figure 4.54 The stream lines and contours of stirred tank at different vertical plane when the blade angle $\alpha=70^\circ$ ($D=T/3$ $d=3D/4$ $C=T/3$).....	122
Figure 5.1 Dual impeller stirred tank configuration.....	123
Figure 5.2 Multiple reference of parallel flow.....	123
Figure 5.3 Multiple reference of merging flow.....	124
Figure 5.4 Multiple reference of diverging flow.....	124
Figure 5.5 Parallel flow: comparison of velocity vector plots in a plane midway between baffles.....	127
Figure 5.6 Parallel flow: comparison of turbulence energy distribution in a plane midway between baffles.....	128
Figure 5.7 Merging flow: comparison of velocity vector plots in a plane midway between baffles.....	129
Figure 5.8 Merging flow: comparison of turbulence energy distribution in a plane midway between baffles.....	130
Figure 5.9 Diverging flow: comparison of velocity vector plots in a plane midway between baffles.....	131
Figure 5.10 Diverging flow: comparison of turbulence energy distribution in a plane midway between baffles.....	132

Nomenclature

a_p, a_c	Coefficient of momentum equation
a_p^p, a_c^p	Coefficient of pressure correction equation
B	Width of baffles
C	Clearance between vertical center plan of impeller and vessel bottom
D	Diameter of impeller disc
D	Diameter of impeller
\vec{e}	Unit vector
F_f	Flux
H	Height of stirred tank
L	Length of impeller blades
\dot{m}	Mass flow rate
N_p	Power number
N_{Q_p}	Pumping number
p	Pressure
Q_ϕ	Source term
R_e	Reynold number
\vec{S}	Normal vector of surface
\vec{S}_f	Normal vector of control volume surfaces
T	Diameter of stirred tank
U	Fluid velocity
U_g	Speed of grid
W	Width of impeller blades
w_p	Weighting factor
α_ϕ, α_p	Relaxation factor
ρ	Density
μ	Viscosity
ΔV	Volume of control volume cell
τ	Wall shear stress
Ω	Angular speed



Suffix

<i>b</i>	Boundary
<i>C</i>	Neighbor cell center
<i>f</i>	Center of control volume face
<i>P</i>	Present cell
<i>w</i>	Wall
Φ	Variable

Superscript

<i>c</i>	Convection term
<i>d</i>	Diffusion term
N	Times of iteration
P	Pressure
UD	Up wind differential scheme
//, \perp	Parallel or vertical to the boundary



Chapter 1 Introduction

1.1 Preface

Stirred tanks are widely used in industrial mixing processes to carry out many different operations. Two or more kinds of materials would be mixed in chemical industrial or biological industrial. The main function of the agitation is to accelerate the heat and mass transfer process. We introduce energy into the vessel by the rotating impellers which convert this energy into hydrodynamic motion. A detailed understanding of the hydrodynamics of these vessels (velocity fields, turbulence, stress field, etc.) is essential to the optimum design of stirred tanks. The flow fields in agitated chemical reactors are very complex which have strong three dimensional characters with vertical structures that are not always well defined and high turbulence levels in the vicinity of the impellers. The flow complexity is greatly increased when a configuration of multiple impellers is adopted. It is hard to tell which distribution of impeller is better just by watching the flow field. So, we introduce power number, pumping number and many other numbers of efficiency to compare the efficiency of different stirred tanks.

The flow field in stirred vessels has been the subject of many experimental investigations in the past in order to investigate the scaling of quantities such as power consumption and mixing time with varying experimental conditions. Advanced experimental techniques and useful theoretical concepts of turbulence make it possible to analyze the fluid mechanics of these stirred vessels in a much more detailed manner. However, numerical modeling of the flow in such tanks is becoming more and more feasible because of the improvement of computers. The greatest advantage of the numerical simulation of stirred tanks is that the effects of tank

geometry and process parameters can be studied at low cost. These reasons are then making us to investigate the detailed understanding of the hydrodynamics of the stirred tanks by CFD simulation.

1.2 Definition of Radial flow and Axial flow

The flow field can be divided into two kinds when the flow is agitated by different kinds of impellers like the pitched blade impeller and propeller make the flow field become axial flow as the Rushton turbine and straight blade impeller agitate the flow to form radial flow (Fig.1.1). In present work, when the blade angle changes, the flow field will be changed from axial flow to radial flow. It is necessary to define the characteristic of the radial flow and the axial flow. There will be two circulations when the fluid flows out and back to the impeller swept region. We define the flow field as axial flow if the fluid flow downward out the impeller swept region and the division between the two circulations connect to vessel bottom. In the same way, if the fluid flow out the impeller swept region toward wall direction and the division between the two circulations connect to side wall, the flow field will be defined as radial flow (Fig.1.2).

1.3 Review of Previous Works

The following review is divided into two parts. The first part is experimental result, and the second part is numerical modeling. Each of them includes two parts, one is single impeller and the other one is dual impeller.

1.3.1 Experiments

1. Single impeller

Costes and Couderc [1] used two different cylindrical tanks, that geometrically

similar, with flat bottom and four vertical baffles to study turbulent flow induced by a Rushton turbine in a stirred tank by laser Doppler anemometer. Mean velocity and velocity fluctuations were measured at different impeller rotational speed. The discharge flow number and the circulation flow number were also calculated. They find that, in non-dimensional form, all the profiles are approximately independent of the system size and of the rotational speed of the impeller. The three components of velocity intensity are found to be the same order in the bulk region of the tank, and therefore, turbulence may be considered as isotropic and homogeneous in the bulk region. The pumping coefficient was measured as 0.73. The value of total circulation number is 3.4 in a plane 45° from the baffle.

Wu and Petterson [2] used one dimensional laser Doppler anemometer to profile mean and rms velocity of all the three component on vertical surface of impeller swept volume with periodicity that correspond to impeller blade frequency and twice that frequency removed. Radial profiles of pumping capacity in impeller stream have been presented. The pumping capacity increases with radius and maximum is around 2.5 times the discharge pumping capacity. Turbulent length scale has been reported for impeller stream. Energy balance around the impeller region and profiles of local energy dissipation rates have been reported. 30% of input energy dissipated in impeller region, about 30% dissipated in the impeller stream, and the rest, about 40% was dissipated in the bulk of the tank. The mean velocities, pumping capacities, and turbulence intensity in the impeller stream were approximately proportional to the impeller speed, in other words, the profiles on non-dimension are independent of rotational speed of impeller.

Ranade and Joshi [3] want to establish a complete understanding of the flow generated by a disc turbine in a fully baffled cylindrical vessel, as a reference case.

They measured the mean flow and turbulence intensities for bulk region using a laser Doppler anemometer. An energy balance around the impeller has been performed and the effect of vessel diameter on flow characteristics has also been studied. The comparison with published data of previous papers was also presented. The hydraulic efficiency of the disc turbine was found to be about 65% in the 500 mm i.d. vessel and 61% in the 300 mm i.d. vessel. And around 35%-40% of the input energy is dissipated in the impeller region. Various vertical plane located at different angles from the baffles has been measured. These profiles demonstrate the existence of vortices behind the baffle. The value of primary pumping number obtained in the present work is 0.74.

Yianneskis et al. [4] presented flow data for the trailing vortices and flow between two blades of impeller. Data presented in various r - z and r - θ planes near the impeller were used to characterize the trailing vortices behind the blades. The measurements quantify the mean flow and the kinetic energy of turbulence in the vortices and show that ensemble-average measurements of the flow over 360° of revolution can overestimate the turbulence fluctuations by up to 400%. The vortices structure is present in most cycles shown and each recording follows a similar pattern: the vortices appear to be generated constantly behind the blades, but have a short duration and are erratically broken-up occasionally. They also report the power number is 4.8 for the present geometry.

Mishra and Joshi [5] compared the flow generated by three different diameters of disc turbine with each other, with the flow generated by a standard disc turbine located on different clearances and with flow generated by other four designs of radial flow impellers, namely modified disc turbine, curved blade turbine, straight blade turbine and Brumagin impeller. The effect of impeller geometry on the turbulent flow was

measured using a laser Doppler anemometer. The comparison is presented in terms of mean velocities, turbulent kinetic energy, flow number, hydraulic efficiency and pumping effectiveness. The flow number of the disc turbine was found to be maximal at an impeller clearance of $H/3$, and for an impeller diameter of $T/3$. The hydraulic efficiency of the disc turbine is maximal for an impeller clearance of $H/2$, and for an impeller diameter of $T/3$. The straight blade turbine produces an unsteady flow with intermittent changes in direction of flow.

Mishra and Joshi [6] investigated three dimensional turbulent flow generated by multiple impellers using two kind of impellers that are a standard Rushton disc turbine(DT) and a pitched blade downflow turbine(PTD) and two impeller combinations: (1)DT-DT and (2)DT-PTD. Three dimensional mean and rms velocities generated by a double system have been reported over a wide range of impeller clearance and impeller location from the vessel bottom. The flow number and power number have also been measured for all the configurations. Energy balance had been established and the values of hydraulic efficiency and pumping effectiveness have been reported. The hydraulic efficiency and the pumping effectiveness for the DT-PTD impeller was found to be higher than the DT-DT impeller or a single disc turbine. They supposed that it is likely that PTD-PTD combination is superior even to the DT-PTD combination for a flow controlled operation.

Lee and Yianneslis [7] investigated the structure of the flow in a vessel stirred by a 100mm diameter Rushton turbine by laser Doppler anemometry. The flow field and turbulence structure produced in the vicinity of a Rushton impeller has been described in detail. The time and length scales of turbulence were determined and used to estimate the dissipation rate of turbulence energy. The level of turbulence energy and dissipation are high near the turbine and decrease rapidly with increasing distance

from the turbine blade. The degree of anisotropy of the turbulence in the vicinity of the impeller blades decreases with distance from the blade tip, as indicated by comparison of the three normal stress components.

Ranade et al. [8] studied the trailing vortices behind the blades of a standard Rushton turbine using PIV technique. Angle resolved and angle averaged flow fields near the impeller blades were measured and the structure of trailing vortices was studied in detail. They also do the computational simulation of flow field agitated by Rushton turbine with standard $k-\varepsilon$ and RNG $k-\varepsilon$ turbulent models. Predicted results were compared with the angle resolved PIV measurements. The trailing vortices were found to retain their coherent structure up to about 30° behind the leading blade. Predicted flow field show the presence of trailing vortices but under predicted the strength and the kinetic energy.

2. Dual impeller

Rutherford et al. [9] investigated the flows generated in vessels stirred by two Rushton turbines using flow visualization, power consumption, mixing time, and 360° ensemble-averaged and 1° angle-resolved LDA measurement techniques. They use two vessels of diameter $T=100\text{mm}$ and $T=294\text{mm}$ with impeller diameter $D=T/3$. The flow depended strongly on the clearance of the lower impeller above the base of the vessel(C1), the separation between the impellers(C2), and the submergence(C3) of the upper impeller below the top of the liquid height. When these distances were varied, three stable and four unstable flow patterns were observed. The three kind of stable flow patterns are the parallel flow, merging flow, and diverging flow with the clearance (C1,C2,C3) equal to $(0.25T, 0.5T, 0.25T)$, $(T/3, T/3, T/3)$, and $(0.15T, 0.5T, 0.35T)$ respectively as shown in Fig1.3. The total power number of the parallel flow pattern was 10, of the diverging flow pattern was 9.5, of the merging flow was 8.4 at

the impeller rotational speed equal to 250rpm.

Markopoulos et al. [10] presented that the dependence of power consumption on baffle length, L , in vessels agitated by a dual Rushton turbine system was studied within the turbulent regime, and also in relation to the impeller spacing ΔH (Fig. 1.4). The two Rushton turbines act independently at $\Delta H > 1.65d$. As the baffle length decrease, an increased mutual interaction between the two impellers can be observed for a large regime of $\Delta H/d$ values. Power number is not affected by ΔH for the unbaffled agitated systems studied.

1.3.2 Numerical modeling

1. Single Impeller

Ranade and Joshi [11] did the mathematical modeling and comparison with experimental data of reference [3]. The influences of grid size, impeller boundary conditions and values of model parameters on the predicted flow have been analyzed. The complete set of Reynolds equations coupled with the standard $k-\varepsilon$ model have been solved in the 3D domain of a stirred vessel. They used black box treatment for the impeller swept volume. That is solution of momentum equations for bulk region of the tank using impeller boundary conditions generated from the experiments. Then, solve momentum equations for the impeller region. Then couple the above two stages to avoid any need for empirical input to the flow problem. The model reproduce the three dimensional flow and other essential characteristics of the flow successfully.

Luo et al. [12] presents a CFD method which supply the treatment of the impeller region in the numerical solution such that the full flow field can be computed both within the impeller swept region and bulk region. The method developed with finite volume type and solves the time-dependent governing equation by sliding grids. After

about 6 complete impeller revolutions, the flow pattern become cyclically repeatable. They presented that the inherent unsteadiness of the flow, especially in the vicinity of the impeller is a significant phenomenon in stirred vessels and this has to be considered in the analysis if accurate predictions are to be obtained.

Luo et al. [13] presented an approach to predict the flow field induced by impellers in stirred tanks, including that within the impeller region, using steady-state computations. The method uses two frames of reference. The first rotates at the impeller speed and is used to compute the flow within the impeller in steady state manner. The second frame is stationary and is used to compute the flow away from the impeller. The comparisons were made against the measurement of Yianneskis and the simulation which employed empirically specified body forces in approximating. The radial and axial velocity profile showed good agreement with them. The advantage of this method over earlier steady prediction approach is that it is able to predict details of the flow field both within the impeller region and that outside it with attendant improvement in predictive accuracy.

Harvey III et al. [14] used an approximate steady-state method to compute the flow field agitated by pitched-blade impeller in a baffled stirred tank. The steady-state analysis involves accurately defining the geometry of the mixing tank using a multi-block grid technique. At higher Reynolds numbers the present steady-state numerical method will yield less accurate results. To accurately predict higher Reynolds number flows in stirred tanks, the turbulence model must be applied.

Tabor et al. [15] presented the results of numerical simulation of the fluid flow in a stirred tank with a 6-bladed Rushton turbine using two different techniques. One is a fully time-dependent approach and the other is an approximate steady-state approach. The fully time-dependent simulation is sliding mesh method, and the approximate

steady-state simulation is Multiple Reference Frame (MRF). They validated data of the two numerical methods against experimental data. They found the MRF model seems to have performed better in this case. There are several possible reasons for this, one is that a small impeller in a large tank is very suitable for the MRF case. Another possibility relates to numerical errors related to the complexity of the sliding mesh procedure.

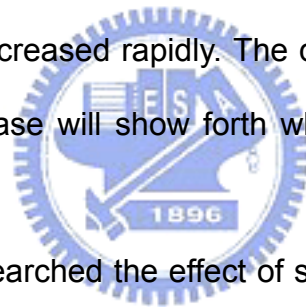
Jones et al. [16] predict the performance of six different two-equation turbulence models on the flow in an un-baffled stirred tank. The models include the low Reynolds number $k-\varepsilon$ model for Rodi et al., the high and low Reynolds number $k-\varepsilon$ model of Wilson, the RNG $k-\varepsilon$ model, modified $k-\omega$ and $k-\varepsilon$ models. Each model captures the qualitative circulation patterns in the stirred tank reactor. However, all of the models over-predict the mean radial discharge of the impeller due to an under-prediction of the eddy viscosity.

Hu [17] aimed on the modeling of flow field in stirred tank with pitched blade turbine and analyzing the flow field structures at horizontal and vertical plane, including the development of vortices. He investigated the change of flow field when the clearance from impeller to bottom decreases, and also investigated the influence of different blade angles. He presented that the change of clearance doesn't influence the flow field much, but the change of turbine blade angle do affect the flow field structure. The larger the blade angle is, the better the circulation capacity and power consumption is. But there is an utmost angle, when the blade angle is larger than that, the circulation capacity will go down.

Chou [18] also investigated the same impeller as Yu-Chang Hu, presented there is a critical angle of the pitched blade. When oblique angle of blade increases to the critical angle, the flow field changes from axial flow to radial flow, the power number

increases rapidly, and the pumping number decreases rapidly. The increase of power number that results from the change of fluid field will become bigger when the clearance from impeller to vessel bottom decrease. And it also leads to the increase of pumping number. He also changed the diameter of impeller. The bigger the impeller diameter is, the less the increase of power number is, and the bigger the decrease of pumping number is, when the oblique angle of blade reach critical angle.

Shen [19] analyzed the flow agitated by pitched blade disc turbine. She also found there is a critical angle of the pitched angle, and the flow field will change from axial flow to radial flow when the oblique angle of pitched blade reaches the critical angle. But there are some things different from Jian-Ren Chou's research. When the flow field changes from axial flow to radial flow, the power number decreases rapidly and the pumping number increased rapidly. The quantity of power number decrease and pumping number increase will show forth when the clearance from impeller to vessel bottom decreased.



Jaworski et al. [20] researched the effect of size, location and pumping direction of pitched blade turbine impellers on flow patterns by LDA measurement and CFD predictions. The CFD method used in this work is MRF method. The CFD and LDA study has been undertaken of the turbulent flow associated with two sizes of six-bladed 45° pitched blade turbine at three clearances. They showed that most of the differences between the CFD and LDA results were within the 5% range of tip velocity

2. Dual Impeller

Harvey et al. [21] computed the flow with an incompressible Navier-stokes solver which use the pseudocompressibility technique of coupling the velocity and pressure field. The laminar viscous flow field is solved using an approximate steady-state

technique which neglects relative motion between the impellers and baffles. This work illustrates that the circulation patterns within the tank strongly depend on relative impeller size and spacing. This work also shows the utility of the numerical method for studying complex multiple impeller flows at low Reynolds number.

Micale et al. [22] presented prediction of flow fields in a dual-impeller stirred vessel. Three modeling approaches were tested. First is time-dependence sliding grid technique. Second approach is steady-state IO technique: the vessel was modeled as two partially overlapping regions, the inner one rotating with the impeller and the outer one stationary; simulations were run in steady-state mode for each of the two regions while information was iteratively exchanged between them after azimuthally averaging and transforming for the relative motion. Third is the similar impeller boundary condition approach. Three impeller modeling techniques were compared with the experimental data of reference [9]. The first two techniques gave similar predictions and successfully reproduced the dependence of the flow patterns on the position of the impellers. The last technique gave satisfactory results only in the simple case of parallel flow, but failed to predict the merging flow and diverging flow.

1.4 Study Objective

This study is to model the flow field of a mixing tank stirred by single or multiple impellers using quasi steady-state Multiple Reference Frame (MRF). We discretize the governing equation by finite volume method. Turbulence was modeled by using the standard $k-\varepsilon$ model with “wall function” on walls. The SIMPLE algorithm was used to couple the continuity and Navier-Stokes equations. We change the clearance between impellers and vessel bottom to investigate the performance of mixing and parameters of the flow field.

The flow field agitated by single disc turbine was modeled again. The geometry

is just the same as Shih-Jhen Shen's [19] model, but the location of stationary frame and rotational frame is different (Fig.1.5, Fig.1.6). In shen's model, the rotational frame is defined only at the range of impeller blade in radius direction and in axial direction; stationary frame is used on the other places. The rotational frame in present work is defined encompass all the impeller and the flow surrounding it. Quasi-steady state flow conditions are assumed at the interface between the two reference frames. That is, the velocity at the interface must be the same for each reference frame. The predictions of velocity field, power number, and pumping number are much more close to the experimental data at this setting. And this setting is also applied to stirred tank with dual impellers.




Chapter2 Mathematical Model

2.1 Basic assumptions

In this work, the equations to be solved were the continuity and momentum (Navier-Stokes) equations for a constant-density fluid in turbulent motion. The working fluid used here is water. We have some assumptions for the flow field

1. The flow field is in quasi-steady state.
2. The flow field is isothermal: The temperature in the process does not vary obviously. We can assume that the flow field is isothermal.
3. The flow field is fully three dimensional and the effect of gravity is neglected.

2.2 The governing equations of the MRF(Multiple Reference Frame) model



The MRF model utilizes the fact that for those geometrics where the clearance between the impeller and the baffles is comparable with or greater than the impeller diameter, the flow pattern in the vicinity of the impeller is unaffected by the rest of the tank, and thus be calculated as a time-independent problem in the frame of reference co-rotating with the impeller. As some distance away from the impeller it is assumed that the flow is cylindrically symmetric, and so beyond this distance the flow is time-independent in the frame of reference of the tank. The technique is clearly appropriate for tank geometries with sufficient spacing between the impeller blades and the baffles like the present case.

2.2.1 The govern equations in the stationary frame

A stationary frame is used for the flow outside the impeller region. The govern equations in Eulerian coordinates can be written as so:

Continuity equation

$$\frac{\partial(\rho U_j)}{\partial x_j} = 0 \quad (2.1)$$

Momentum equation

$$\frac{\partial(\rho U_i U_j)}{\partial x_j} = -\frac{\partial p}{\partial x_i} + \frac{\partial}{\partial x_j} \left[\mu \left(\frac{\partial U_i}{\partial x_j} + \frac{\partial U_j}{\partial x_i} \right) \right] \quad (2.2)$$

2.2.2 Time-average eddy viscosity turbulent model: the k-ε model

Turbulence was modeled by using the standard $k-\varepsilon$ model with wall function at the near-wall region. The complete set of Reynolds equations coupled with the standard $k-\varepsilon$ model have been solved in the three dimensional domain of the stirred vessel. In the Reynolds averaging process U_i is divided into a steady mean value \tilde{U}_i and a fluctuating component U'_i :

$$U_i = \tilde{U}_i + U'_i$$

(2.3)

substitute (2.3) into (2.1) and (2.2), then

Continuity equation:

$$\frac{\partial(\rho \tilde{U}_j)}{\partial x_j} = 0 \quad (2.4)$$

Momentum equation:

$$\frac{\partial(\rho \tilde{U}_i \tilde{U}_j)}{\partial x_j} = -\frac{\partial p}{\partial x_i} + \frac{\partial}{\partial x_j} \left[\mu \left(\frac{\partial \tilde{U}_i}{\partial x_j} + \frac{\partial \tilde{U}_j}{\partial x_i} \right) - \rho \left(\tilde{U}'_i \tilde{U}'_j \right) \right] \quad (2.5)$$

$-\rho \left(\tilde{U}'_i \tilde{U}'_j \right)$ is the Reynold stresses needed to be modeled.

Following the assumption of Boussinesq(1877), the Reynold stresses an linearly related with average strain rates:

$$\tau_{ij} = -\rho \left(\widetilde{U'_i U'_j} \right) = 2\mu_t D_{ij} - \frac{2}{3} \rho k \delta_{ij} \quad (2.6)$$

With the average strain rates:

$$D_{ij} = \frac{1}{2} \left(\frac{\partial \widetilde{U}_i}{\partial x_j} + \frac{\partial \widetilde{U}_j}{\partial x_i} \right) \quad (2.7)$$

turbulence viscosity:

$$\mu_t = \frac{C_\mu \rho k^2}{\varepsilon} \quad (2.8)$$

turbulent kinetic energy:

$$k = \frac{\widetilde{U'_i U'_i}}{2} \quad (2.9)$$

viscous dissipation rate:

$$\varepsilon = \nu \left(\frac{\partial U'_i}{\partial x_j} \right)^2 \quad (2.10)$$

and:

$$C_\mu = 0.09$$

substitute(2.6)into(2.5), the momentum equation become:

$$\frac{\partial(\rho \widetilde{U}_i \widetilde{U}_j)}{\partial x_j} = -\frac{\partial p}{\partial x_i} + \frac{\partial}{\partial x_j} \left[\mu_{eff} \left(\frac{\partial \widetilde{U}_i}{\partial x_j} + \frac{\partial \widetilde{U}_j}{\partial x_i} \right) - \frac{2}{3} \rho k \delta_{ij} \right] \quad (2.11)$$

where

$$\mu_{eff} = \mu + \mu_t$$

The equations of k and ε can be derived from Navier-Stokes equation:

K equation:

$$\frac{\partial(\rho \tilde{U}_j k)}{\partial x_j} = \frac{\partial}{\partial x_j} \left(\frac{\mu_{eff}}{\sigma_k} \frac{\partial k}{\partial x_j} \right) + P - \rho \varepsilon$$

(2.12)

ε equation:

$$\frac{\partial(\rho \tilde{U}_j \varepsilon)}{\partial x_j} = \frac{\partial}{\partial x_j} \left(\frac{\mu_{eff}}{\sigma_\varepsilon} \frac{\partial \varepsilon}{\partial x_j} \right) + C_{\varepsilon 1} \frac{\varepsilon}{k} P - C_{\varepsilon 2} \rho \frac{\varepsilon^2}{k} \quad (2.13)$$

P is a production term:

$$P = -\rho (\tilde{U}_i' U_j') \frac{\partial \tilde{U}_i}{\partial x_j} = \mu_t \left[\frac{\partial \tilde{U}_i}{\partial x_j} + \frac{\partial \tilde{U}_j}{\partial x_i} \right] \frac{\partial \tilde{U}_i}{\partial x_j} \quad (2.14)$$

According to Launder and Spalding [23] we got:

$$C_{\varepsilon 1} = 1.44 ; C_{\varepsilon 2} = 1.92 ; \sigma_k = 1.00 ; \sigma_\varepsilon = 1.30$$

2.2.3 The governing equation in the rotational frame

It is assumed that the flow field is quasi-steady state, ignoring variation of time.

We define the grid velocity as $\bar{U}_g = \bar{\Omega} \times \bar{r}$ in the blade swept region. In the momentum equation the rotation-induced body force, including centrifugal force and Coriolis force, must be accounted for as sources.

Centrifugal force:

$$-\rho \varepsilon_{mni} \Omega_m (\varepsilon_{pqn} \Omega_p x_q)$$

Coriolis force:

$$2\rho \varepsilon_{mni} \Omega_m (\tilde{U}_n - U_{gn})$$

$\bar{\Omega}$ is the angular speed of the impeller and \bar{r} is the position vector of the considered nodal point. Governing equations are given below:

Continuity equation:

$$\frac{\partial[\rho(\tilde{U}_j - U_{gj})]}{\partial x_j} = 0$$

(2.22)

Momentum equation:

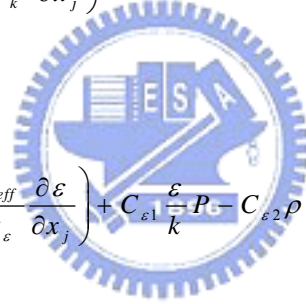
$$\begin{aligned} \frac{\partial[\rho(\tilde{U}_i - U_{gi})(\tilde{U}_j - U_{gj})]}{\partial x_j} = & -\frac{\partial p}{\partial x_i} + \frac{\partial}{\partial x_j} \left[\mu_{eff} \left(\frac{\partial(\tilde{U}_i - U_{gi})}{\partial x_j} + \frac{\partial(\tilde{U}_j - U_{gj})}{\partial x_i} \right) - \frac{2}{3} \rho k \delta_{ij} \right] \\ & - \rho \varepsilon_{mni} \Omega_m (\varepsilon_{pqn} \Omega_p x_q) + 2 \rho \varepsilon_{mni} \Omega_m (\tilde{U}_n - U_{gn}) \end{aligned} \quad (2.23)$$

k equation:

$$\frac{\partial[\rho(\tilde{U}_j - U_{gj})k]}{\partial x_j} = \frac{\partial}{\partial x_j} \left(\frac{\mu_{eff}}{\sigma_k} \frac{\partial k}{\partial x_j} \right) + P - \rho \varepsilon \quad (2.24)$$

ε equation:

$$\frac{\partial[\rho(\tilde{U}_j - U_{gj})\varepsilon]}{\partial x_j} = \frac{\partial}{\partial x_j} \left(\frac{\mu_{eff}}{\sigma_\varepsilon} \frac{\partial \varepsilon}{\partial x_j} \right) + C_{\varepsilon 1} \frac{\varepsilon}{k} P - C_{\varepsilon 2} \rho \frac{\varepsilon^2}{k} \quad (2.25)$$



2.3 Boundary conditions

The area that we want to calculate is the whole vessel. Therefore, that must take a lot of time when the computational cells are too fine. In order to decrease the computational effort required, we have to set a periodic boundary condition.

2.3.1 Periodic boundary conditions

The baffles and the impeller are arranged in a symmetrical manner. Due to the symmetrical arrangement the flow becomes periodic. Therefore, only half of the tank is considered in calculations. Periodic boundary conditions are imposed on the symmetrical planes. The flux out of the 0° radial plane must be carried into 180° plane as shown in Fig. 2.1.

2.3.2 Boundary conditions on the solid walls

Because of the boundary condition is no slip boundary condition; the velocity of fluid next to the walls is the velocity of the walls. There are rotational impellers and vessel walls, they are moving walls and stationary walls. Due to the use of high Reynolds number $k-\varepsilon$ model, we use wall function near the walls. It will be introduced in the next chapter.

1. Stationary walls: For lid of the vessel, bottom of the vessel, side wall of the vessel, baffles, $\vec{U} = 0$.
2. Moving walls: For the shaft and the impellers $\vec{U} = \vec{\Omega} \times \vec{r}$, \vec{r} is the position vector of the impellers.



Chapter 3 Numerical Methods

3.1 Discretization of Governing Equations

Because the unstructured grid can be applied to the complex geometry better than the structured grid can, this research used the unstructured grid. Grids are arranged as un-staggered grid. We put the variables and properties of the flow field in the center of the control volume. Using finite volume method to discretise the governing equations. We introduce a general variable ϕ , the conservation form of all the fluid flow equations presented in chapter 2 can be written as:

$$\nabla \cdot [\rho(\vec{U} - \vec{U}_g)\phi] = \nabla \cdot (\Gamma \nabla \phi) + q_\phi \quad (3.1)$$

\vec{U}_g is the speed of the grid.

In the following, we discuss the convection term, diffusion term and source term separately:



3.1.1 Convection Term

According to the Gauss's divergence theorem, we transform volume integral into face integral. Then use midpoint rule to transform surface integral into difference form.

$$\oint \nabla \cdot (\rho \vec{v} \phi) dV = \iint_S (\rho \vec{v} \phi) \cdot d\vec{S} \quad (3.2)$$

$$\iint_S [\rho(\vec{U} - \vec{U}_g)\phi] \cdot d\vec{S} \approx \sum_f [\rho(\vec{U} - \vec{U}_g)\phi]_f \cdot S_f = \sum_f \dot{m}_f \phi_f = \sum_f F_f^c \quad (3.3)$$

The suffix 'f' means the center point of the face of each volume. \dot{m} is the mass flow rate, F_f^c is the convectational flux.

For the convection term we use a scheme mixing first order upwind differencing scheme and second order upwind difference on convection term. Because in a

strongly convective flow, the upstream cell face should receive much stronger influence from upwind node than from node P.

$$F_f^C = \dot{m}_f \Phi_f = \dot{m}_f (\Phi_f^{UD} + \gamma \nabla \Phi_f^{UD} \cdot \delta \vec{r})$$

(3.4)

Φ_f^{UD} is the value on the face solving by first order upwind differencing scheme. γ is a value between 0 and 1. It approaches 1 in order to reach second order accuracy.

(3.4) becomes :

$$\begin{aligned} \dot{m}_f \Phi_f = & \max(\dot{m}_f, 0) \Phi_P - \max(-\dot{m}_f, 0) \Phi_C \\ & + \gamma \left[\max(\dot{m}_f, 0) \nabla \Phi_P \cdot \delta \vec{r} - \max(-\dot{m}_f, 0) \nabla \Phi_C \cdot \delta \vec{r} \right] \end{aligned} \quad (3.5)$$

The first two terms represent the first order upwind differencing scheme, which are treated implicitly. The third term is considered as source term.

3.1.2 Diffusion Term

According to the Gauss's divergence theorem, we transform volume integral into face integral, then use the midpoint rule to transform surface integral into difference form. The diffusion flux F_f^D for variable ϕ can be written as follows:

$$F_f^D = \Gamma_f (\nabla \phi)_f \cdot \vec{S}_f \quad (3.6)$$

let

$$\vec{S}_f = \vec{d} + (\vec{S}_f - \vec{d}) \quad (3.7)$$

where (Fig. 3.1)

$$\vec{d} \equiv \frac{|\vec{S}_f|}{\vec{e}_d \cdot \vec{e}_s} \vec{e}_d = \frac{|\vec{S}_f|^2}{\delta \vec{r} \cdot \vec{S}_f} \delta \vec{r} \quad (3.8)$$

Substitute (3.7) 、 (3.8) into (3.6) :

$$F_f^D = \frac{\Gamma_f |\bar{S}_f|^2}{\delta \bar{r} \cdot \bar{S}_f} (\phi_C - \phi_P) + \underline{\Gamma_f \nabla \phi_f (\bar{S}_f - \bar{d})} \quad (3.9)$$

The term with underline is considered as source term during solution iteration..

3.1.3 Source term

Take volume integral over the source term q_ϕ :

$$Q_\phi = \int_{\Delta V} q_\phi dV \approx (q_\phi \Delta V)_P \quad (3.10)$$

Each source terms is discussed individually :

For the pressure gradient term, we apply Gauss's divergence theorem and midpoint rule:

$$\nabla P = \frac{1}{\Delta V} \iiint_{\Delta V} \nabla P dV = \frac{1}{\Delta V} \iint_s P d\bar{S} \approx \frac{1}{\Delta V} \sum_f P_f \bar{S}_f \quad (3.11)$$

In the i direction :

$$\frac{\partial p}{\partial x_i} = \frac{1}{\Delta V} \int_{\Delta V} \frac{\partial p}{\partial x_i} dV = \frac{1}{\Delta V} \int_{\Delta V} (\nabla p \cdot \bar{e}_i) dV \approx \frac{1}{\Delta V} \sum_f p_f \bar{S}_{fi} \quad (3.12)$$

Calculate boundary pressure p_a as follows:

$$p_a - p_p = \nabla p_p \cdot \delta \bar{r} \quad (3.13)$$

Where $\delta \bar{r}$ is the vector from nodal point P to boundary a (fig3.2). Pressure gradient ∇p_p was processed to separate the pressure on the boundary and pressure on the other surface.

$$\nabla p_p = \frac{1}{\Delta V} \int_{\Delta V} \nabla p dV = \frac{1}{\Delta V} \int_s p \bar{S} = \frac{1}{\Delta V} \sum_f p_f \bar{S}_f = \frac{1}{\Delta V} \left(p_a \bar{S}_a + \sum_{f \neq a} p_f \bar{S}_f \right) \quad (3.14)$$

Substitute (3.14) into (3.13), then we got the pressure on the boundary:

$$p_a = \frac{p_p + \frac{1}{\Delta V} \sum_{f \neq a} p_f \bar{S}_f \cdot \delta \bar{r}}{1 - \frac{1}{\Delta V} \bar{S}_a \cdot \delta \bar{r}} \quad (3.15)$$

The velocity gradient $\frac{\partial U_i}{\partial x_j}$ was processed as follows:

$$\frac{\partial U_i}{\partial x_j} = \frac{1}{\Delta V} \int_{\Delta V} \frac{\partial U_i}{\partial x_j} dV = \frac{1}{\Delta V} \int_S U_i \bar{e}_j \cdot d\bar{S} = \frac{1}{\Delta V} \sum_f U_{fi} S_{fj} \quad (3.16)$$

Centrifugal force and Coriolis force must be accounted for as sources.

Centrifugal force:

$$\int_{\Delta V} -\rho \varepsilon_{mni} \Omega_m (\varepsilon_{pqn} \Omega_p x_q) dV = [-\rho \varepsilon_{mni} \Omega_m (\varepsilon_{pqn} \Omega_p x_q) \Delta V]_p \quad (3.17)$$

Coriolis force:

$$\int_{\Delta V} 2\rho \varepsilon_{mni} \Omega_m (\tilde{U}_n - U_{gn}) dV = [2\rho \varepsilon_{mni} \Omega_m (\tilde{U}_n - U_{gn}) \Delta V]_p \quad (3.18)$$

When mni is increasing (for example: 123), ε_{mni} is 1. When mni is decreasing (for example: 321), ε_{mni} is -1. ε_{mni} is 0 in other situation.

3.1.4 Difference equation

Combine the convection term, diffusion term and source term given above:

$$a_p \phi_p = \sum_c a_c \phi_c + Q_\phi \quad (3.19)$$

$$a_p = \sum_c a_c, \quad a_c = \frac{\Gamma_f |\vec{S}_f|^2}{\vec{\delta} \cdot \vec{S}_f} + \max(-\dot{m}_f, 0) \quad (3.20)$$

$$Q_\phi = \sum_f -\gamma \left[\max(\dot{m}_f, 0) \nabla \Phi_p \cdot \delta \bar{r} - \max(-\dot{m}_f, 0) \nabla \Phi_c \cdot \delta \bar{r} \right] + \sum_f \Gamma_f \nabla \Phi_f (\vec{S}_f - \vec{d}) + (q_\phi \Delta V)_p \quad (3.21)$$

In order to stabilize the iteration process, we introduce an under-relaxation factor α_ϕ .

the momentum equation becomes:

$$\frac{a_p}{\alpha_\phi} \Phi_p^{(n+1)} = \sum_C a_C \Phi_C^{(n+1)} + Q_\phi + (1 - \alpha_\phi) \frac{a_p}{\alpha_\phi} \Phi_p^{(n)} \quad (3.22)$$

the superscript $(n+1)$ is the new value and subscript (n) is the value of previous iteration. Substitute $\frac{a_p}{\alpha_\phi} = a'_p$ into (3.22):

$$a'_p \Phi_p^{(n+1)} = \sum_C a_C \Phi_C^{(n+1)} + Q_\phi + (1 - \alpha_\phi) a'_p \Phi_p^{(n)} \quad (3.23)$$

α_ϕ for momentum equation is set as 0.5~0.75, α_ϕ for κ and ϵ equation are set as 0.1.

3.2 Calculation of the Rate of Flux through control surface:

In order to satisfy continuity equation, we have to calculate velocity on the surface. First, we have to find the relation between velocity and pressure. Second, Find the relation between velocity and pressure on the face by linear interpolation to calculate the flow flux rate. In (3.19), separate the pressure term from source term then we can get the relation between velocity and pressure on primary grid:

$$\bar{U}_p = \bar{H}_p - \left(\frac{\Delta V}{a_p} \right)_p \nabla p_p \quad (3.24)$$

Relation between velocity and pressure on the control volume surface:

$$\bar{U}_f = \bar{\bar{H}}_f - \left(\frac{\Delta V}{a_p} \right)_f \nabla p_f \quad (3.25)$$

$$\bar{\bar{H}}_f = \bar{\bar{U}}_f + \left(\frac{\Delta V}{a_p} \right)_f \bar{\nabla} p_f \quad (3.26)$$

Substitute(3.26) into (3.25):

$$\bar{U}_f = \bar{\bar{U}}_f - \left(\frac{\Delta V}{a_p} \right)_f (\nabla p_f - \bar{\nabla} p_f) \quad (3.27)$$

The value with overbar “—” is interpolated between main point P and neighbor point C.

w_p is weighting factor.

$$\overline{\overline{U}}_f = w_p \overline{U}_c + (1 - w_p) \overline{U}_p \quad (3.28)$$

$$\left(\frac{\overline{\Delta V}}{a_p} \right)_f = w_p \left(\frac{\Delta V}{a_p} \right)_c + (1 - w_p) \left(\frac{\Delta V}{a_p} \right)_p \quad (3.29)$$

$$\overline{\nabla p}_f = w_p \nabla p_c + (1 - w_p) \nabla p_p \quad (3.30)$$

The flow flux rate can be written as:

$$\begin{aligned} \dot{m}_f &= \rho_f (\overline{U}_f - \overline{U}_{gf}) \cdot \overline{S}_f = \rho_f (\overline{\overline{U}}_f - \overline{U}_{gf}) \cdot \overline{S}_f - \rho_f \left(\frac{\overline{\Delta V}}{a_p} \right)_f (\nabla p_f - \overline{\nabla p}_f) \cdot \overline{S}_f \\ &\approx \rho_f (\overline{\overline{U}}_f - \overline{U}_{gf}) \cdot \overline{S}_f - \rho_f \left(\frac{\overline{\Delta V}}{a_p} \right)_f (\nabla p_f - \overline{\nabla p}_f) \cdot \overline{d} \\ &= \rho_f (\overline{\overline{U}}_f - \overline{U}_{gf}) \cdot \overline{S}_f - \rho_f \left(\frac{\overline{\Delta V}}{a_p} \right)_f \frac{|\overline{S}_f|^2}{\overline{\delta r} \cdot \overline{S}_f} \left[(p_c - p_p) - \overline{\nabla p}_f \cdot \overline{\delta r} \right] \end{aligned} \quad (3.31)$$

\overline{U}_{gf} is the velocity of the grid face of rotational reference frame. The definition of \overline{d} is given in (3.8).

3.3 Pressure Correction Equation

Following the SIMPLE algorithm presented by Patankar, we substitute the pressure P^* , that calculated from previous iteration, into (3.22). Then we can solve the velocity \overline{V}^* in the center of the grid (P). But the velocity \overline{V}^* and pressure P^* does not satisfy continuity equation. We have to correct it. Let the corrected pressure and velocity be \overline{V}^{**} and P^{**} , respectively.

Define pressure correction as: $P_p' = P_p^{**} - P_p^*$

Define velocity correction as: $\overline{U}_p' = \overline{U}_p^{**} - \overline{U}_p^*$

The relation between pressure correction and velocity correction can be written as

follows:

$$\bar{U}'_p = - \left(\frac{\Delta V}{a_p} \right)_p \nabla p'_p \quad (3.32)$$

We also can get the velocity correction on face :

$$\bar{U}'_f = \bar{U}_f^{**} - \bar{U}_f^* = - \left(\frac{\Delta V}{a_p} \right)_f \nabla p'_f \quad (3.33)$$

Then we obtain corrected mass flux:

$$\begin{aligned} \dot{m}_f^{**} &= \dot{m}_f^* + \rho_f \bar{U}'_f \cdot \bar{S}_f = \dot{m}_f^* - \rho_f \left(\frac{\Delta V}{a_p} \right)_f \nabla p'_f \cdot \bar{S}_f \\ &= \dot{m}_f^* - \rho_f \left(\frac{\Delta V}{a_p} \right)_f \nabla p'_f \cdot \bar{d} - \rho_f \left(\frac{\Delta V}{a_p} \right)_f \nabla p'_f \cdot (\bar{S}_f - \bar{d}) \\ &= \dot{m}_f^* - \rho_f \left(\frac{\Delta V}{a_p} \right)_f \frac{|\bar{S}_f|^2}{\delta \vec{r} \cdot \bar{S}_f} (p'_c - p'_p) - \rho_f \left(\frac{\Delta V}{a_p} \right)_f \nabla p'_f \cdot (\bar{S}_f - \bar{d}) \end{aligned} \quad (3.34)$$

Continuity is satisfied in discretised form for a control volume:

$$\sum_f \dot{m}_f^{**} = 0 \quad (3.35)$$

Substitute (3.34) into (3.35), we obtain an equation for pressure correction:

$$A_p^p P_p' = \sum_c A_c^p P_c' + S_{p1} + S_{p2} \quad (3.36)$$

where $A_c^p = \rho_f \left(\frac{\Delta V}{A_p} \right)_f \frac{|\bar{S}_f|^2}{\delta \vec{r} \cdot \bar{S}_f}$

$$A_p^p = \sum_c A_c^p$$

$$S_{p1} = \sum_f \dot{m}_f^*$$

$$S_{p2} = \sum_f \rho_f \left(\frac{\Delta V}{A_p} \right)_f \nabla p'_f \cdot (\bar{S}_f - \bar{d})$$

After we get P' , we also can get P_p^{**} , \bar{U}_p' , \bar{V}^{**} , and \dot{m}_f^* .

Because S_{p2} term includes P' . Consider the effect of P' , we use two correction steps to solve this equation for pressure correction approximately:

We only consider S_{p1} in the first step, then we get pressure correction $p'^{(1)}$

$$A_p p_p'^{(1)} = \sum_C A_c p_c'^{(1)} + S_{p1} \quad (3.37)$$

Then we substitute $p'^{(1)}$ into S_{p2} to calculate $p'^{(2)}$:

$$A_p p_p'^{(2)} = \sum_C A_c p_c'^{(2)} + S_{p2}^{(1)} \quad (3.38)$$

$$S_{p2}^{(1)} = \sum_f \rho_f \left(\frac{\Delta V}{A_p} \nabla p_f'^{(1)} \right)_f \cdot (\bar{S}_f - \bar{d})$$

After solving for $p_p'^{(1)}$ and $p_p'^{(2)}$ we can get p_p^{**} :

$$p_p^{**} = p_p^* + p_p'^{(1)} + p_p'^{(2)} \quad (3.41)$$

and \bar{U}^{**} :

$$\bar{U}_p^{**} = \bar{U}_p^* - \left(\frac{\Delta V}{a_p} \right)_p (\nabla p_p'^{(1)} + \nabla p_p'^{(2)}) \quad (3.42)$$

Corrected mass flux was obtained as follows:

First step correction:

$$\dot{m}_f^{**} = \dot{m}_f^* - \rho_f \left(\frac{\Delta V}{a_p} \right)_f \frac{|\bar{S}_f|^2}{\delta \bar{r} \cdot \bar{S}_f} (p_c'^{(1)} - p_p'^{(1)}) \quad (3.43)$$

Second step correction:

$$\dot{m}_f^{**} = \dot{m}_f^* - \rho_f \left(\frac{\Delta V}{a_p} \right)_f \nabla p_f'^{(2)} \cdot (\bar{S}_f - \bar{d}) \quad (3.44)$$

3.4 Boundary Conditions

3.4.1 Periodic boundary condition

Because of the rotation of impeller blades, cylindrical coordinates is used on the periodic boundary condition. The corresponding values of periodic boundary are presented on cylindrical coordinates. But we analyze the flow field on Cartesian coordinates. For vector quantities we have to correct the value of periodic boundary condition by coordinates transport. For pure quantities we do not have to process it by special way, just give it the corresponding values.

Process methods of scalar quantities and vector quantities were written below:

Scalar quantities: For pressure, κ , ε . Because of the direction-less of them, it is not necessary for them to coordinate transport. We just have to load the values of corresponding grids. (Fig 2.1) ◦

$$\phi_1 = \phi_1, \quad \phi_2 = \phi_2. \quad (3.45)$$

Vector quantities: For velocity vectors and gradient of each property, such as pressure gradient, velocity gradient, gradient of κ , and gradient of ε . The periodic boundary condition should be corrected by cylindrical coordinates, but the Cartesian coordinates was used to analyze the flow field. We have to transfer the value of vector from Cartesian coordinates to cylindrical coordinates. Then we can match the values of periodic boundary condition. Take grid 1' that next to grid 2 as the example.

(1) Transfer the vector value of grid 1 from Cartesian coordinates to cylindrical coordinates:

$$\phi_{r1} = \bar{\phi}_1 \cdot \bar{e}_{r1} = (\phi_{x1} \bar{i} + \phi_{y1} \bar{j} + \phi_{z1} \bar{k}) \cdot (\cos \theta_1 \bar{j} + \sin \theta_1 \bar{k}) = \phi_{y1} \cos \theta_1 + \phi_{z1} \sin \theta_1 \quad (3.46)$$

$$\phi_{\theta_1} = \bar{\phi}_1 \cdot \bar{e}_{\theta_1} = (\phi_{x1}\bar{i} + \phi_{y1}\bar{j} + \phi_{z1}\bar{k}) \cdot (\cos\theta_1\bar{k} - \sin\theta_1\bar{j}) = \phi_{z1}\cos\theta_1 - \phi_{y1}\sin\theta_1 \quad (3.47)$$

(2) Load the values of corresponding grids : $\phi_{r1'} = \phi_{r1}$, $\phi_{\theta1'} = \phi_{\theta1}$

(3.48)

(3) Finally, we transfer the value of vector from cylindrical coordinates to Cartesian coordinates:

$$\phi_{y1'} = \phi_{r1}\cos\theta_1' - \phi_{\theta1}\sin\theta_1' \quad (3.49)$$

$$\phi_{z1'} = \phi_{r1}\sin\theta_1' + \phi_{\theta1}\cos\theta_1' \quad (3.50)$$

Define: \bar{e} is a unit vector; ϕ is a vector, ϕ is the component of this vector.

3.4.2 Solid wall boundary condition

(a) wall-function

The turbulent model used in this research is high Reynold number k-ε model. It is unsuitable near walls, because the change of properties is quite fast near walls. In order to solve this kind of situation, we introduced wall-function to process the wall shear stress and k-ε model of grids that next to walls.

Assume the flow field that out of viscous sublayer follow logarithmic law. The wall shear stress can be written as:

$$\bar{\tau}_w = \frac{\mu_{eff}}{\delta n} \left[\bar{S}_w \right] \delta \bar{U}''$$

where:

$$\mu_{eff} = \begin{cases} \mu & \text{for } y^+ < 11.63 \\ \frac{\mu y^+}{u^+} & \text{for } y^+ \geq 11.63 \end{cases} \quad (3.51)$$

$$y^+ = \frac{\rho c_{\mu}^{1/4} k^{1/2} \delta n}{\mu} \quad (3.52)$$

$$u^+ = \frac{1}{\kappa} \ln(Ey^+) \quad (3.53)$$

Define Von-Karmon's constant $\kappa=0.4187$, $E =9.793$.

The k - ε equation of grids that next to walls also need processed specially. Assume the generation and consumption of turbulent energy reach balance near walls, define ε as:

$$\varepsilon = \frac{c_{\mu}^{\frac{3}{4}} k^{\frac{3}{2}}}{\kappa \delta n} \quad (3.54)$$

Equation (3.45) will replace ε equation in grids next to walls. The generation term P and consumption term $\rho\varepsilon$ have to change, too. ε in consumption term was taken the average value on volume:

$$\bar{\varepsilon} = \frac{c_{\mu} \rho k^2}{\mu_{eff}} \quad (3.55)$$

The production term can written as follows:

$$P \approx \tau_w \frac{\delta U''}{\delta n} \quad (3.56)$$

(b) Shear stress

On grids that next to walls, we calculate wall shear stress (Fig 3.3). P is the primary grid center, w is the wall, and \bar{S}_w is the normal vector of the wall. The velocity of P is \bar{U}_P , the velocity of the wall is \bar{U}_w . The normal vector of the wall that forward grid \bar{n} is written below:

$$\bar{n} = - \frac{S_{wx} \bar{i} + S_{wy} \bar{j} + S_{wz} \bar{k}}{|\bar{S}_w|} \quad (3.57)$$

The relative velocity between the main grid (P) and wall (w) is:

$$\delta \bar{U} = \bar{U}_P - \bar{U}_w \quad (3.58)$$

The velocity quantity that normal to the wall is $\delta\bar{U}^\perp$

$$\begin{aligned}
 \delta\bar{U}^\perp &= (\delta\bar{U} \cdot \bar{n})\bar{n} = \frac{\delta u S_{wx} + \delta v S_{wy} + \delta w S_{wz}}{|\bar{S}_w|} \frac{S_{wx}\bar{i} + S_{wy}\bar{j} + S_{wz}\bar{k}}{|\bar{S}_w|} \\
 &= \frac{1}{|\bar{S}_w|^2} \left[\delta u S_{wx}^2 + \delta v S_{wx} S_{wy} + \delta w S_{wx} S_{wz} \right] \bar{i} \\
 &\quad + \frac{1}{|\bar{S}_w|^2} \left[\delta u S_{wx} S_{wy} + \delta v S_{wy}^2 + \delta w S_{wy} S_{wz} \right] \bar{j} \\
 &\quad + \frac{1}{|\bar{S}_w|^2} \left[\delta u S_{wx} S_{wz} + \delta v S_{wy} S_{wz} + \delta w S_{wz}^2 \right] \bar{k} \tag{3.59}
 \end{aligned}$$

And the velocity quantity that parallel to the wall is $\delta\bar{U}^\parallel$:

$$\begin{aligned}
 \delta\bar{U}^\parallel &= \delta\bar{U} - \delta\bar{U}^\perp \\
 &= \frac{1}{|\bar{S}_w|^2} \left[\delta u (S_{wy}^2 + S_{wz}^2) - \delta v S_{wx} S_{wy} + \delta w S_{wx} S_{wz} \right] \bar{i} \\
 &\quad + \frac{1}{|\bar{S}_w|^2} \left[-\delta u S_{wx} S_{wy} + \delta v (S_{wx}^2 + S_{wz}^2) - \delta w S_{wy} S_{wz} \right] \bar{j} \\
 &\quad + \frac{1}{|\bar{S}_w|^2} \left[-\delta u S_{wx} S_{wz} + \delta v S_{wy} S_{wz} - \delta w (S_{wx}^2 + S_{wy}^2) \right] \bar{k} \tag{3.60}
 \end{aligned}$$

The shear stress of the wall is:

$$\bar{\tau}_w = \frac{\mu_{eff} |\bar{S}_w|}{\delta n} \delta\bar{U}^\parallel \tag{3.61}$$

δn is the distance from P to wall.

3.5 Transformation between Rotational Frame and Stationary Frame

The blade swept region is stationary frame region. The velocity counted of this region is relative to rotational frame speed. The other region is stationary frame. The velocity counted in this region is absolute velocity. There are some transformation

between rotational frame and stationary frame.

If main grid P is in rotational frame (Fig 3.4), the velocity of P is relative velocity. The neighbor grid Cs is in stationary frame, the velocity of Cs is absolute velocity. Source term Q_Φ between this two grids should be corrected to Q'_Φ .

$$Q'_\Phi = Q_\Phi - a_c \bar{U}_{gf} \quad (3.62)$$

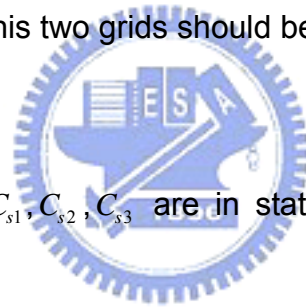
\bar{U}_{gf} is the speed of the interface of two grids.

The other neighbor grids, such as C_{r1} , C_{r2} , C_{r3} are also in rotational frame, it is unnecessary to correct.

If the main point is in stationary frame (Fig 3.5), the velocity of P is absolute velocity. The neighbor grid Cr is in rotational frame, and the velocity of it is relative velocity. Source term Q_Φ between this two grids should be corrected to Q'_Φ :

$$Q'_\Phi = Q_\Phi + a_c \bar{U}_{gf} \quad (3.63)$$

The other neighbor grids C_{s1} , C_{s2} , C_{s3} are in stationary frame, it is unnecessary to correct.



3.6 Solution Approach

1. Give an initial velocity \bar{U}^0 , pressure p^0 , k^0 , ε^0 and turbulent viscosity μ_t^0 .
2. Solve the momentum equation in order to receive speed \bar{U}^* .
3. Calculate the mass flux rate m^* then calculate equation of pressure correction to receive p' .
4. Correct velocity, pressure and mass flux rate and we receive \bar{U}^{**} , p^{**} 及 m^{**} .
5. Solve k equation and ε equation to receive k^* and ε^* then we calculate new turbulent viscosity μ_t^* .
6. Regard new value that we got as initial value, covered the step 2 again until it converges.

Chapter 4 Results and discussion for single impeller

4.1 Introduction

In this chapter, flow agitated by single disc turbine with various pitched blade angles is predicted by the Multiple Reference Frame method that is different from Shen's model. The flow field, power number, and pumping number resulting from present work are compared with Shen's work. The results are also compared with Ranade et al.'s experimental data when the impeller is located at the center of the vessel and the oblique angle of blades is 90 degree.

4.2 Geometry of stirred tank with single disc turbine

The geometry of stirred tank with single disc turbine is the same with Shen's work, but the definition of Multiple Reference Frame is different. In shen's model, the rotational frame was defined only at impeller blades swept region in radius direction and in axial direction; stationary frame was used on the other places (Fig 1.5). In present work, the rotational frame is defined encompass all the impeller and the flow surrounding it, and the other place is defined as stationary frame (Fig.1.6). The geometry of the stirred tank is shown at Fig.4.1. There are four baffles mounted vertically and equally spaced on the flat bottomed cylindrical vessel wall. The vessel is lidded and impeller rotates counterclockwise with top view. The shaft of the impeller is concentric with the axis of the vessel. The impeller has six blades on the disc; each of them equally spaced around the disc perimeter. We changed four geometrical parameters to affect the flow structure, they are oblique angle of blades α , the clearance between impeller center and vessel bottom C , the diameter of impeller D , and diameter of impeller disc d (Fig.4.2). The cylindrical coordinate system has been

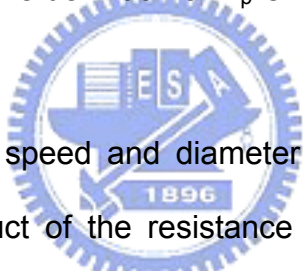
used with the origin located at the center of the impeller. Under the fully developed and steady flow conditions, flow in the baffled cylindrical vessel could be divided into two similar parts. We could just simulate one of them by using the periodic boundary condition. This could decrease the computational effort required. The calculation domain and grids of straight blades are shown in Fig.4.3 and the calculation domain and grids of pitched blade turbine are shown in Fig.4.4. Periodic boundary conditions were imposed in the surface of 0 and 180.

4.2.1 Comparison with experimental data of Ranade et al.

Before comparison with Ranade et al.'s experimental data, many numbers for telling the efficiency of different stirred tanks are introduced.

(a)Power number N_p : The definition of N_p is:

$$N_p = W / \rho N^3 D^5$$

 N and D are the rotational speed and diameter of the impeller respectively, W is determined to be the product of the resistance torque by the angular velocity. In experiments, the torque is directly measured. In the present numerical simulation, it is computed by summing the contributions due to (1) the pressure difference between the upstream and downstream faces of the blades, and (2) the wall shear stress on walls of shaft and impeller.

$$N_p = 2\pi N\tau / \rho N^3 D^5$$

τ is the torque generated by the pressure and shear force act on impeller blades when the impeller is rotating.

(b)Pumping number: the definition of pumping number is:

$$N_{Q_p} = Q_p / ND^3$$

Q_p is the flow rate of volume that fluid discharged by the impeller. N and D are as

defined previously. In order to analyze the flow conditions that surround the impeller swept region, we calculated the volume flow rate in four directions. First is the upper part of the impeller swept region, the rest three are lower, outer (tip), and inner of the impeller swept region. The positive number of volume flow rate is defined as fluid flow out from the impeller swept region, or the negative number of volume flow rate is defined as fluid flow into the impeller swept region.

(c) Pumping efficiency: The pumping efficiency is defined by the following equation

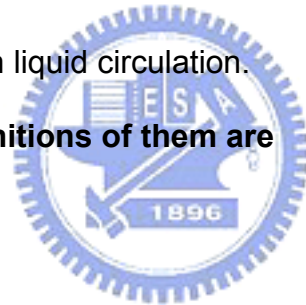
$$\eta = N_Q / N_P$$

Greater pumping effectiveness means greater liquid circulation for a given power consumption. Ranade et al. have shown that the mixing time (for a given homogeneity) decrease with an increase in liquid circulation.

(d) k^* and ϵ^* : The definitions of them are

$$k^* = \int_v \rho k dv / \rho N^2 D^5$$

$$\epsilon^* = \int_v \rho \epsilon dv / \rho N^3 D^5$$



k^* is the dimensionless kinetic energy of all the stirred tank, it is an index of kinetic energy of flow in stirred tank. ϵ^* is the dimension less local energy dissipation, it is an index of energy dissipation of flow in stirred tank.

Now we start to simulate the flow that agitated by Ranade's experimental model. The Geometry of the vessel is the same with Ranade's work. The stirred tank modeled in this study is standard configuration cylindrical vessels with four equal-spaced wall-mounted baffles of width $d=T/10$ (30mm) as shown in Fig.4.2. T is the vessel diameter; the vessel height $H=T=300$ mm. The impeller used is of diameter equal to one-third of the vessel diameter (100mm) with blade angle α equal to 90 degree. The width and length of the blades is $w=D/5$ (20mm) and $l=D/4$ (25mm)

respectively. The diameter of the disc is equal to $2D/3$ (67mm). The impeller is located halfway between the lid and the base, that is $C=T/2$ (150mm). The diameter of the shaft D_s is 19mm. Rotation speed is 5 rps counter-clockwise.

Fig.4.5 shows the radius profiles of radial, tangential, and axial velocity. Fig.4.6 shows the location of various Z/R . The location of $Z/R=0.933$ is close to the vessel bottom, and the location of $Z/R=0.2$ is close to the lower part of the impeller. Fig.4.5a can be seen that present work underpredicts the radial velocity near the bottom region of the vessel. The magnitude of maximum radial velocity near the bottom is around 0.05 times the tip speed in present work. But it is almost 0.1 times the tip speed in Ranade's experimental data. The radial profiles of radial velocity is better when $Z/R=0.2$. But there are still some underprediction near the shaft and some overprediction near the vessel wall. The most striking difference between Shen's data and present work occurs in the case of tangential velocity shown in Fig.4.5b. Shen's work predicted negative tangential velocity near the symmetry axis especially at the vessel bottom and present work shows better agreement. But there are still some underpredictions near the vessel bottom. Predicted radial profiles of axial velocity at various axial locations are compared with Ranade et al.'s experimental data and Shen's data in Fig.4.5c. The agreement can be said to be satisfactory except in the region of flow reversal. The difference between predictions and experimental data increases as the vessel bottom is approached.

The table below shows the comparison of Power number and Pumping number between present work, Ranade et al.'s experimental data, and Shen's work ($D=T/3$, $C=T/2$, $d=2D/3$, $\alpha=90^0$).

	Present Work	Ranade's Exp Data	Shen's Work
Power number	5.038	4.85	2.961
Pumping number	0.8429	0.75	0.7383

It shows that Shen's work seriously underpredict Power number. Multiple Reference Frame is used in problems that contain regions of nearly-stationary flow. This occurs in the region midway between the blades and baffles in a mixing vessel. In Shen's work, she defined the interface between rotational frame and stationary frame just next to the impeller blade tip that must not be a region of nearly-stationary flow. That may lead to inaccurate results. Following, we will re-do Shen's work and compare the result with Shen's data.

4.2.2 Grids test cases

Four sets of grids with different density are used to run the grids test. The total cells of them are 180000, 123360, 84480 and 46080 respectively. Fig.4.7 shows the radial profiles of radial, tangential, and axial velocity of the four kinds of grids. The table below shows the power number and pumping number of the four set of grids respectively.

	46080	84480	123360	180000
Power number	4.931	5.028	5.038	5.045
Pumping number	0.813	0.831	0.843	0.849

It is seen that the velocity profile distributions of these grid are very close except the 46080 grids and the power number and pumping number are almost independent of the grids. In order to raise the accuracy of the result and to decrease the computational effort required, we choose grid of 123360 cells as the computational grid.

4.3 The effects of blade angle on flow pattern for different off-bottom clearance. ($D=T/3$, $d=2D/3$)

4.3.1 The effects of blade angle on flow patterns when $C=T/2$. ($D=T/3$, $d=2D/3$)

We change the blade angle to observe the influence of the flow in the stirred tank when the impeller is located at the vertical center plane of the vessel. Fig. 4.8 shows the stream lines of various blade angles at the vertical plane of $\Phi = -30^\circ$. Φ is defined at Fig.1.5. We can see the flow field changes from axial flow to radial flow when the blade angle α changes from 47° to 48° . The blade angle that made the flow field changes is defined as critical angle. The critical angle in this case is 47° .

Fig.4.9 shows the angular profiles of Power number and Pumping number. The power number increases by the increases of the blade angle α . When the blade angle increases from 47° to 48° the Pumping number increases rapidly, but pumping number decreases rapidly, similar to the change of Power number and Pumping number at critical angle reporter by Chou [18]. This is the different from Shen's result. In Shan's work, the Power number and Pumping number increase smoothly in the same condition. Then we separate the Pumping number into four pars, they are flow rate out from the outer, inner, lower, and upper side of the impeller swept region. At the lower side of the impeller swept region, the flow rate increases by the increase of blade angle α until 47° . When the blade angle changes to 48° , the flow rate of lower side decreases rapidly, and continue decreasing when the oblique angle goes bigger. The flow rate of outer side increases rapidly when the blade angle α changes from 47° to 48° and continue increasing by the increasing of blade angle α . That the flow rate of outer side of impeller increase rapidly and the flow rate of lower side of impeller decrease rapidly is an apparent characteristic when the flow field changes from axial flow to radial flow. We can also find the critical angle by the angular profiles of flow rate except from the vertical plane of stream line.

Fig. 4.10 shows the angular profile of power number and pumping number

compare with Shen's work. The Power number and Pumping number of Shen's work are generally lower than the present work, especially at high blade angle. Fig. 4.11 shows the pressure contour of $\alpha=47^\circ$ and $\alpha=48^\circ$ at the vertical plane of $\Phi=-30^\circ$. The pressure gradient below the impeller of $\alpha=47^\circ$ is bigger than that of $\alpha=48^\circ$ and there is a high pressure in the right down position of the stirred tank.

4.3.2 The effects of blade angle on flow patterns when $C=T/3$. ($D=T/3$, $d=2D/3$)

Now we posit the impeller at one third height of the stirred vessel and observe the flow field. Fig.4.12 is the Stream lines of various blade angles at vertical plane of $\varphi=-30^\circ$. Critical angle in this case is found at 72° by the observation of Fig.4.12. The flow field changes from axial flow to radial flow when the impeller blade oblique angle changes from 72° to 73° .

Then we observe the angular profiles of power number and pumping number in Fig.4.13. The power number increases as the oblique angle increases, and it increases rapidly when the oblique angle increase from 72° to 73° . In the figure of Pumping number profile, the flow rate at lower side of the impeller increases by the increasing of oblique and reaches a maximum at about 50° of the oblique angle, then it decreases slowly by the increases of oblique angle and decreases rapidly when the oblique angle reaches critical angle. The flow rate at outer side of the impeller becomes from flowing into the impeller swept region to flowing out the impeller swept region by the increasing of oblique angle, and it increases rapidly when the oblique angle reaches the critical angle, and then keep slow increasing by the increasing of oblique angle. The flow rate through inner side of the impeller does not change a lot; it decreases slowly as the oblique angle increases. The flow rate through upper side of the impeller increases in the beginning and reaches a maximum value at about $\alpha=50^\circ$ and then decreases with the oblique angle decreases. Fig.4.14 is the angular profiles

of Power number and Pumping number compare with Shen's work. The critical angle of Shen's work is 63° in this condition. Power number in her case decreases rapidly when the oblique angle reaches critical angle. The quantity of Power number and Pumping number at Shen's work is lower than present.

Fig. 4.15 shows the pressure contour at the vertical plane of $\alpha = 72^\circ$ and $\alpha = 73^\circ$. There is an area of higher pressure at the right down corner of the vessel when the oblique angle is 72° . High pressure only exist at the upper side of the impeller disc when oblique angle is 72° , but high pressure exist both side of the impeller disc when the oblique angle is 73° . There is also a place where the pressure gradient is apparent that is about one third the stirred tank height near the wall with oblique angle equal to 73° . It is also the separation point of upper circulation and lower circulation.

4.3.3 The effects of blade angle on flow patterns when $C=T/4$. ($D=T/3$, $d=2D/3$)

By the observation of stream lines shown in Fig.4.16, we find the critical angle is 88° when the clearance between impeller and stirred tank bottom is one fourth the vessel height. Fig.4.17 shows the Power number and Pumping number of various impeller blade angles. The power number increases as the blade angle increases, and it decreases rapidly when the oblique angle increase from 88° to 89° , it is similar to the change of Power number and Pumping number at critical angle reporter by Shen [19]. In the figure of Pumping number profile shown in Fig.4.17, the flow rate at lower side of the impeller increases by the increasing of blade angle and reaches a maximum at about 55° of the impeller blade angle, then it decreases slowly by the increases of blade angle and decreases rapidly when the blade angle reaches critical angle. The flow rate at outer side of the impeller becomes from flowing in to flowing out the impeller swept region by the increasing of blade angle, and it increases rapidly when the blade angle reaches the critical angle, and then keeps slow increasing by

the increasing of blade angle.

Fig.4.18 shows the angular profile of Power number and Pumping number compare with Shen's work. The Power numbers and pumping numbers of both of them increase by the increasing of blade angle before the critical angle. The Power numbers of both present and Shen's work decrease rapidly and the Pumping numbers of them increase rapidly when the blade angle reaches critical angle. Fig.4.19 shows the pressure contour at the vertical plane of $\alpha = 88^\circ$ and $\alpha = 89^\circ$. There is a place where the pressure gradient is apparent that is about one fourth the stirred tank height near the wall with oblique angle equal to 89° . It is also the separation point of upper circulation and lower circulation.

4.3.4 The effects of pitched blade disc turbine position on flow patterns.

The impeller that of diameter equal to $D/3$ is posited in three different distances from the vessel bottom, they are $T/2$, $T/3$, and $T/4$ respectively. The critical angles of these three conditions are 47° , 72° , and 88° respectively. The less the clearance from impeller to vessel bottom is, the bigger the critical angle is. Fig.4.20 shows the flow field changes from axial flow to vertical flow. The flow field is easier to become axial flow when the clearance decreased. The flow fields of blade angle equal to 70° when the impeller is posited at three different locations are presented in Fig. 4.21. We can observe that when the blade angle is constant, the change of the clearance from vessel bottom to impeller will influence the flow field. The less the clearance is, the stronger the axial flow will be. This might because when the impeller is closer to the bottom, the fluid volume below the impeller is smaller. At the same impeller rotational speed, the fluid velocity of smaller volume will be faster and small blade oblique angle can produce large axial velocity component, this may be the reason why the flow field is easy to become axial flow when the clearance is small.

The power number increase rapidly when the oblique angle reaches the critical angle in the condition of $C=T/2$. This was happened in the flow field prediction of pitched blade impellers presented by Chou [18]. In the other hand, the power number decrease rapidly when the blade angle reaches the critical angle when $C=T/4$. This might because the effect of the impeller disc. When the flow field is axial flow, the flow below or above of the disc is baffled by the disc. The disc makes the fluid flow toward radial direction but the impeller blade force them flow down to form the axial flow. This may be the reason why the power number decreases rapidly when the flow field changed from axial flow to radial flow, because the impeller blades don't have to change flow direction in radial flow condition. When the impeller is located at $C=T/2$ with $disc=2D/3$, the effort of disc is not large enough, the power number increase rapidly just like the flow field that agitated by pitched blade turbine changes from axial flow to radial flow.



4.4 The effects of blade angle on flow pattern for different off-bottom clearance. ($D=T/3$, $d=3D/4$)

4.4.1 The effects of blade angle on flow patterns when $C=T/2$. ($D=T/3$, $d=3D/4$)

The stream lines of various blade angles at the vertical plane of $\Phi= -30$ is reported in Fig.4.22. By the change of stream lines, we can tell the critical angle is 37° . The power number, pumping number and pumping efficiency of radial profile are shown in Fig.4.23. The power number increases smoothly when the impeller blade angle reaches critical angle, so does the pumping number.

Predictions of Power number and Pumping number of this case are compared with Shen's result in Fig.4.24. Overall Pumping numbers of present work are higher than Shen's, especially at high impeller blade angle. The Pumping numbers reported

in present work are also higher than Shen's.

Fig. 4.25 shows the pressure contour of $\alpha=37^\circ$ and $\alpha=38^\circ$ at the vertical plane of $\Phi=-30$. High pressure only exist at the upper side of the impeller disc when blade angle is 37° , this may cause the higher pressure gradient on impeller blades and make the power number larger than that of oblique angle equal to 38°

4.4.2 The effects of blade angle on flow patterns when $C=T/3$. ($D=T/3$, $d=3D/4$)

Fig.4.26 is the Stream lines of various angle of impeller blades at vertical plane of $\varphi= -30^\circ$. Critical angle is found at 65° by the observation of Fig.4.26. The flow field changes from axial flow to radial flow when the impeller blade oblique angle changes from 65° to 66° . We observe the angular profile of power number and pumping number in Fig.4.27. The power number increases as the oblique angle increases, and it decreases rapidly when the oblique angle increase from 65° to 66° . The flow rate at lower side of the impeller increases by the increasing of blade angle and reaches a maximum at about 45° of the blade angle, then it decreases slowly by the increases of blade angle and decreases rapidly when the oblique angle reaches critical angle. Fig.4.28 is the angular profile of Power number and Pumping number compare with Shen's work. The critical angle of Shen's work is 59° in this condition. Power number in her case decreases rapidly when the oblique angle reaches critical angle. The quantity of Power number and Pumping number at Shen's work is lower than present.

Fig. 4.29 shows the pressure contour of $\alpha= 65^\circ$ and $\alpha= 66^\circ$ at the vertical plane of $\Phi=-30^\circ$. High pressure only exist at the upper side of the impeller disc when oblique angle is 65° , this may cause the higher pressure gradient on impeller blades and make the power number larger than that of oblique angle equal to 66°

4.4.3 The effects of blade angle on flow patterns when $C=T/4$. ($D=T/3$, $d=3D/4$)

By the observation of stream lines shown in Fig.4.30, we find the critical angel is

84° when the clearance between impeller and stirred tank bottom is one fourth the vessel height. The Power number and Pumping number of various impeller blade angles are shown in Fig.4.31. The power number increases as the oblique angle increases, and it decreases rapidly when the oblique angle increase from 84° to 85. The flow rate at lower side of the impeller increases by the increasing of blade angle and reaches a maximum at about 45° of the oblique angle, then it decreases slowly by the increases of oblique angle and decreases rapidly when the oblique angle reaches critical angle. The flow rate at outer side of the impeller increases by the increasing of oblique angle, and it increases rapidly when the oblique angle reaches the critical angle.

Fig.4.32 shows the angular profiles of Power number and Pumping number compare with Shen's work. The Power numbers of both present and Shen's work decrease rapidly and the Pumping numbers of both of them increase rapidly when the oblique angle reaches critical angle. Fig.4.33 shows the pressure contour at the vertical plane of $\alpha = 84^\circ$ and $\alpha = 85^\circ$. There is a place where the pressure gradient is apparent that is about one fourth the stirred tank height near the wall with oblique angle equal to 85°. It is also the separation point of upper circulation and lower circulation.

4.4.4 The effects of disc size on flow patterns.

Compare the flow field agitated by pitched blade disc turbines of different length of disc diameter. The table shows below is the critical angle of the flow field agitated by two different turbines of disc diameter $d=2D/3$ and $d=3D/4$ at three difference location.

	$C=T/2$	$C=T/3$	$C=1/4$
$D=T/3, d=2D/3$	47°	72°	88°

$D=T/3, d=3D/4$	37°	65°	84°
-----------------	------------	------------	------------

It shows that the critical angle with big disc is less than that with small disc. The impeller of big disc has better performance to force the fluid flow toward radial direction. The bigger disc has more area to baffle liquid than small one, it leads to bigger pressure gradient on the impeller blades. We can observe that the quantity of power number that rapidly decrease after the critical angle is bigger when the disc is larger.

4.5 The effects of blade angle on flow patterns for different off-bottom clearances. ($D=T/2, d=3D/4$)

4.5.1 The effects of blade angle on flow patterns when $C=T/2$. ($D=T/2, d=3D/4$)

Fig.4.34 is the Stream lines of various impeller blade angle of impeller blades at vertical plane of $\varphi = -30^\circ$. Critical angle is not found by the observation of Fig.4.34, all of the flow fields are axial flow. We observe the angular profile of power number and pumping number in Fig.4.35. The power number increases as the oblique angle increases. The flow rate at lower side of the impeller becomes from flowing out the impeller swept region to flowing into the impeller swept region by the increasing of blade angle, and the flow rate at outer side of the impeller increases by the increasing of blade angle. Fig.4.36 is the angular profile of Power number and Pumping number compare with Shen's work. The quantity of Power number and Pumping number at Shen's work is lower than present.

4.5.2 The effects of blade angle on flow patterns when $C=T/3$. ($D=T/2, d=3D/4$)

Now we posit the impeller at one third height of the stirred vessel and observe the flow field. Fig.4.37 is the Stream lines of various blade angle of impeller blades at the

vertical plane of $\varphi = -30^\circ$. Critical angle is found at 40° by the observation of Fig.4.37. The flow field changes from axial flow to radial flow when the impeller blade oblique angle changes from 40° to 41° . In the figure of Pumping number profile shown in Fig.4.38, the flow rate at lower side of the impeller increases by the increasing of oblique then it decreases rapidly when the oblique angle reaches critical angle. The flow rate at outer side of the impeller becomes from flowing in to flowing out the impeller swept region immediately after the impeller blade angle reaches the critical angle, and then keeps continuously increasing by the increasing of blade angle. Fig.4.39 is the angular profile of Power number and Pumping number compare with Shen's work. The critical angle of Shen's work is 39° in this condition. The quantity of Power number and Pumping number at Shen's work is lower than present.

4.5.3 The effects blade angle on flow patterns when $C=T/4$. ($D=T/2$, $d=3D/4$)

By the observation of stream lines shown in Fig.4.40, we find the critical angle is 65° when the clearance between impeller and stirred tank bottom is one fourth the vessel height. Fig.4.41 shows the Power number and Pumping number of various impeller blade angles. The power number increases as the blade angle increases, and it decreases rapidly when the oblique angle increase from 65° to 66° . At the lower side of the impeller swept region, the flow rate increases by the increase of oblique angle α and reach maximum at about 50° . When the oblique angle changes to 66° , the flow rate of lower side decreases rapidly, and continuously decreases when the oblique angle goes bigger. The flow rate of outer side increase rapidly when the oblique angle α changes from 65° to 66° and continuously increases by the increasing of blade angle α . Fig. 4.42 shows the angular profile of power number and pumping number compare with Shen's work. The Power number and Pumping number of Shen's work are generally lower than the present work, especially at high critical

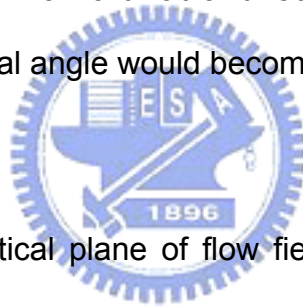
angle.

4.5.4 The effects of impeller diameter on flow patterns.

The table shows below is the critical angle, resulted by different impeller locations, compared between different impeller sizes. All of the impellers are with disc diameter equal to three-fourth the impeller diameter.

	C=T/2	C=T/3	C=T/4
D=T/3 d=3D/4	37°	65°	84°
D=T/2 d=3D/4	none	40°	65°

It shows that the critical angle decreases when the diameter of impeller increases. The bigger the impeller diameter is, the bigger the disc diameter. Bigger disc have bigger area to force fluid flow forward radial direction, makes the flow field easier to form radial flow. So the critical angle would become less.



4.6 Discussion

Fig.4.43 shows the vertical plane of flow field at different distance from blade (D=T/3 d=3D/4 C=T/3). At $\Phi=0^\circ$, the fluid flow into the impeller swept region at the upper side of blade and form a vortex at the up-right corner. The fluid flow downward out of the impeller swept region at the lower side of the blade when $\alpha=65^\circ$ as the fluid flow out of the impeller swept region at radial direction at the lower side of the blade when $\alpha=66^\circ$. When $\Phi=8^\circ$ the vortex move out of the impeller blade tip side and get a little sinking. When $\Phi=16^\circ$ the vortex move more out then $\Phi=8^\circ$ and it sink to the middle of the impeller swept region. At $\Phi=24^\circ$ the impeller has already dissipated.

The pressure contours of different blade angles at the vertical plane of $\Phi=-30^\circ$ is shown in Fig.4.44 (D=T/3 d=3D/4 C=T/3). The pressure contours of $\alpha=50^\circ$ and $\alpha=65^\circ$ are similar, high pressure only exit on the top side of the impeller disc. As the blade angle changes to 66° the pressure gradient between upper and lower side of impeller

disc become small. There are high pressure regions on both sides of the impeller disc at radial flow as high pressure region only exist on upper side of the impeller disc at axial flow. The pressure contours of $\alpha=66^\circ$ and $\alpha=90^\circ$ are similar.

Fig.4.45 and Fig.4.46 shows the pressure contours and stream lines on blade surface for different impeller angles respectively. The pressure contour changes a lot between $\alpha=65^\circ$ and $\alpha=66^\circ$ on face facing wind, we can observe the impeller disc do lots of favor. It is almost the same at all the lee face except $\alpha=90^\circ$, which is much more symmetric to the center line. The pressure act on blade of $\alpha=65^\circ$ is higher then that of $\alpha=66^\circ$. Stream lines on blade surface of the first two axial flows shown in Fig.4.46 are almost the same. By observation of the stream lines on face facing wind, the blade forces the fluid flow downward when $\alpha=65^\circ$ and forces the fluid flow outward tip direction when $\alpha=66^\circ$. The fluid flow into the upper side of the lee blade face when $\alpha=50^\circ$, 65° and 66° form single vortex behind the blade. The fluid flow into both the upper and lower side of the lee blade face when $\alpha=90^\circ$ and form two vortices behind the blade.

In Fig.4.47, the flow out angle β was defined. First we connect the tip of the impeller disc and the separation point of upper and lower circulation. The angle between this line and the horizontal line extend from the impeller disc is defined as flow-out angle β . Fig.4.48 is the angular profiles of flow-out angle for different off-bottom clearance at three conditions. The flow-out angle of axial flow is located between sixty and eighty degree. When the flow field changes to radial flow, the flow-out angle decreases rapidly. The flow-out angle of radial flow is located between zero degree and twenty degree. The flow-out angle changes near-linearly before and after the critical angle.

Fig.4.49 and Fig.4.50 shows the radial profiles of power number and pumping

number for different off-bottom clearance. In case of ($D=T/3$ $d=2D/3$) the power number of $C=T/2$ and $C=T/3$ increase rapidly as the power number of $C=T/4$ decrease rapidly. In the other two cases power number of $C=T/2$ increase smoothly and power number of $C=T/3$ and $C=T/4$ increase by the increasing of blade angle and decrease rapidly after critical angle and then keep increasing. By observation of Fig.4.49 the critical angle will be bigger when the clearance C is smaller, the degree of power number that decrease rapidly after passing through the critical angle will be larger when the clearance C is smaller. Except the case of ($D=T/3$ $d=2D/3$ $C=T/2$), the pumping number will increase after the blade angle passes through the critical angle. The degree of increase of pumping number will be bigger when the clearance C becomes smaller. Fig.4.51 and Fig.4.52 show the radial profiles of k^* and ϵ^* for different off-bottom clearance. The k^* increases with the increase of blade angle and decreases rapidly after the blade angle pass through the critical angle and then keeps increasing. The ϵ^* increases with the increase of blade angle and increases rapidly after the blade angle pass through the critical angle and then keeps increasing. Fig.4.53 shows the radial profile of pumping efficiency for different off-bottom clearance. The pumping efficiency decreases with the increase of blade angle and increases rapidly when the blade angle passes through the critical angle and then keeps decreasing. The pumping efficiency is around 0.2 when the blade angle is close to 90 degree for all the cases. Fig.4.54 shows the stream lines and pressure contours of the stirred tank with impeller oblique angle $\alpha=70^\circ$ at different vertical plane. The vertical plane of $\Phi=-40^\circ$ and $\Phi=-50^\circ$ are in front and in back of the baffle respectively, this leads to the stream lines irregular near the vessel wall. When $\Phi=0^\circ$ and $\Phi=150^\circ$, the upper side of the blade swept region is behind the blade and the lower side of the blade swept region is in front of the blade. This leads to low pressure on the upper

side of the blade swept region and high pressure on the lower side of the blade swept region. The location of high pressure on the side wall corresponds to the separation point of upper and lower circulation.



Chapter 5 Results and discussion for dual impeller

5.1 Introduction

In this chapter, flow agitated by dual disc turbine with straight blade is predicted by the Multiple Reference Frame method and compare the results with the experimental data of Rutherford et al. [9] and numerical predictions of Micale et al. [22]. Rutherford et al. presented that the flows depended strongly on the clearance of lower impeller above the base of the vessel (C1), the separation between the impellers (C2), and the submergence (C3) of the upper impeller below the top of the liquid column height. The stirred reactor configuration is shown in Fig.5.1. When these distances were varied, three stable and four unstable flow patterns were observed. In present work, we located the impellers to model the three stable patterns.

5.2 Multiple reference frames

The MRF model utilizes the fact that for those geometries where the clearance between the impeller and the baffles is comparable with or greater than the impeller diameter, the flow pattern in the vicinity of the impeller is unaffected by the rest of the tank, and thus is time-independent with respect to the impeller. The flow in this region can thus be calculated as a time independent problem in the frame of reference co-rotating with the impeller. At some distance away from the impeller it is assumed that the flow is cylindrically symmetric, and so beyond this distance the flow is time-independent in the frame of reference of the tank. The flow here can be calculated as a time-independent problem in the stationary frame of the tank, and the two flows are coupled appropriately at the boundary between the frames. The technique is clearly appropriate for tank geometries with sufficient spacing between

the impeller blades and the baffles.

5.3 The geometry of the stirred tank.

The geometry of the stirred tank is the same with Rutherford et al.'s experimental model shown in Fig.5.1. In all cases, the vessel height is $H=T$, the width of the four baffles is $b=0.1T$, and the impeller diameter is $D=T/3$. Both impellers are standard Rushton turbines, with the blades aligned in the same vertical planes. Three stable flow patterns were observed during the flow visualization experiments with different lower impeller clearance (C1), impeller separation (C2), and upper impeller submergence (C3). The cases that are numerically simulated are summarized in the table shown below.

Case	C1	C2	C3	Notes
A	0.25T	0.5T	0.25T	Parallel flow
B	0.33T	0.33T	0.33T	Merging flow
C	0.15T	0.5T	0.35T	Diverging flow

They correspond to the parallel flow, merging flow, and diverging flow. Because of the different location of the impellers, the definition of multiple reference frame of each of them is different. Fig.5.2, 5.3, 5.4 shows the Multiple Reference applied to parallel flow, merging flow, and diverging flow respectively..

5.4 Result and discussion

For Parallel flow a comparison of prediction obtained by different impeller modeling technique with experimental LDV data is reported in Fig.5.5 and Fig.5.6. All graphs are for a plane at 45 degree between two baffles. Fig.5.5 reports the flow field of velocity vector. The MRF correctly predict the overall flow pattern in the stirred tank, including the recirculation centers and the spreading of the radial jet issuing from the

impeller. Contour plots of the turbulence energy k (normalized by V_{tip}^2) are compared in Fig.5.6. Levels of turbulent energy are under predicted by all computational methods. But the MRF predictions are in better agreement with the experimental results.

Predictions of the velocity and turbulence field for merging flow are compared with experimental result in Fig.5.7 and Fig.5.8. Fig.5.7 shows that the MRF technique successfully reproduces the characteristic of merging flow pattern that is observed in experimental for this configuration. The experimental velocity vectors show that the distortion of the radial jets issuing from the impellers, due to the attractive interaction between the two streams (a phenomenon akin to the Coanda effect observed in the near-wall planar jets), extends upstream to the impeller periphery. A close examination of the vector plots in Fig.5.7 reveals that all the three numerical method actually over-predict the convergence of the two impeller streams. Turbulence energy contours plots are shown in Fig.5.8. Levels of k are under-predicted by both the IO and SG method, so does the MRF method, but the underprediction level of MRF is lower then the other two.

The results for diverging flow are reported in Fig.5.9 and Fig.5.10. All the three methods can correctly reproduce the characteristic attachment of the lower stream to the bottom wall, but overpredict its downward curvature (the angle with respect to the horizontal is about 30° in the experiments, but the numerical prediction exhibit 45° - 55°). Contour plots of the turbulent energy k are reported in Fig 5.10. The agreement of SG, IO, and MRF predictions with the experimental result is of the same order as that observed for the merging flow case.

As a final comparison, the table showed below reports experimental and computed values of the power number, N_p .

Case	Experimental	IO	SG	MRF
Parallel flow	10.0	8.2	10	9.5
Merging flow	8.4	6.9	8.2	4.5
Diverging flow	9.5	4.5	8.4	15.9

The experimental value of N_P found for the parallel flow is about twice the value that most commonly reported in the literature for tanks stirred by single disc turbine. This confirms that the two impeller streams interact only weakly in this configuration. The experimental data shows that N_P decreases slightly in the diverging flow and more significantly in the merging flow case. The trend is correctly reproduced only by the SG or IO simulation. The power number of MRF do good agreement only in the parallel flow case but there are great inaccuracy on the merging and diverging flow cases. That might because there is no sufficient space between the lower impeller and the vessel bottom in diverging flow or between the two impellers in merging flow. When the impellers and walls are sufficiently separated, the region between them may contain nearly-stationary flow, we have sufficient physical meaning to define the interface between rotational frame and stationary frame on it, but not in the diverging flow or merging flow. This may be the reason that the power number is incorrect.

Chapter 6 Conclusion

1. The flow field will change by the oblique angle of impeller blades. Small oblique angle will bring axial flow and large oblique angle will bring radial flow. When the oblique angle increase to a certain angle, the flow field will change from axial flow to radial flow. The significant angle is defined as critical angle.
2. The definition of the multiple reference frames does really affect the computational prediction result. In Shen's work, the rotational frame is defined only at the range of impeller blade in radius direction and in axial direction; stationary frame is used on the other places. In present work, the rotational frame is defined encompass all the impeller and the flow surrounding it, and the other place is defined as stationary frame. For the second condition the interface between the rotational frame and stationary frame may be a nearly-stationary flow, and it would be better for MRF technique to apply to. The result shows that the Power number of present work has better agreement on experimental data.
3. When the flow field is axial flow, the flow below or above of the disc is baffled by the disc. The disc makes the fluid flow toward radial direction but the pitched impeller blade force them flow down to form the axial flow. When the flow field is radial flow, the fluid flow out the disk and the impeller blades continues force them toward the same direction to from radial flow. The pressure act on impeller blades in first condition would be bigger then that in second condition. This may be the reason why the power number decreases rapidly when the flow field changed from axial flow to radial flow. As the disc is bigger, this circumstance will be more obvious. Bigger impeller disc brings bigger decrease of power number when the flow field changes from axial flow to radial flow.

4. In the condition of $D=T/3$, $d=2D/3$, $C=T/2$, the power number increase rapidly when the oblique angle reaches critical angle. This is because the effect of disk is smaller than the effect that when the flow field change from radial flow to axial flow the pressure act on blades increase rapidly reported by Chou[18].
5. The less the clearance from impeller to vessel bottom is, the bigger the critical angle is. The less the clearance is, the stronger the axial flow will be. This might because when the impeller is closer to the vessel bottom, the fluid volume below the impeller is smaller. At the same impeller rotational speed, the fluid velocity of smaller volume will be faster and small oblique angle can produce large axial velocity component, this may be the reason why the flow field is easy to become axial flow when the clearance is small.
6. In cases of dual impeller turbines, MRF technique can predict the parallel flow well, but not the merging flow or diverging flow. That might because there is no sufficient space between the lower impeller and the vessel bottom in diverging flow or between the two impellers in merging flow. When the impellers and walls are sufficiently separated, the region between them may contain nearly-stationary flow, we have sufficient physical meaning to define the interface between rotational frame and stationary frame on it, but not on merging flow and diverging flow. Though the MRF technique can predict the velocity and turbulence field well on merging and diverging flow, but there are still inaccuracies on power number.

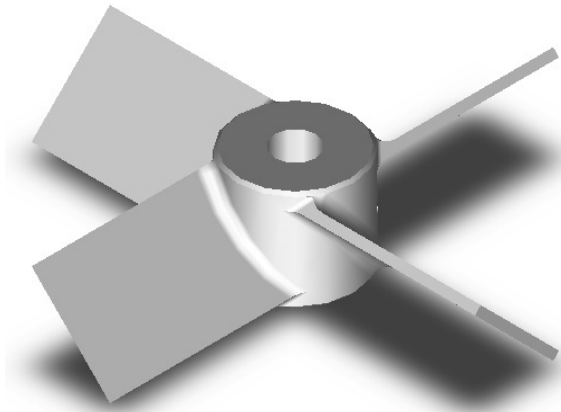
Reference

- [1] J.COSTES and J.P.COUDERC, "Study by laser Doppler anemometry of the turbulent flow induced by a Rushton turbine in a stirred tank: influence of the size of the units- Part 1: mean flow and turbulence", Chemical Engineering Science, Vol 43, No10, pp.2751-2764, 1988.
- [2] H.WU and G.K.PATTERSON, "Laser-Doppler measurements of turbulent flow parameters in a stirred mixer", Chemical engineering science, Vol.44, No.10, pp.2207-2221, 1989.
- [3] V.V.RANADE and J.B.JOSHI, "Flow generated by a disc turbine: part 1 experimental", Transactions of the Institution of Chemical Engineers, Vol.68, part A, pp.19-33, 1990.
- [4] M. YIANNESKIS AND J. H. WHITELAW, "On the structure of the trailing vortices around Rushton turbine blades", Transactions of the Institution of Chemical Engineering, Vol. 71, Part A, pp. 543-550, 1993.
- [5] V. P. MISHRA and J. B. JOSHI, "Flow generated by a disc turbine: part III: Effect of impeller diameter, Impeller Location and Comparison with other radial flow turbines", Transactions of the Institution of Chemical Engineering, Vol. 71, Part A, pp. 563-573, 1993.
- [6] V. P. MISHRA and J. B. JOSHI, "Flow generated by a disc turbine: part IV: Multiple impellers", Transactions of the Institution of Chemical Engineering, Vol.72, Part A, pp. 657-668, 1994.
- [7] K. C. LEE and M. YIANNESKIS, "Turbulence properties of the impeller stream of a Rushton turbine, American Institute of Chemical Engineering Journal, Vol. 44, No.1, pp.13-24, 1998.
- [8] V. V. Ranade, M. Perard, N. Lesauze, C. Xuereb and J. Bertrand, "Trailing

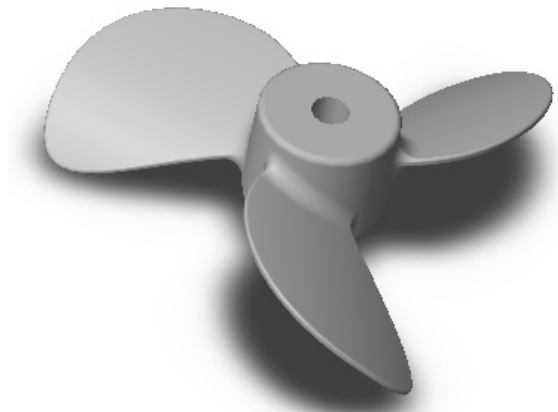
- vortices of Rushton turbine: PIV measurements and CFD simulations with snapshot approach” Transactions of Institution of Chemical Engineering, Vol. 79 part A, pp. 3-12, 2001.
- [9] K. RUTHERFORD, K. C. LEE, S. M. S. MAHMOUDI and M. YIANNESKI, “Hydrodynamic characteristics of dual Rushton impeller stirred vessels”, American Institute of Chemical Engineering Journal, Vol. 42, No.2, pp. 332-346, 1996.
- [10] J. MARKOPOULOS, E. BABALONA, and E. TSILIOPOULOU, “Power consumption in agitated vessels with dual Rushton turbines: Baffle length and impeller spacing effects”, Chemical Engineering Technology, Vol.27, No.11, pp. 1212-1215, 2004.
- [11] V. V. RANADE and J. B. JOSHI, “Flow generated by a disc turbine: part II: Mathematical modelling and comparison with experimental data”, Transactions of the Institution of Chemical Engineering, Vol. 68, Part A, pp.34-50, 1990.
- [12] J. Y. LUO, A. D. Gosman, R. I. Issa, J. C. Middleton, and M. K. Fitzgerald. “Full flow field computation of mixing in baffled stirred vessels”, Institution of Chemical Engineers, vol.71, part A, 1993.
- [13] J. Y. LUO, R, I, ISSA and A. D. GOSMAN, “Prediction of impeller induced flow in mixing vessels using multiple frame of reference”, ICHEME Symposium Series, No. 136, pp. 549-556, 1994.
- [14] Albert D. Harvey III, Stewart P. Wood and Douglas E. Leng. “Experimental and computational study of multiple impeller flows”, Chemical Engineering Science, vol. 52, No. 9, pp. 1479-1491, 1997
- [15] G. TABOR, A. D. GOSMAN and R. I. ISSA, “Numerical simulation of the flow in a mixing vessel stirred by a Rushton turbine”, I. Chem. E. Fluid Mixing V: UK

conference on Mixing, Bradford, 1996.

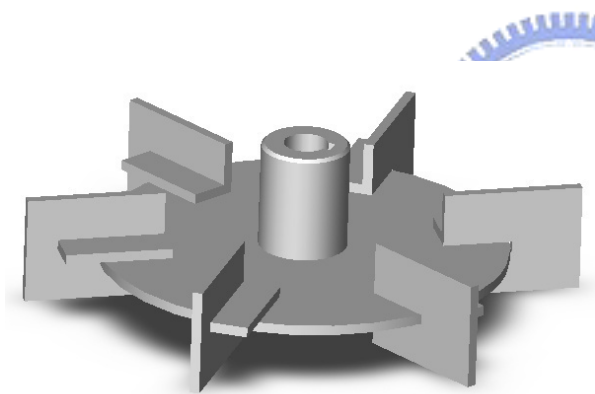
- [16] R. M. JONES, A. D. HARVEY III, and S. ACHARYA, "Two-equation turbulence modeling for impeller stirred tanks", Transactions of the ASME, Journal of Fluids Engineering, Vol.123, pp. 640-648, 2001
- [17] Yu-Chang Hu, "Calculation of the Flow in Impeller Stirred Tanks", National Chiao Tung University, Thesis for Master Degree, 2003.
- [18] Jian-Ren Chou, "Flow analysis in a Tank Agitated by Pitched-Blade Impellers", National Chiao Tung University, Thesis for Master Degree, 2004.
- [19] Shih-Jhen Shen, "Analysis of the Flow Agitated by Disc Turbines with Pitched Blades", National Chiao Tung University, Thesis for Master Degree, 2005.
- [20] Z. Jaworski, K. N. Dyster and A. W. Nienow, "The effect of size, location and Pumping direction of pitched blade turbine impellers on flow patterns: LDA measurements and CFD predictions", Transactions of Institution of Chemical Engineers, vol. 79, part A, pp. 887-894, 2001.
- [21] Albert D. Harvey III and Cassian K. Lee, "Steady-state modeling and experimental measurement of a baffled impeller stirred tank", American Institute of Chemical Engineering Journal, vol. 41, No. 10, pp. 2177-2186, 1995.
- [22] G. MICALÈ, A. BRUCATO, and F. GRISAFI, "Prediction of flow fields in a dual-impeller stirred vessel", American Institute of Chemical Engineering Journal, Vol. 45, No 3, pp. 445-464, 1999.
- [23] D. B. Spalding and B. E. Launder, "The Numerical computation of turbulence flows", Computer Method in Applied Mechanics and Engineering, Issue 3, pp. 269-289, 1974



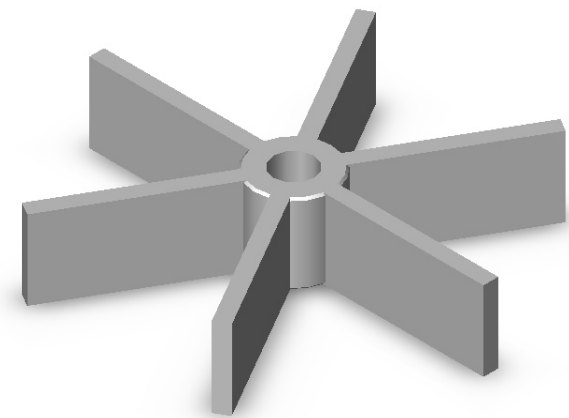
(a) Pitched blade impeller



(b) Propeller



(c) Rushton turbine



(d) Straight blade impeller

Figure 1.1 Various impellers

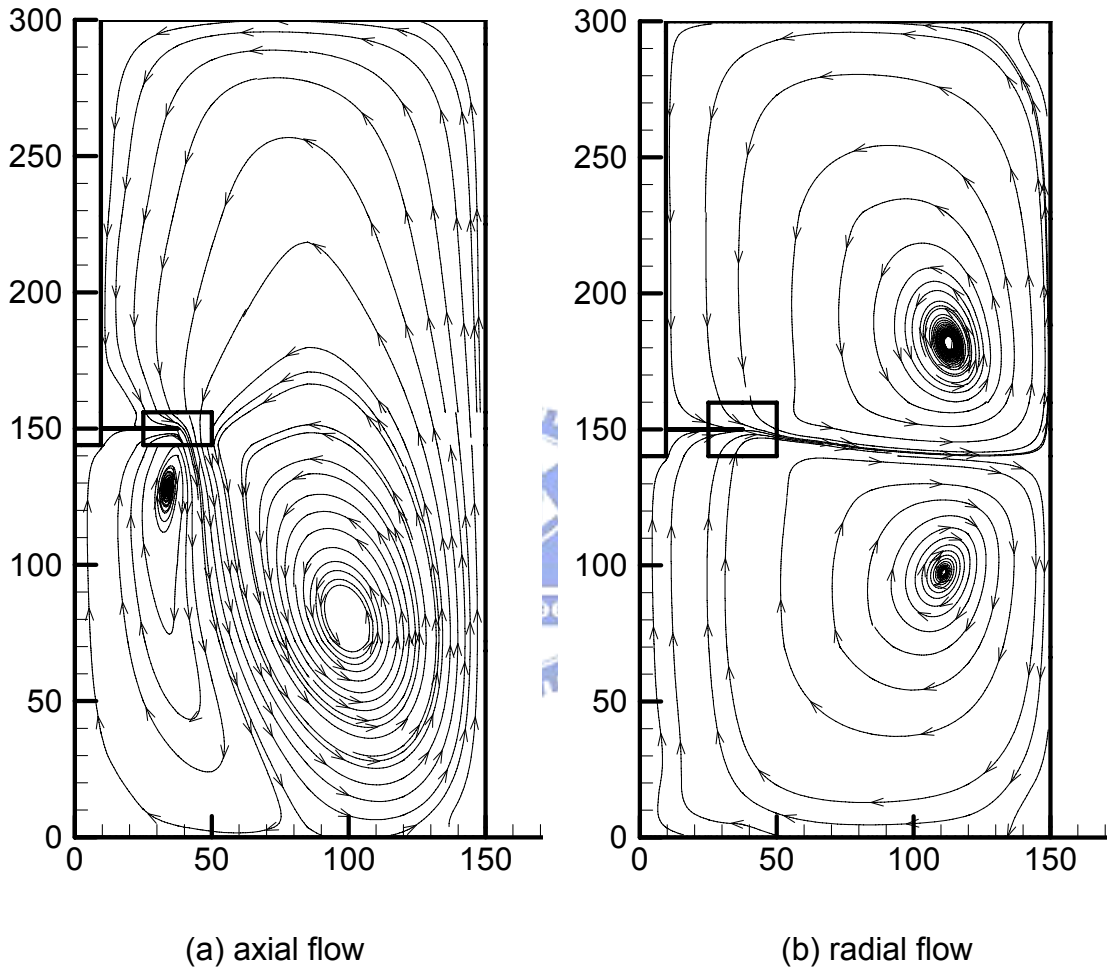
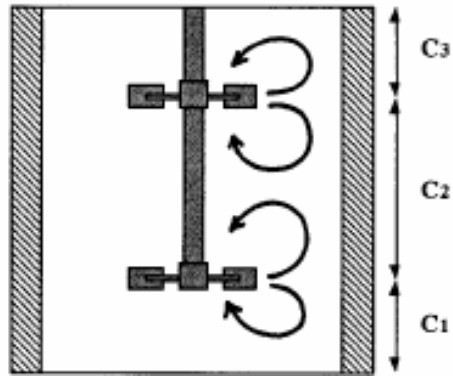
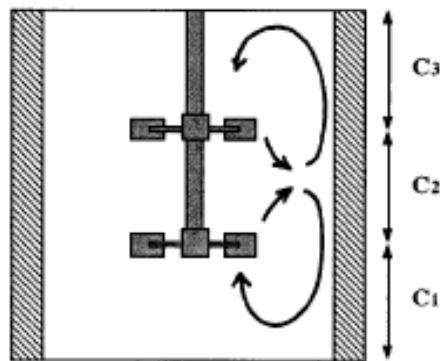


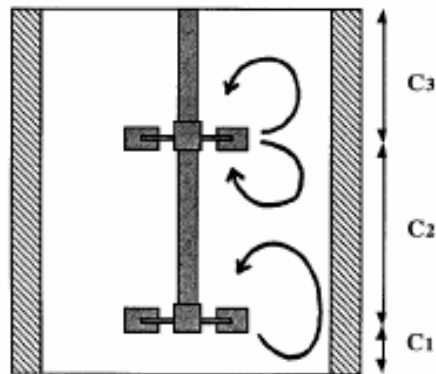
Figure 1.2 Axial flow and radial flow



(a) $C1=T/4$, $C2=T/2$, $C3=T/4$



(b) $C1=T/3$, $C2=T/3$, $C3=T/3$



(c) $C1=0.15T$, $C2=0.5T$, $C3=0.35T$

Figure 1.3 Flow patterns for three geometrical configuration studied: (a) parallel flow;
(b) merging flow; (c) diverging flow

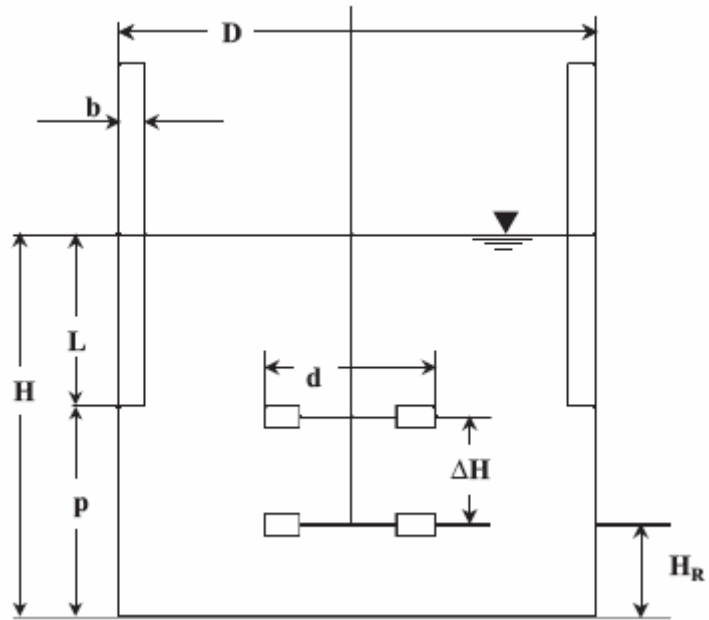


Figure 1.4 Dual Rushton turbine vessel with variable baffle length



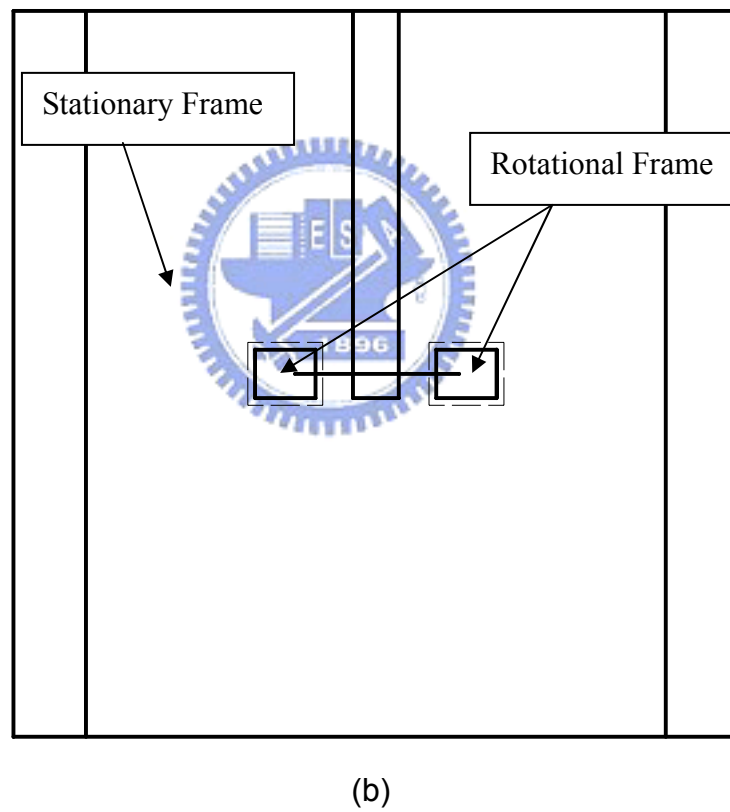
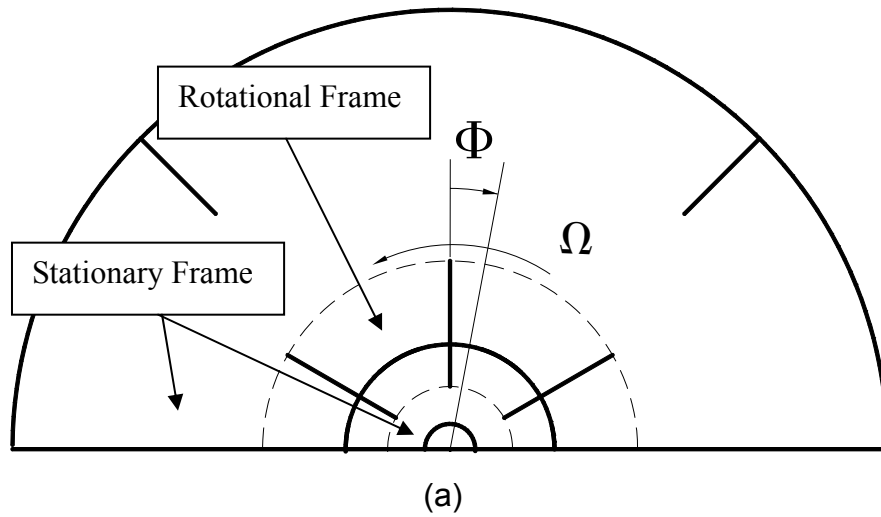
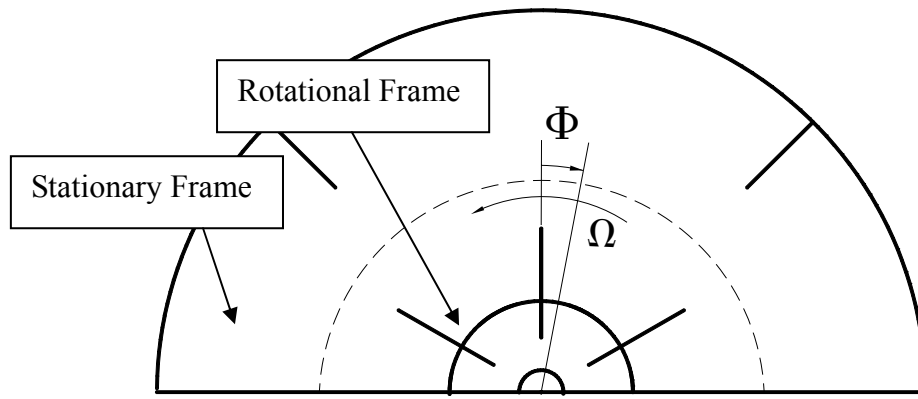
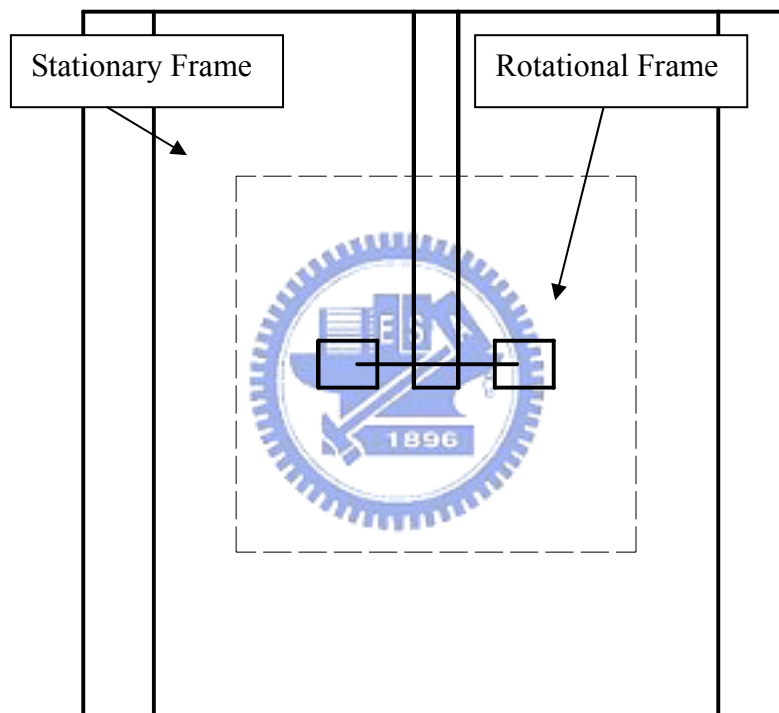


Figure 1.5 Rotational and stationary frame of Shen's model (a) Horizontal plane (b) Vertical plane



(a)



(b)

Figure 1.6 Rotational and stationary frame of present work (a) Horizontal plane (b) Vertical plane

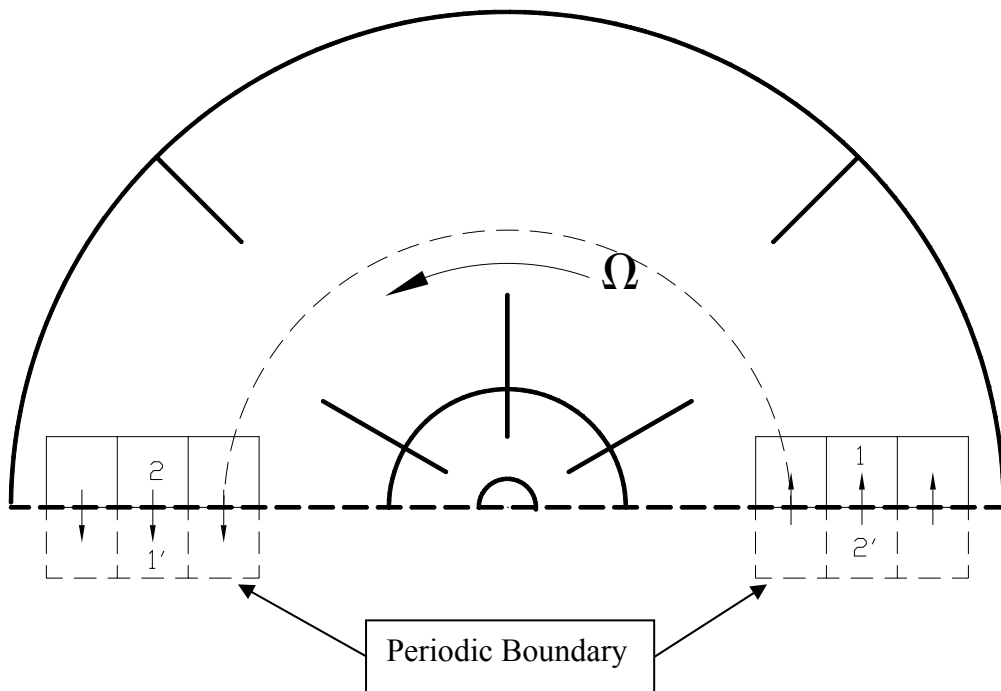


Figure 2.1 Periodic boundary conditions



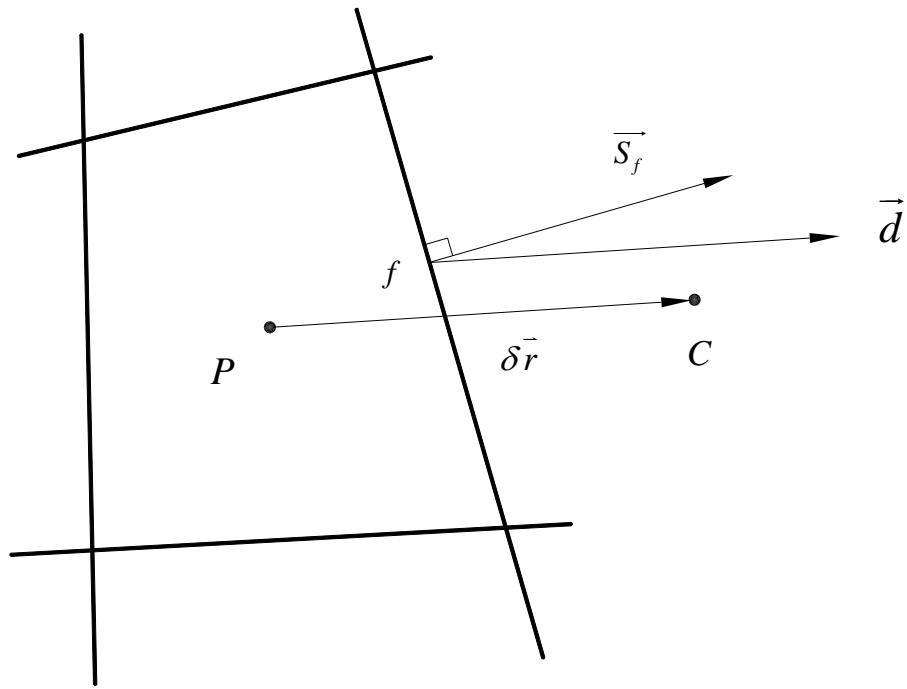


Figure 3.1 Over-relaxed approach

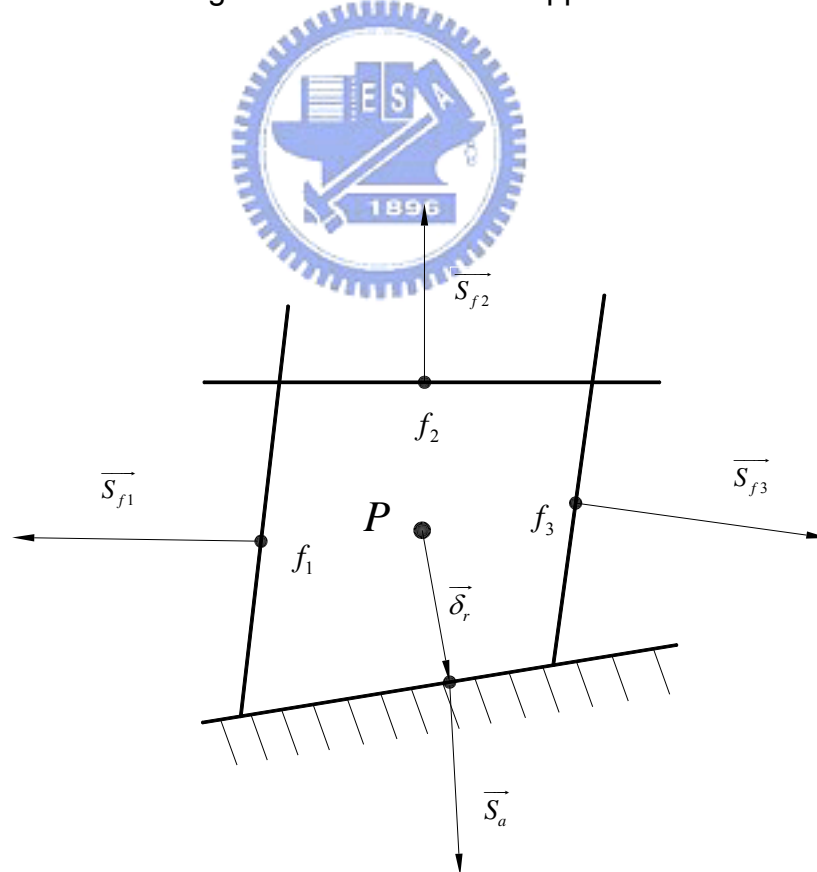


Figure 3.2 Calculation of boundary pressure

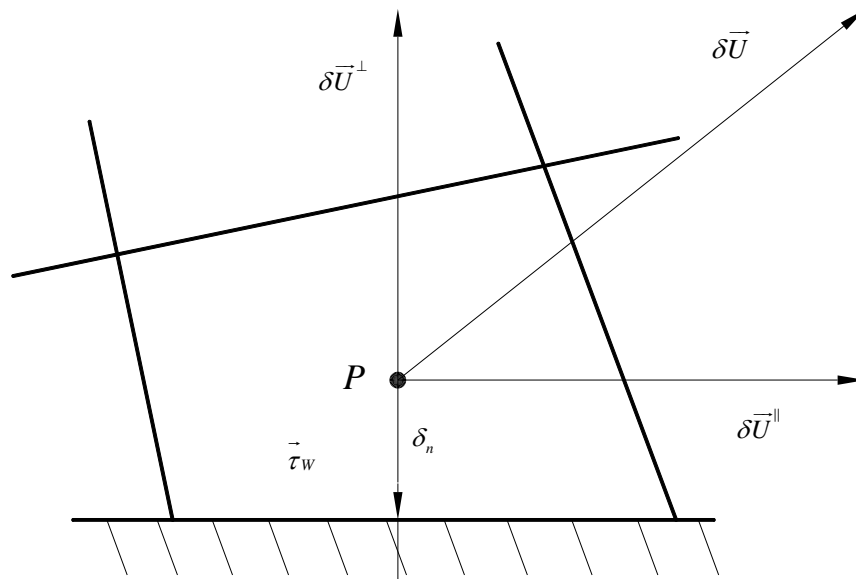
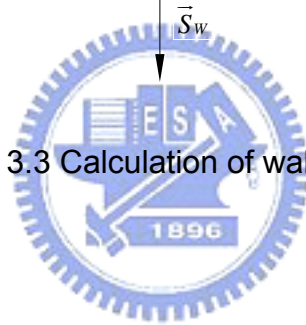


Figure 3.3 Calculation of wall shear stress



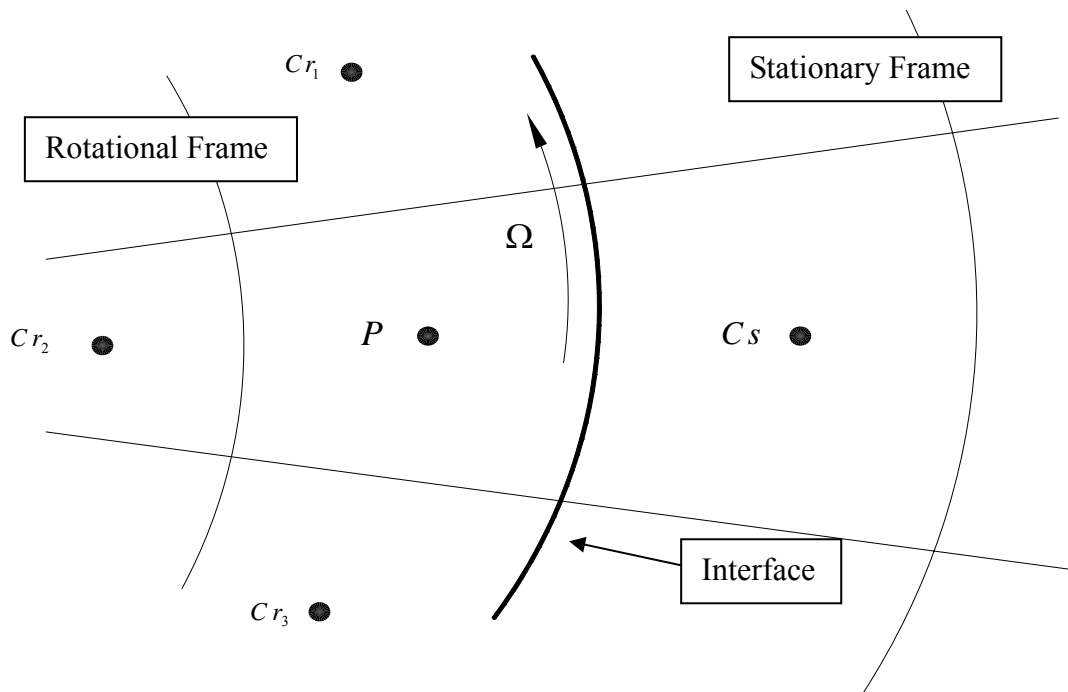


Figure 3.4 Calculated grids in rotational frame

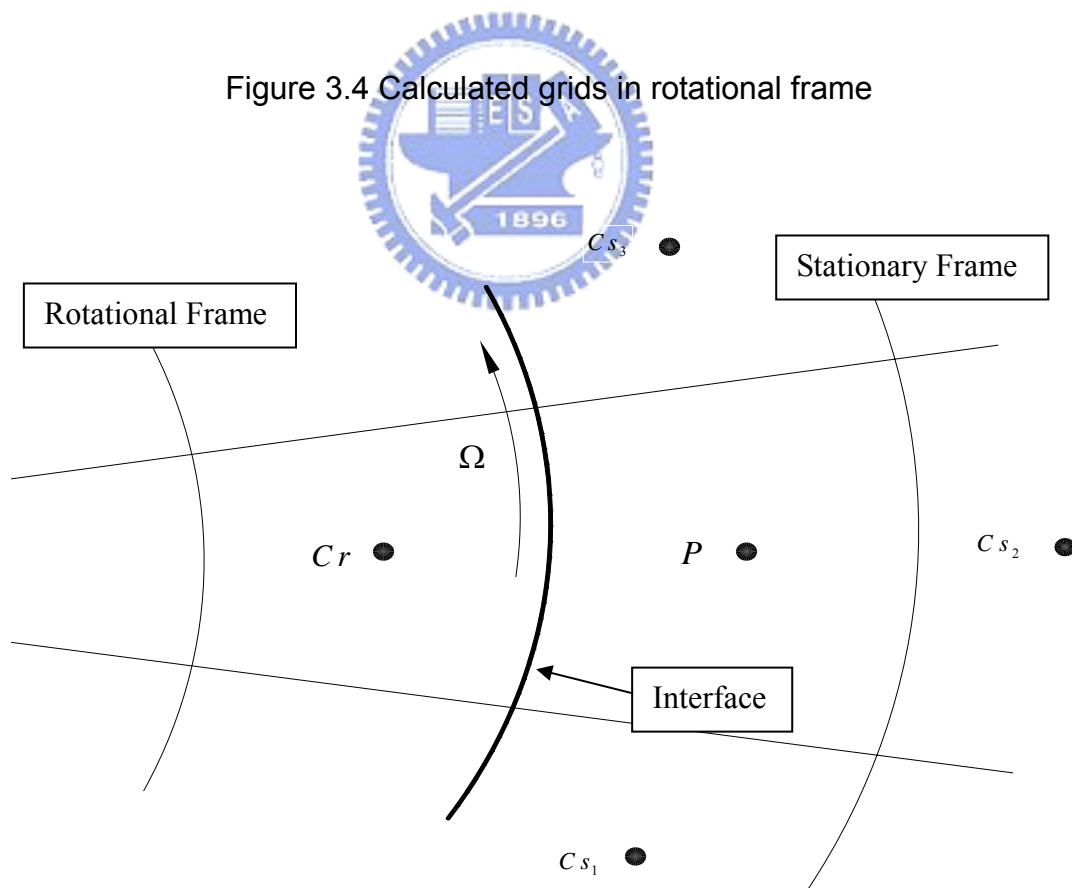


Figure 3.5 Calculated grids in stationary frame

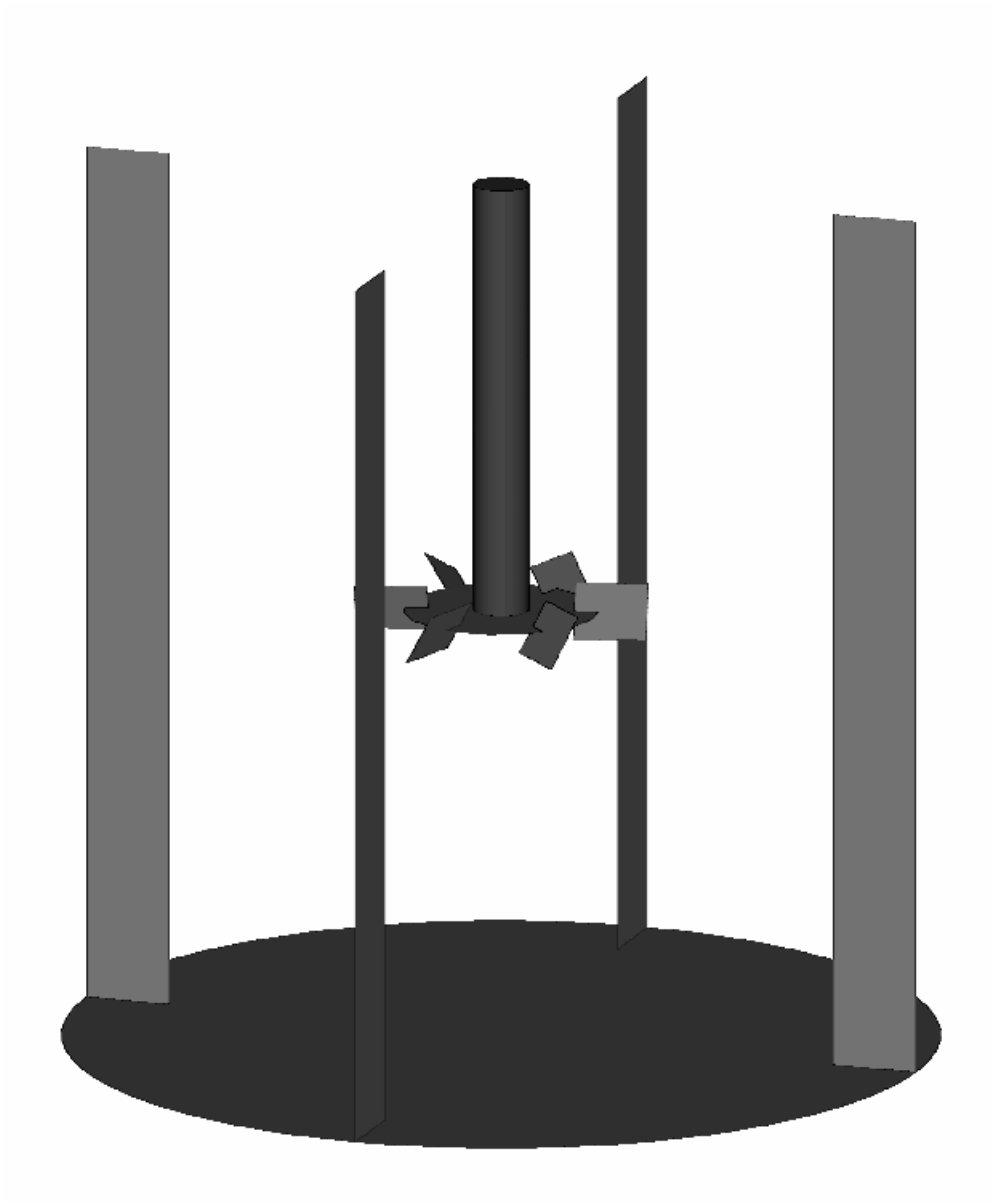


Figure 4.1 Geometric of single impeller stirred tank

α

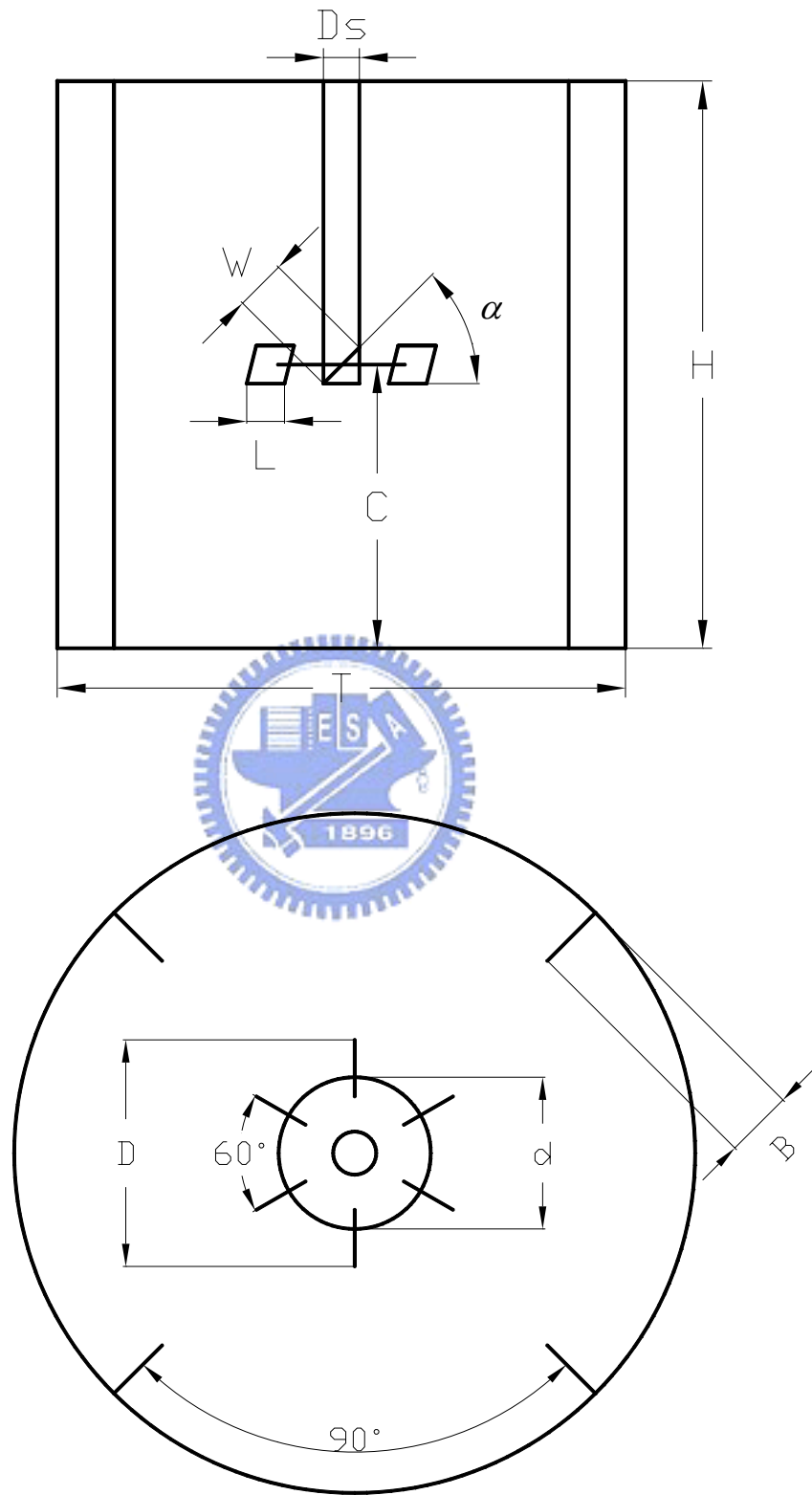
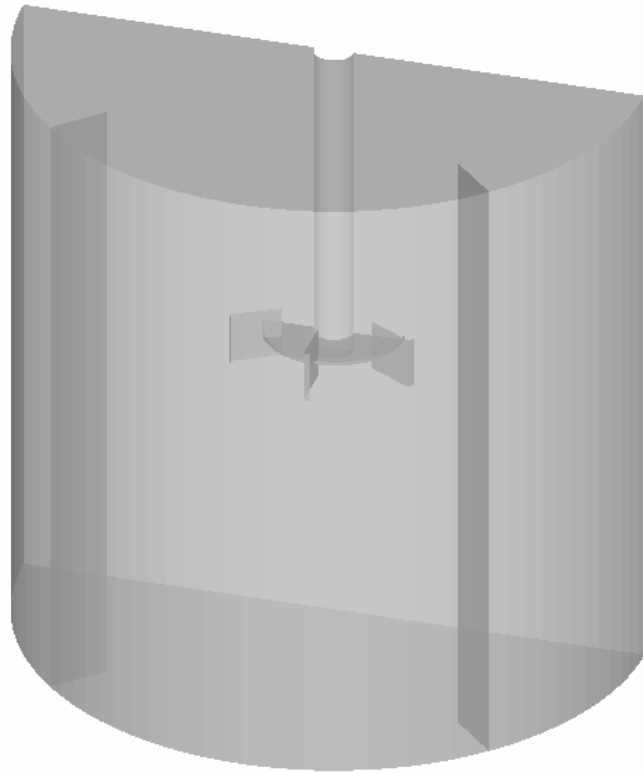
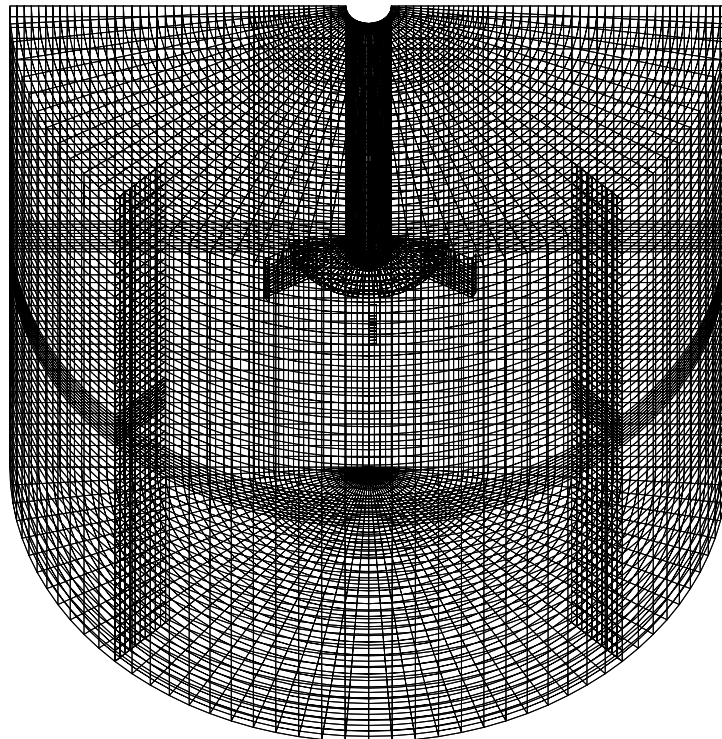


Figure 4.2 Geometrical parameters of stirred tank



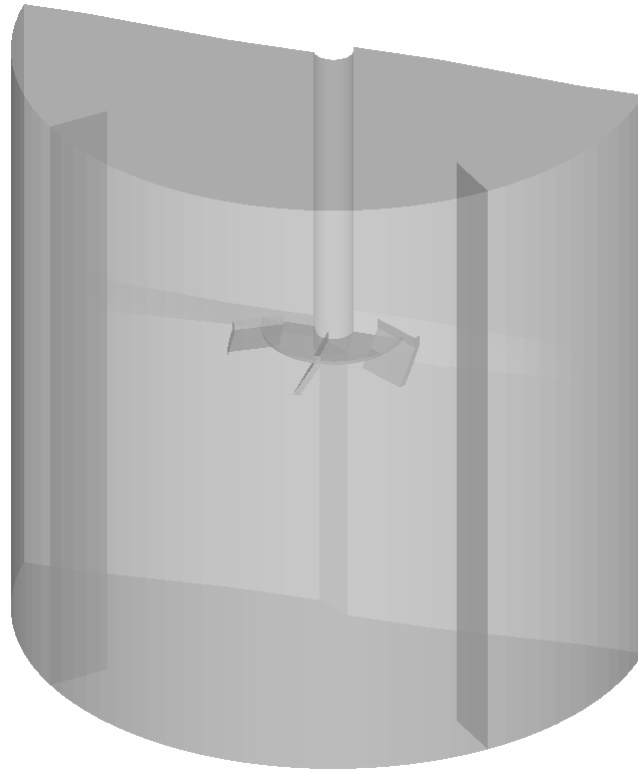
(a)



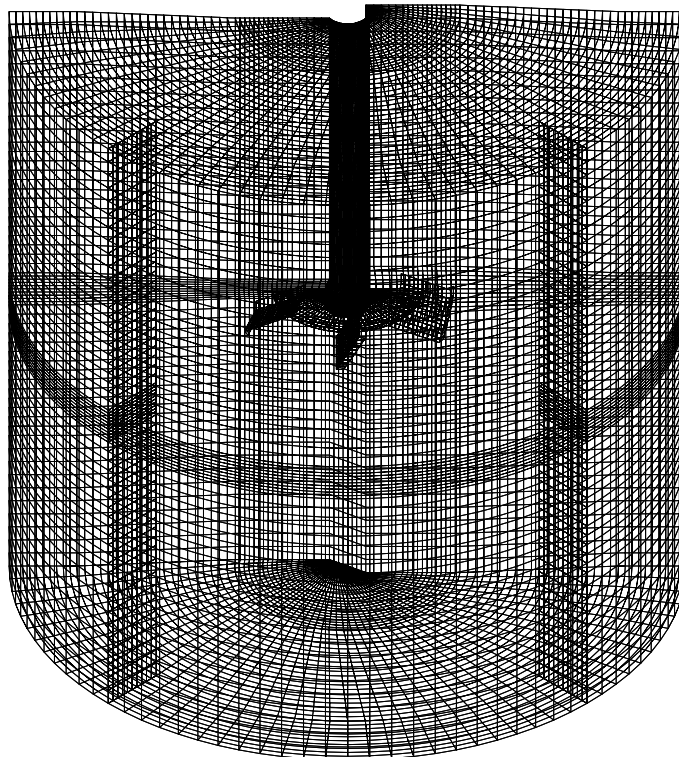
(b)

Figure 4.3 (a) Calculation domain of straight-blade turbine

(b) Grids of straight-blade turbine



(a)



(b)

Figure 4.4 (a) Calculation domain of pitched-blade turbine

(b) Grids of pitched-blade turbine V_r/V_{tip}

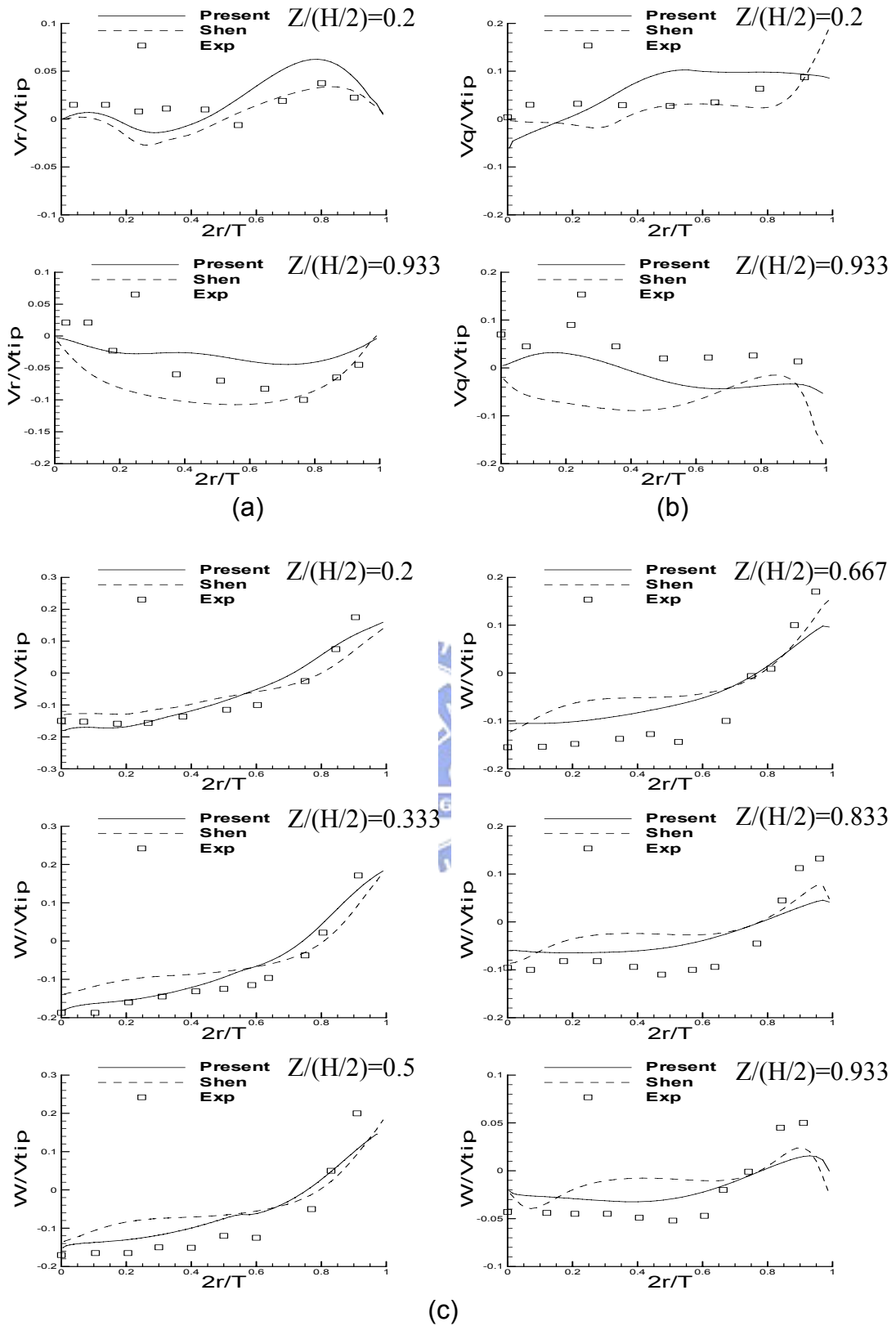


Figure 4.5 Radial profiles of (a) radial, (b) tangential, and (c) axial velocity compare prediction of Shen [19] and experimental data of Ranade[3]. ($D=T/3$, $C=T/2$, $\alpha=90$)

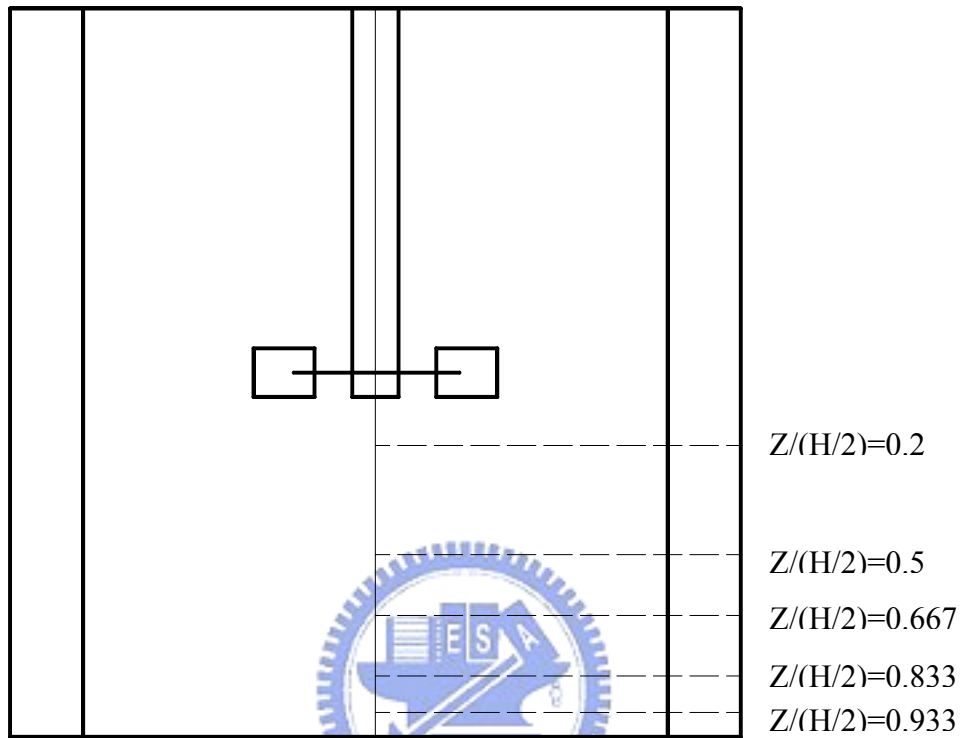


Figure 4.6 The position of various Z/R

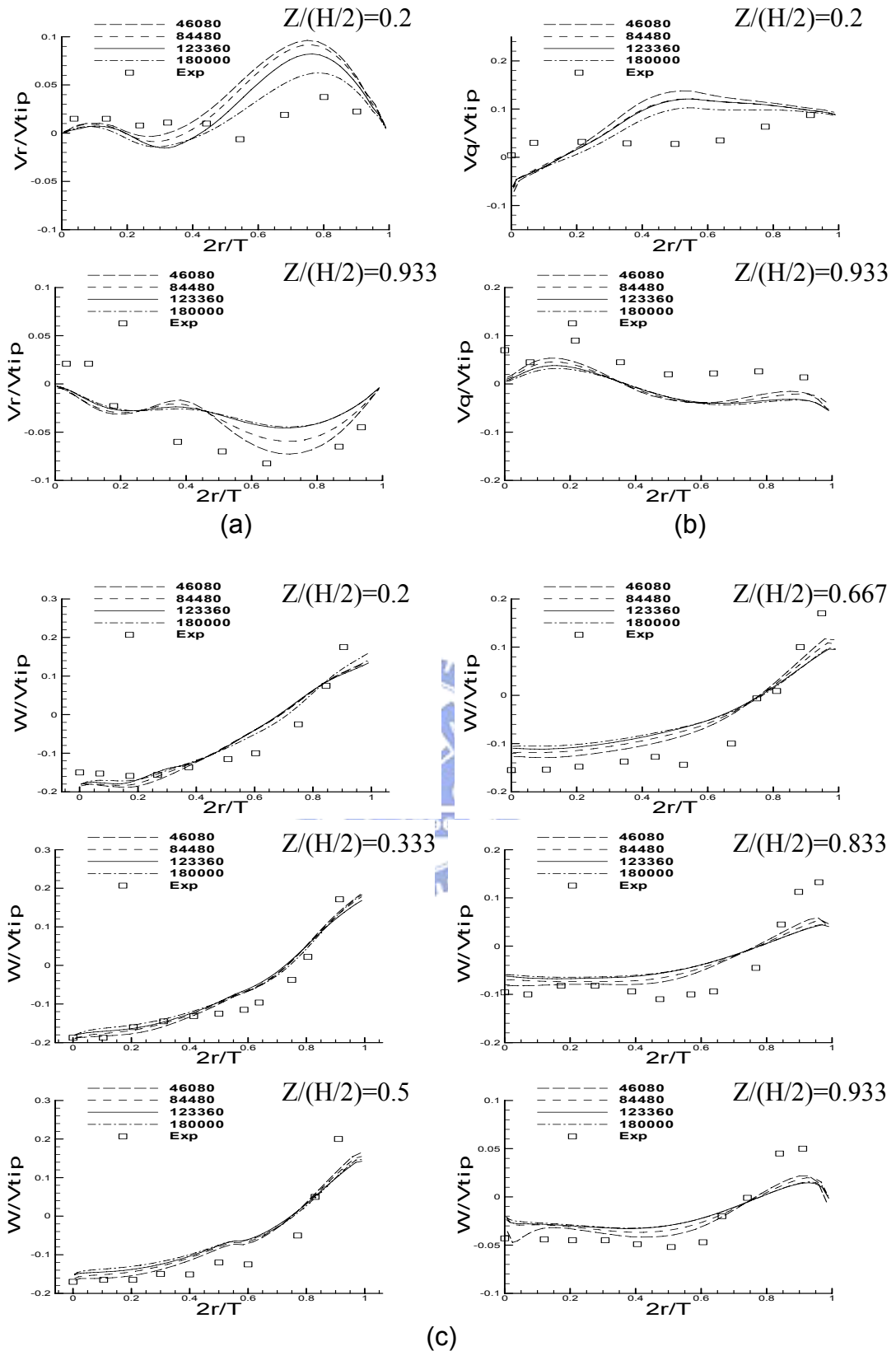


Figure 4.7 Radial profiles of (a) radial, (b) tangential, and (c) axial velocity of four kinds of grids. ($D=T/3$, $C=T/2$, $\alpha=90$)

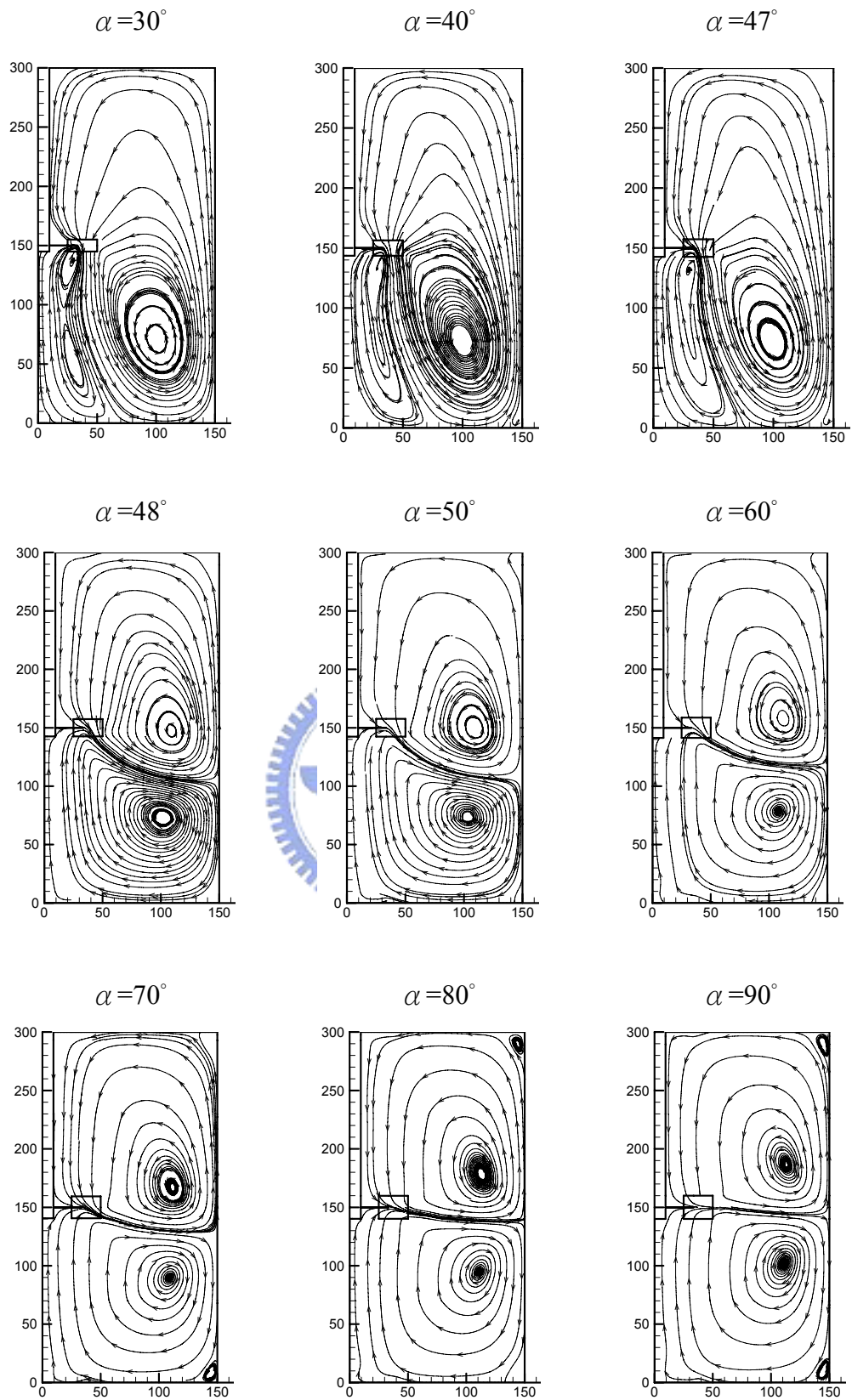


Figure 4.8 Stream lines of various blade angles at the vertical plane of $\varphi = -30^\circ$ ($D=T/3$
 $d=2D/3$ $C=T/2$)

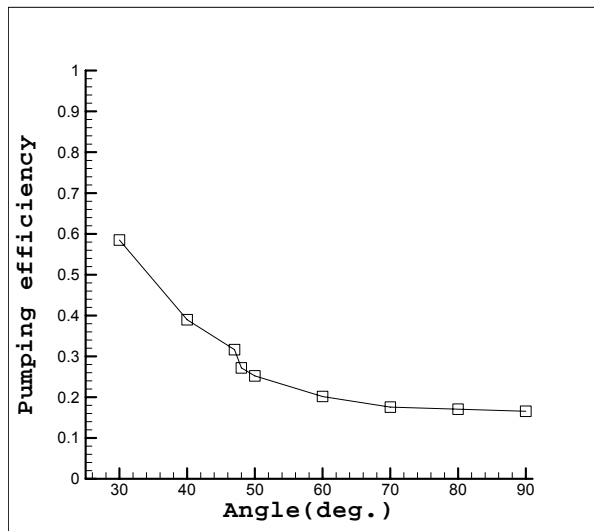
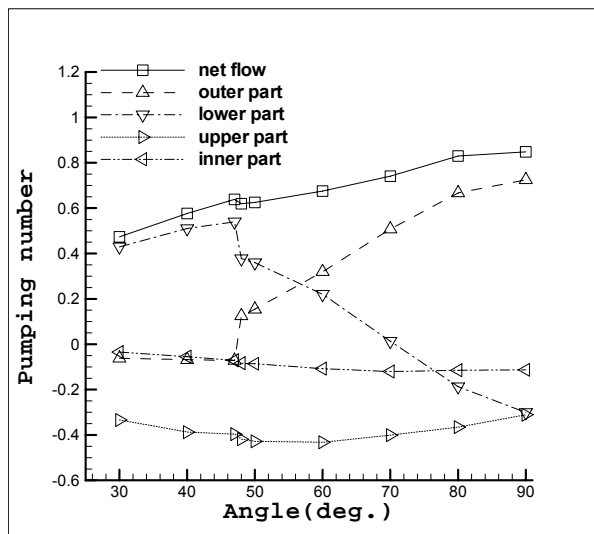
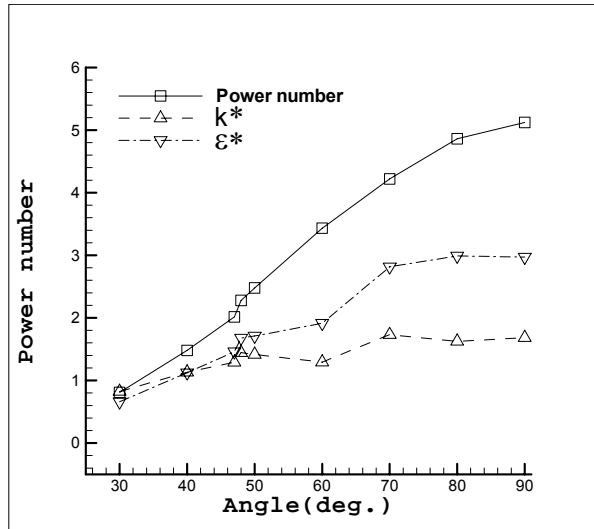


Figure 4.9 The Power number, Pumping number, and Pumping efficiency of various blade angles. ($D=T/3$ $d=2D/3$ $C=T/2$)

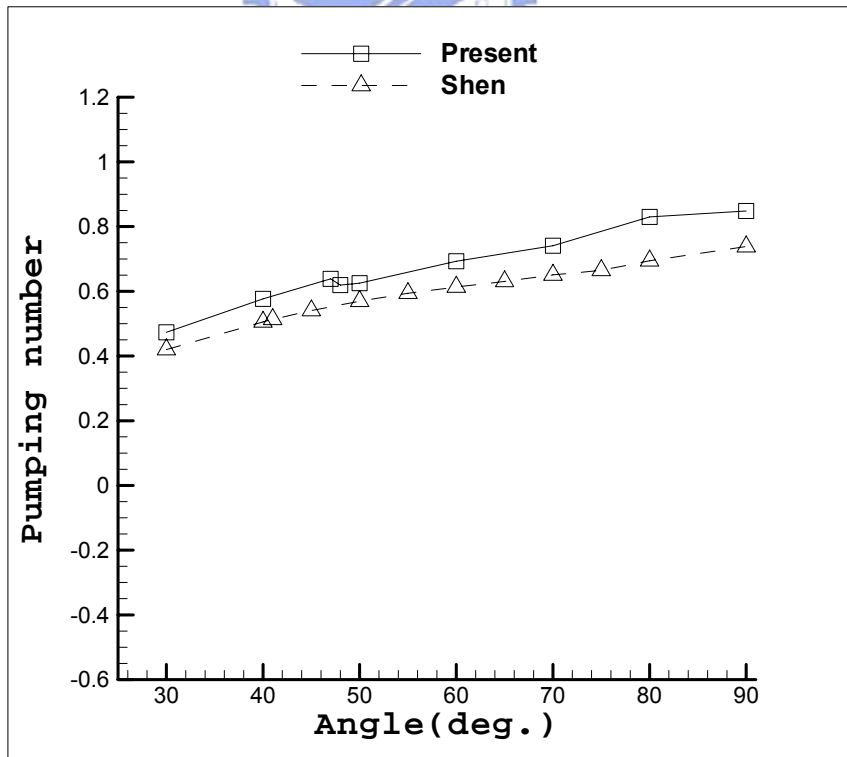
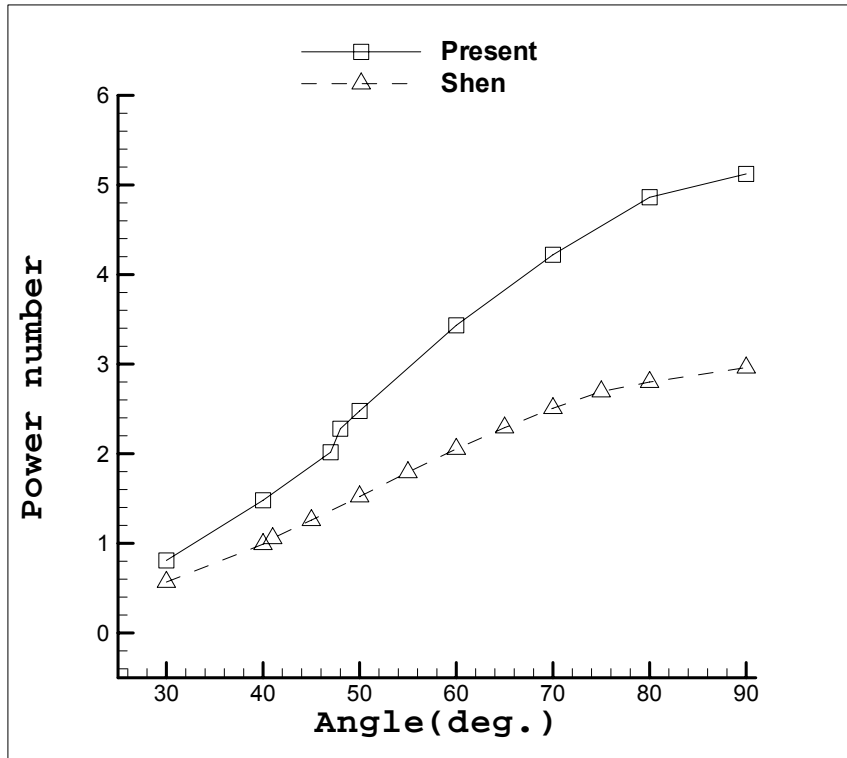


Figure 4.10 The angular profiles of Power number and Pumping number compare with Shen's work. ($D=T/3$ $d=2D/3$ $C=T/2$)

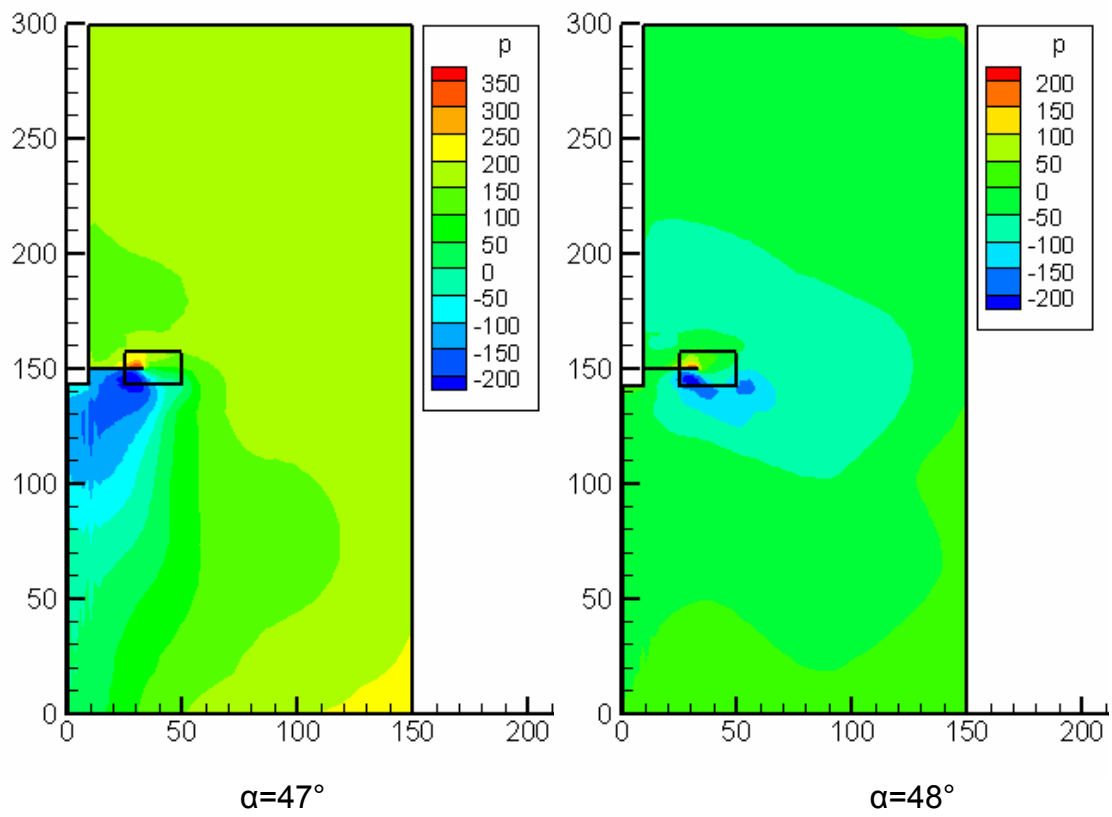


Figure 4.11 The pressure contour of $\alpha=47^\circ$ and $\alpha=48^\circ$ at the vertical plane of $\Phi=-30^\circ$.
 ($D=T/3$ $d=2D/3$ $C=T/2$)

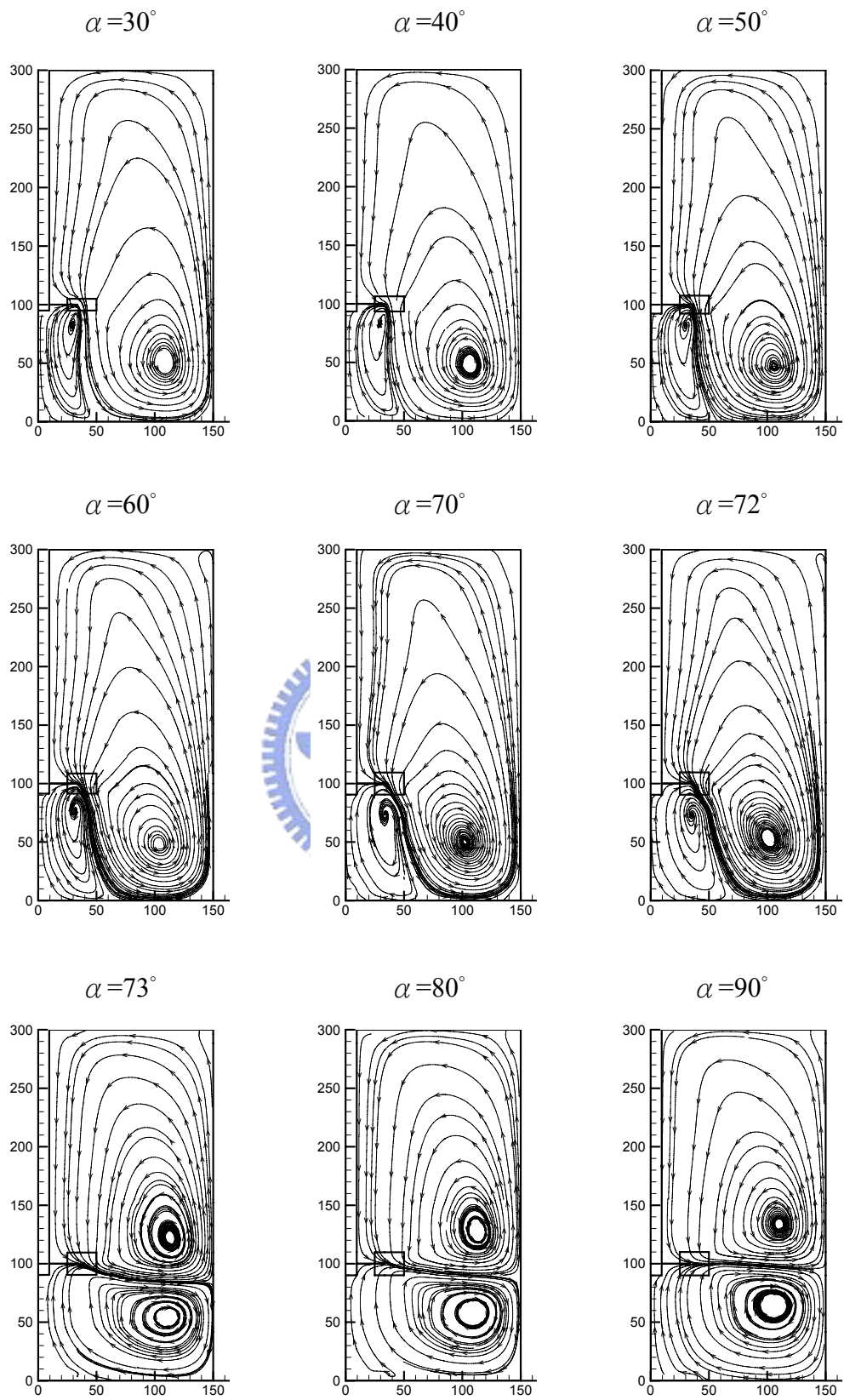


Figure 4.12 Stream lines of various blade angles at the vertical plane of $\varphi = -30^\circ$.
 ($D=T/3$ $d=2D/3$ $C=T/3$)

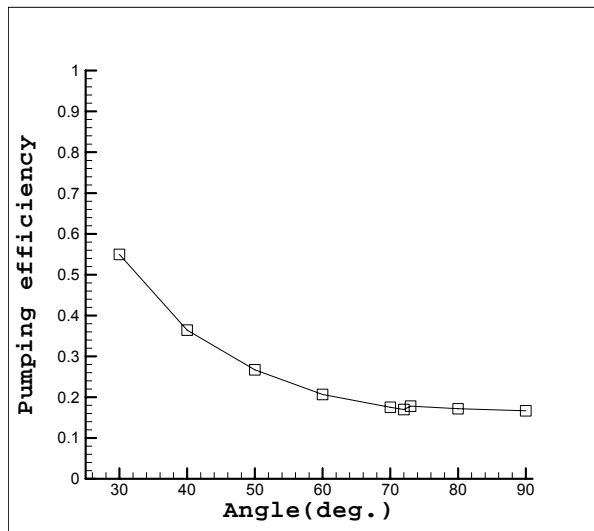
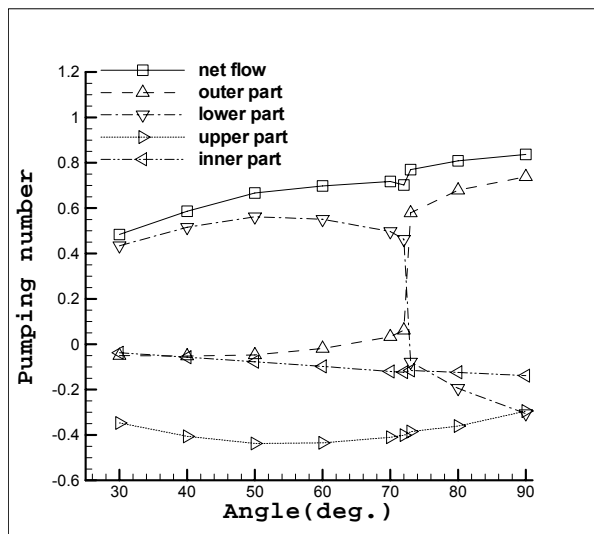
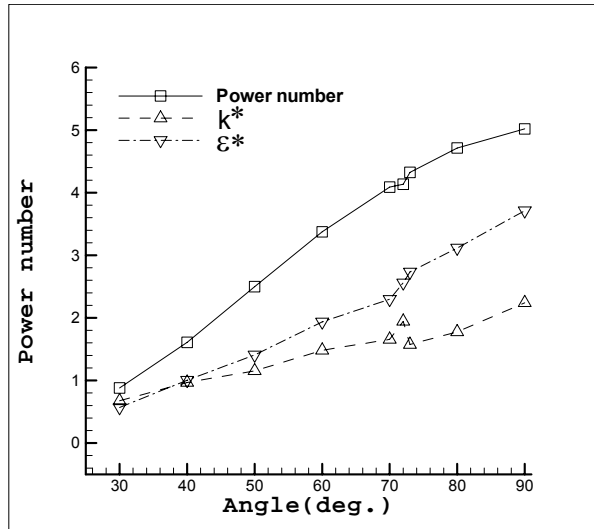


Figure 4.13 The Power number, Pumping number, and pumping efficiency of various blade angles. ($D=T/3$ $d=2D/3$ $C=T/3$)

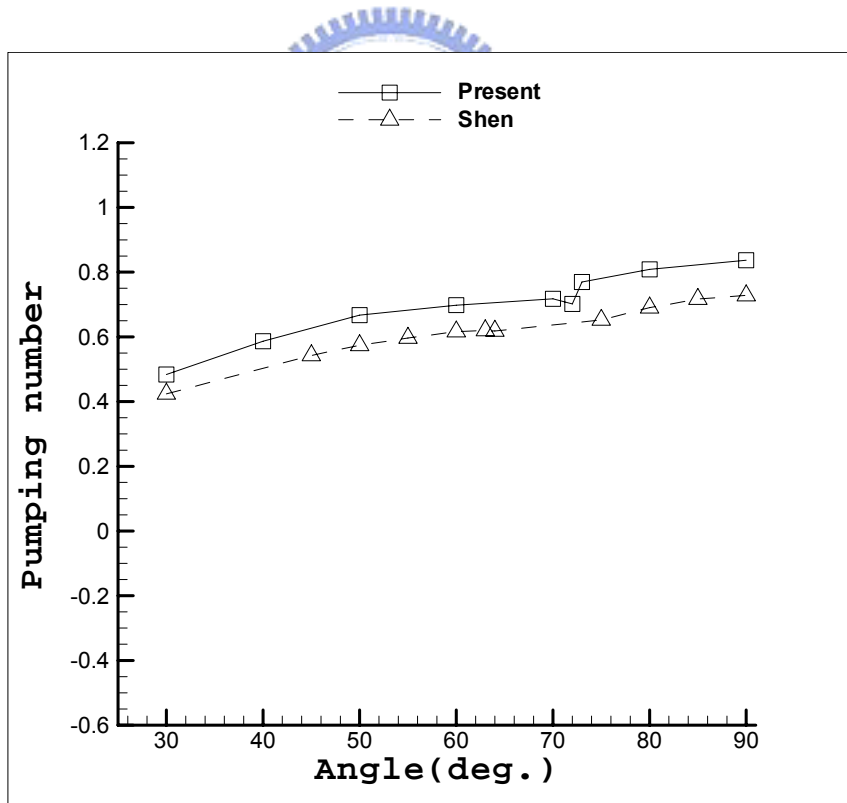
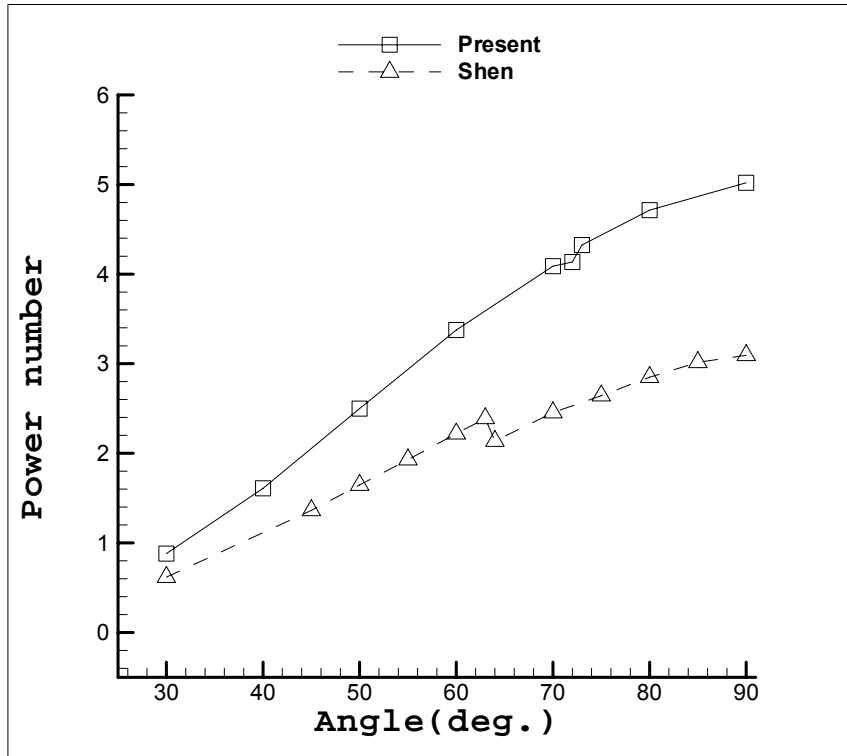


Figure 4.14 The angular profile of Power number and Pumping number compare with Shen's work. ($D=T/3$ $d=2D/3$ $C=T/3$)

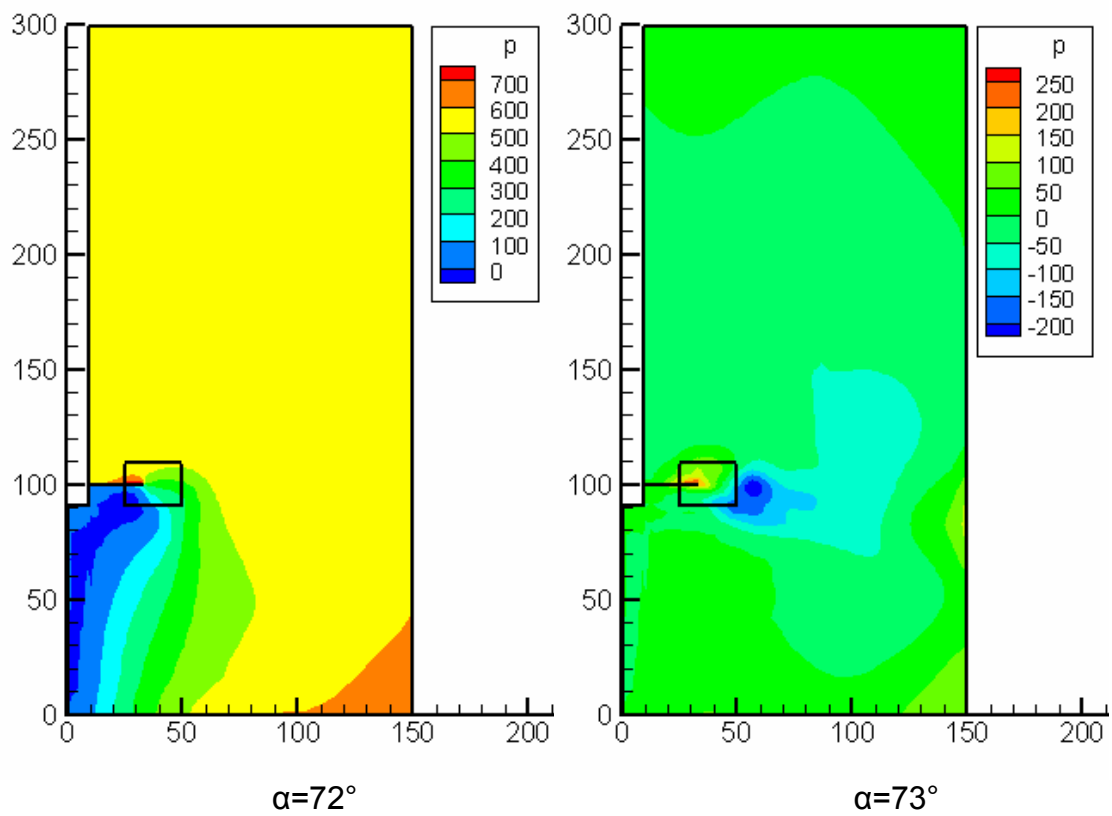


Figure 4.15 The pressure contour of $\alpha=72^\circ$ and $\alpha=73^\circ$ at the vertical plane of $\Phi=-30^\circ$.
 (D=T/3 d=2D/3 C=T/3)

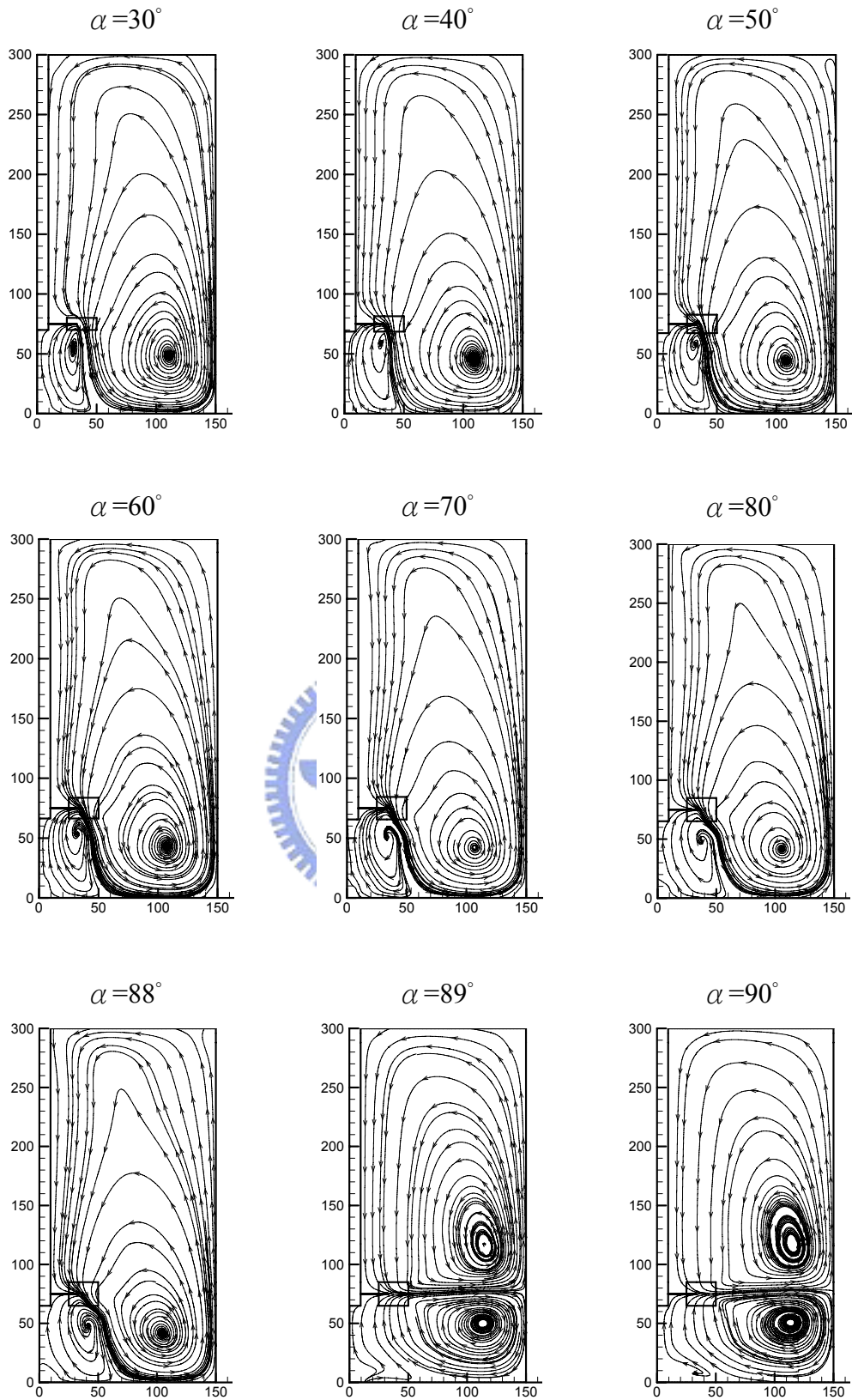


Figure 4.16 Stream lines of various blade angles at the vertical plane of $\varphi = -30^\circ$.
 ($D=T/3$ $d=2D/3$ $C=T/4$)

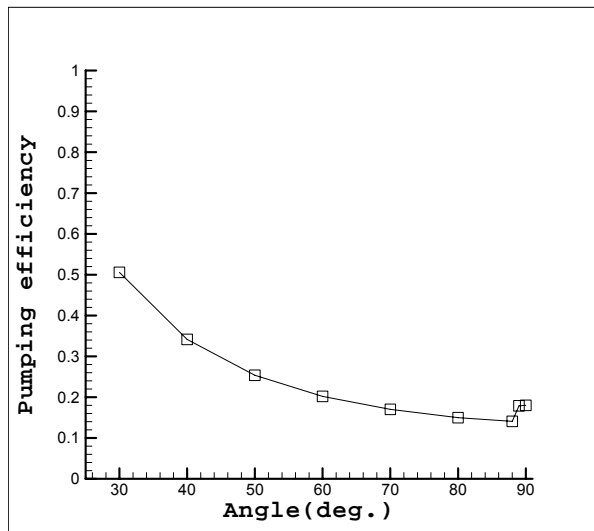
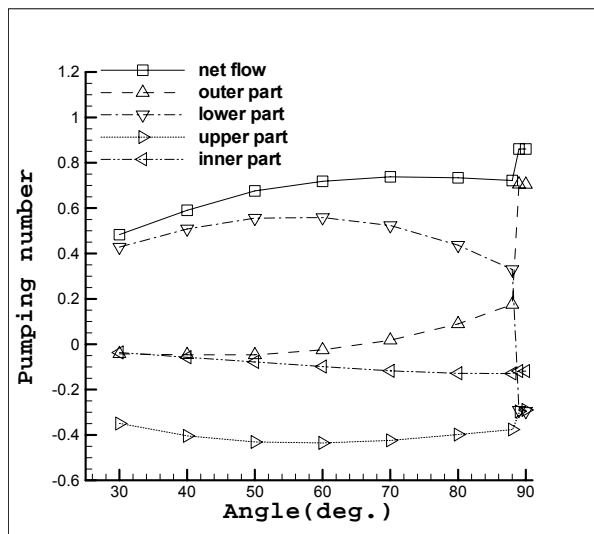
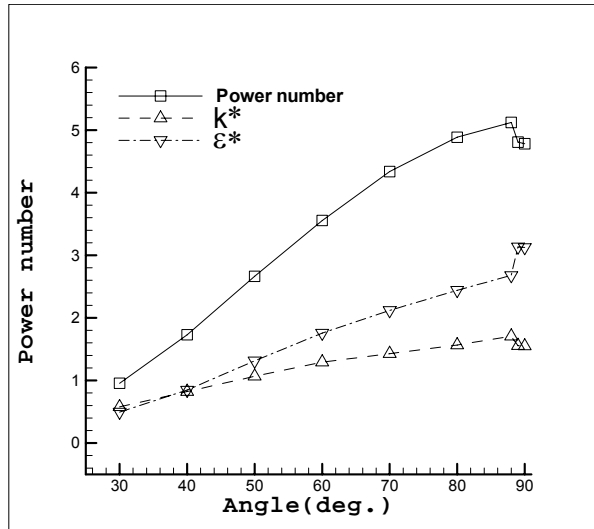


Figure 4.17 The Power number, Pumping number, and Pumping efficiency of various blade angles. ($D=T/3$ $d=2D/3$ $C=T/4$)

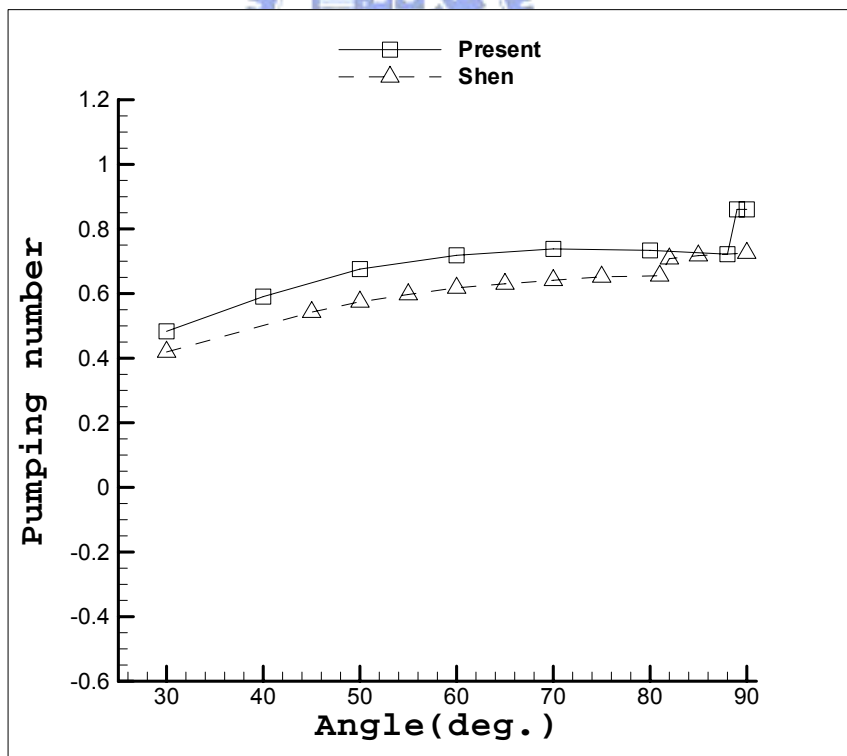
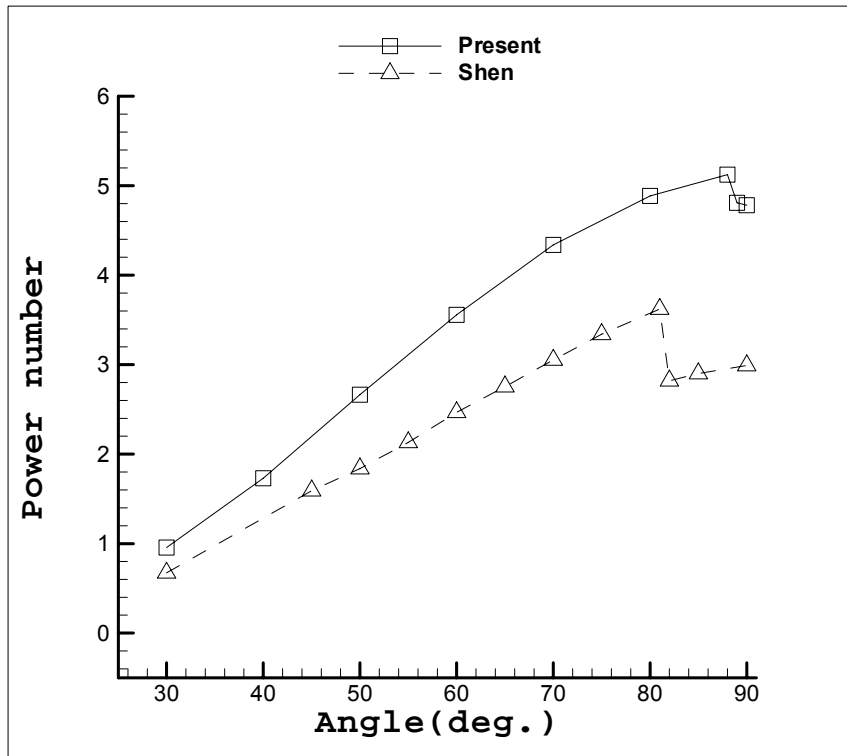


Figure 4.18 The angular profile of Power number and Pumping number compare with Shen's work. ($D=T/3$ $d=2D/3$ $C=T/4$)

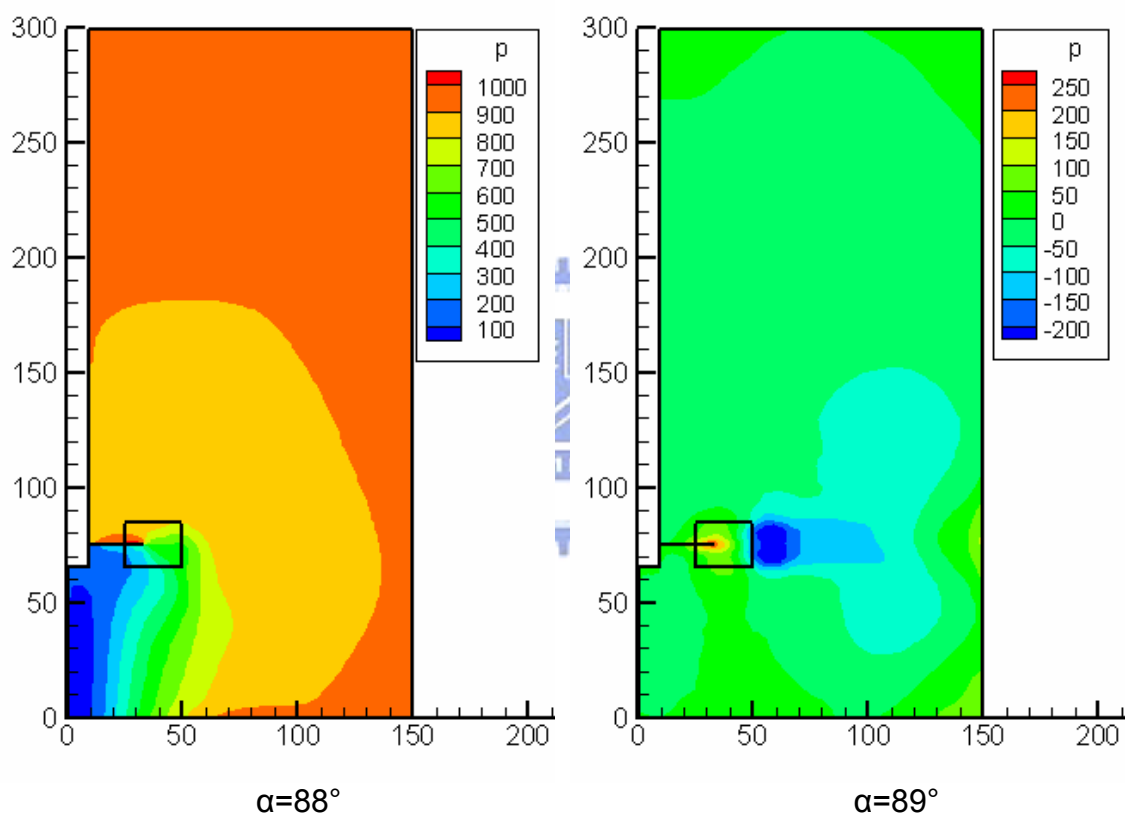


Figure 4.19 The pressure contour of $\alpha=88^\circ$ and $\alpha=89^\circ$ at the vertical plane of $\Phi=-30^\circ$.
 ($D=T/3$ $d=2D/3$ $C=T/4$)

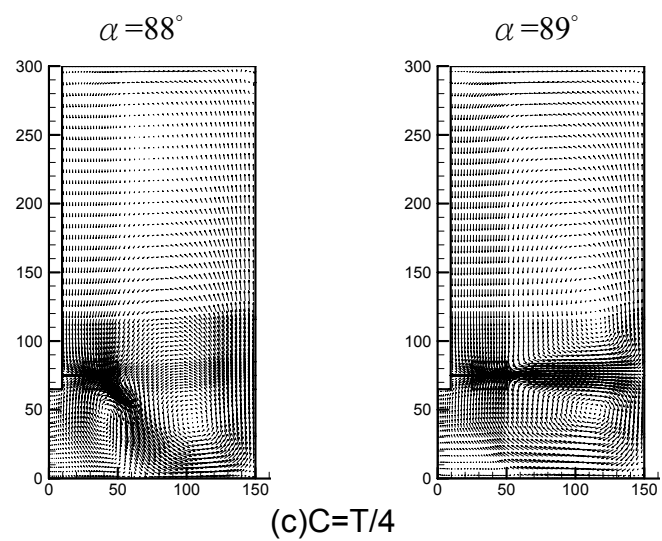
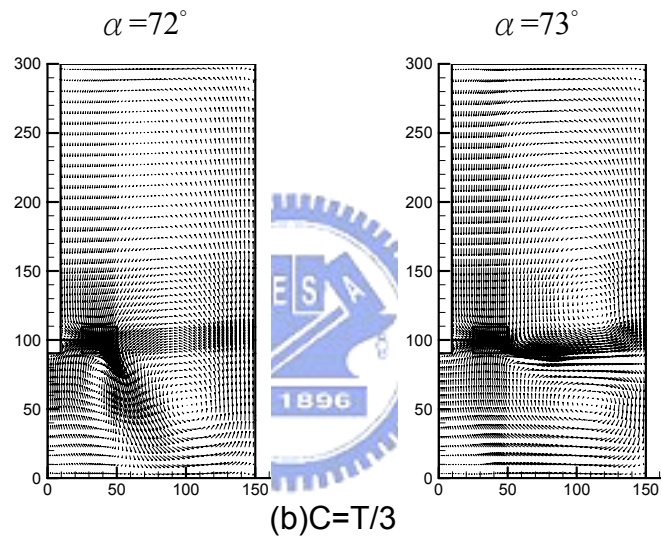
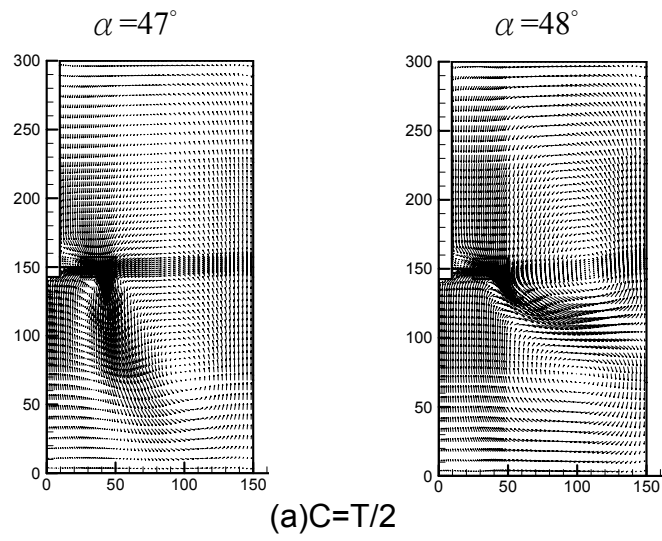


Figure 4.20 The flow field changes from axial flow to radial flow of different impeller location.

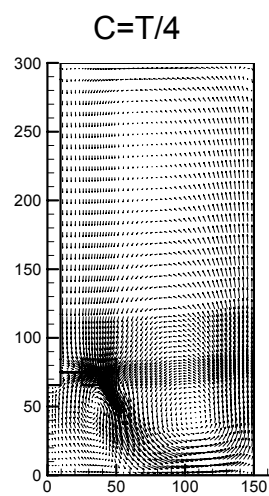
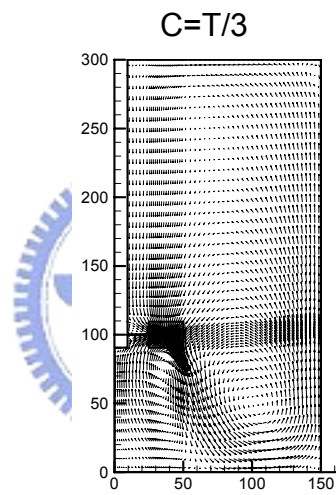
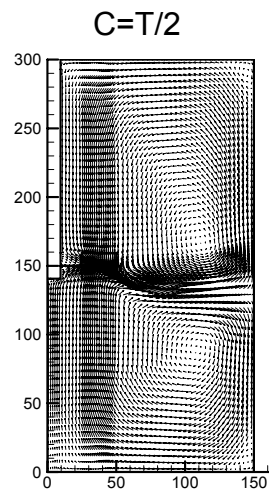


Figure 4.21 The flow field of blade angle $\alpha=60^\circ$ when the impeller is posited at three different location

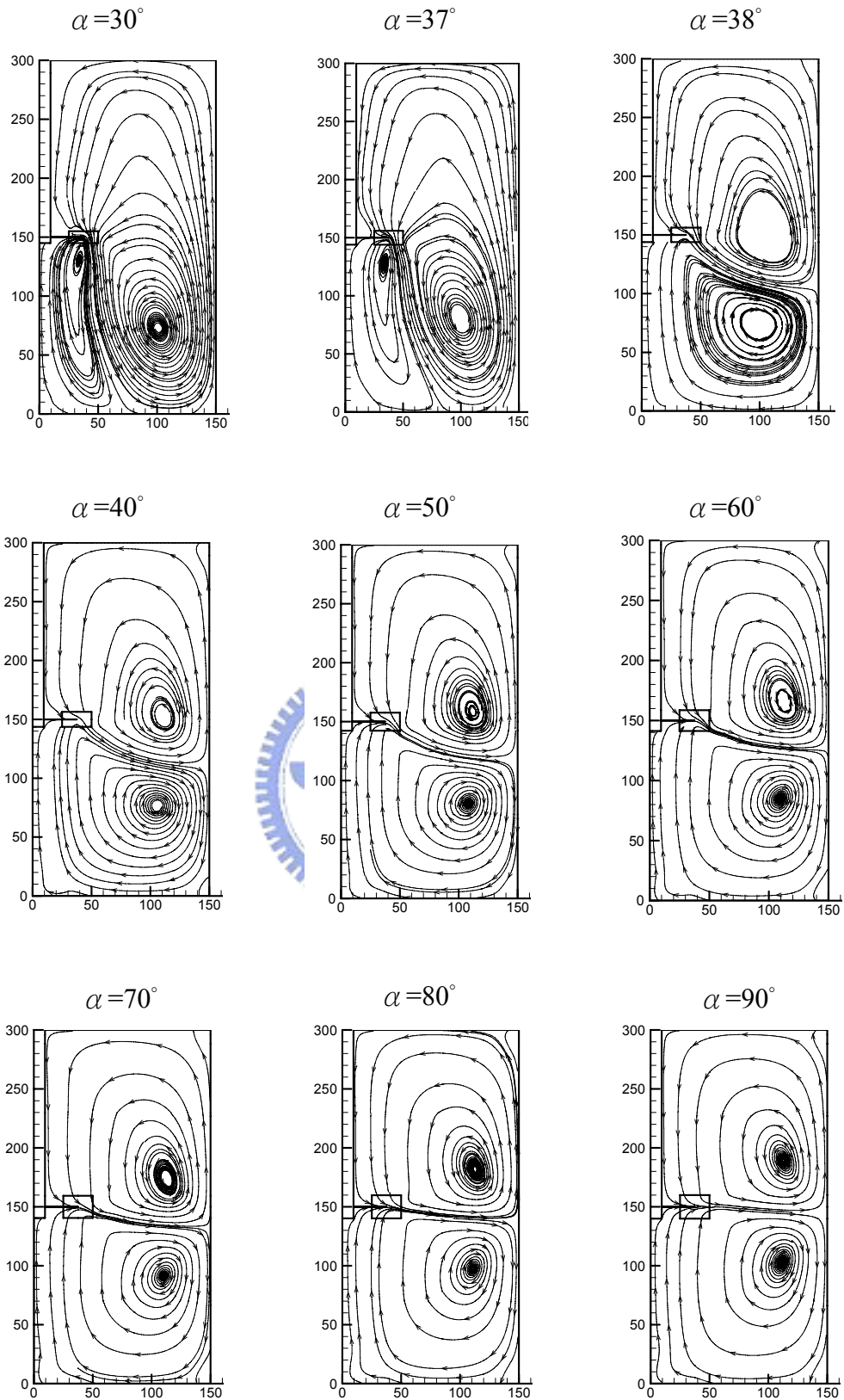


Figure 4.22 Stream lines of various blade angles at the vertical plane of $\Phi = -30$.
 ($D=T/3$ $d=3D/4$ $C=T/2$)

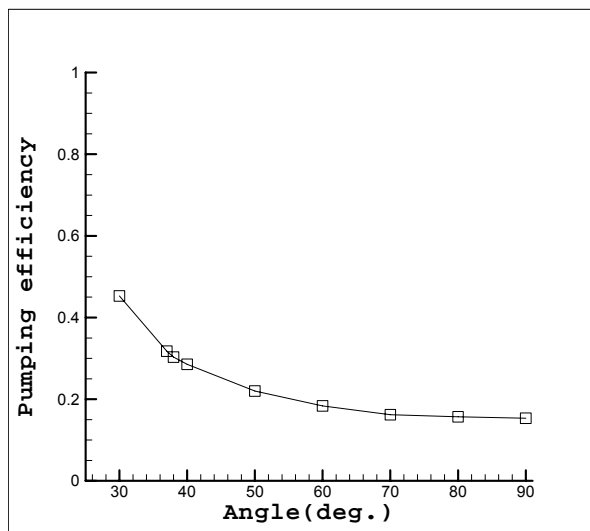
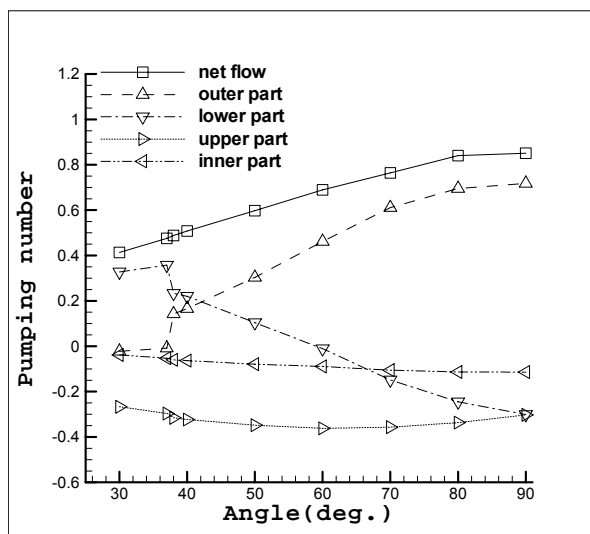
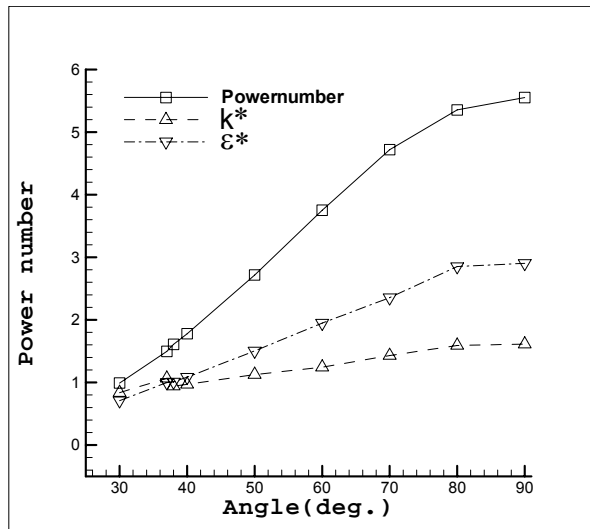


Figure 4.23 The Power number, Pumping number, and Pumping efficiency of various blade angles. ($D=T/3$ $d=3D/4$ $C=T/2$)

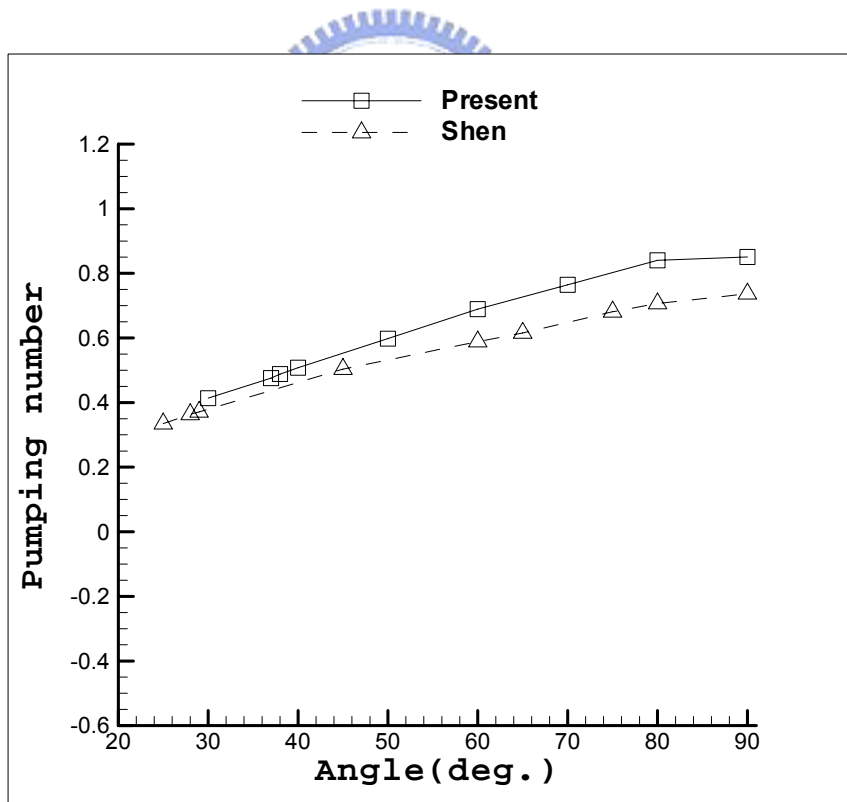
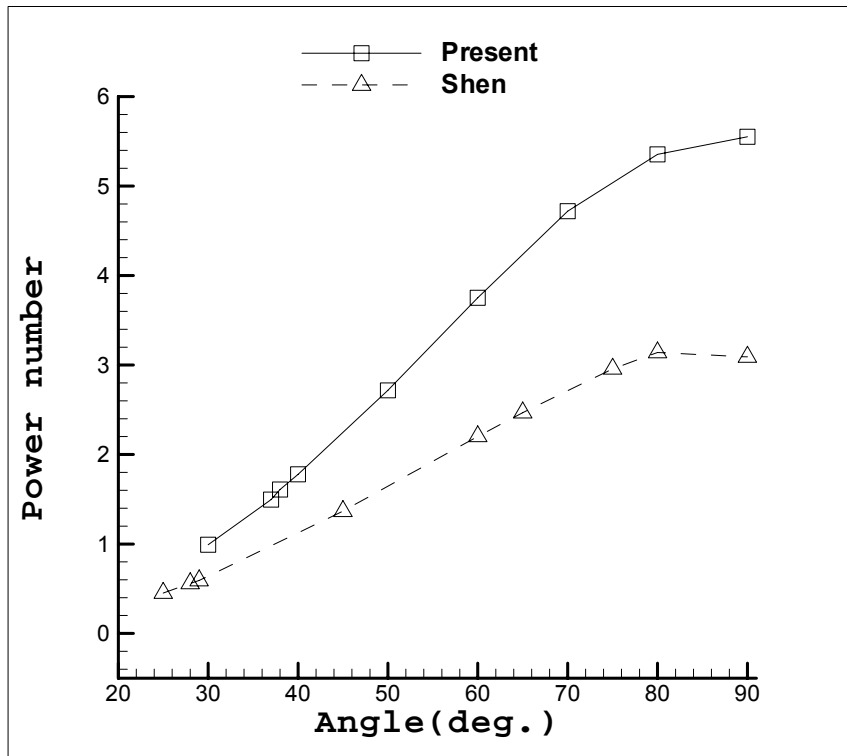


Figure 4.24 The angular profile of Power number and Pumping number compare with Shen's work. ($D=T/3$ $d=3D/4$ $C=T/2$)

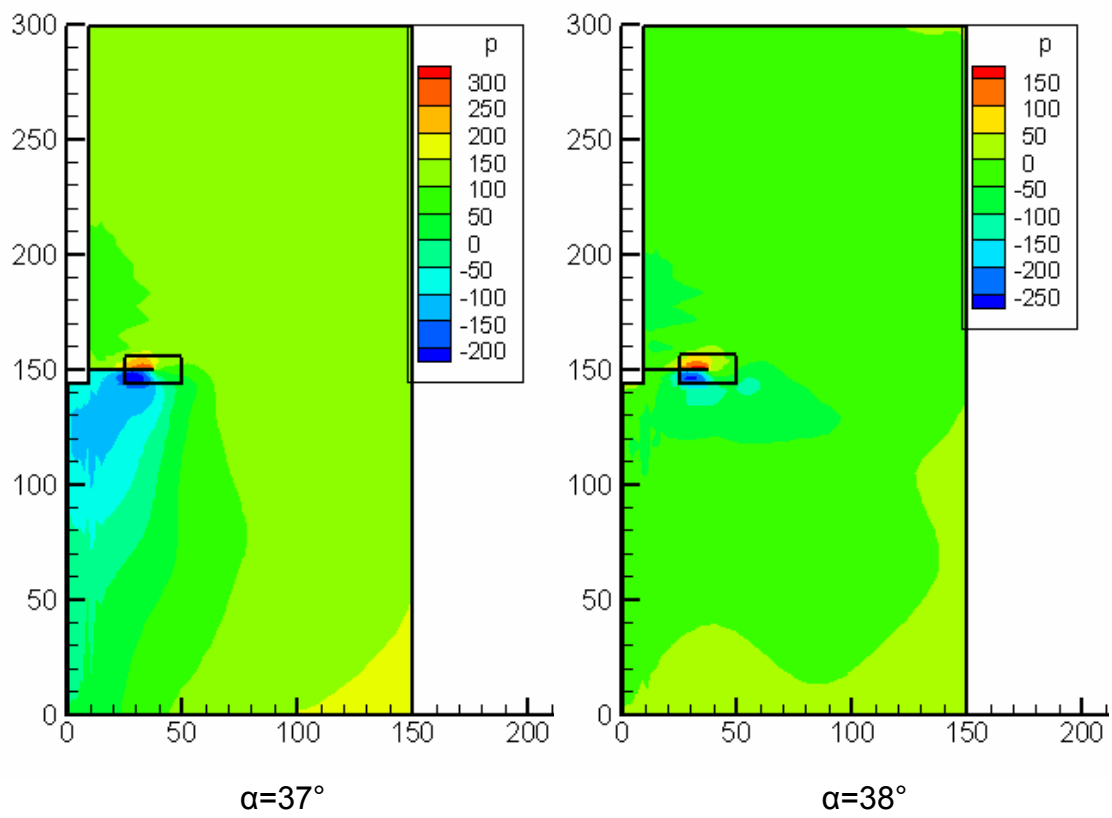


Figure 4.25 The pressure contour of $\alpha= 37^\circ$ and $\alpha= 38^\circ$ at the vertical plane of $\Phi=-30^\circ$.
 (D=T/3 d=3D/4 C=T/2)

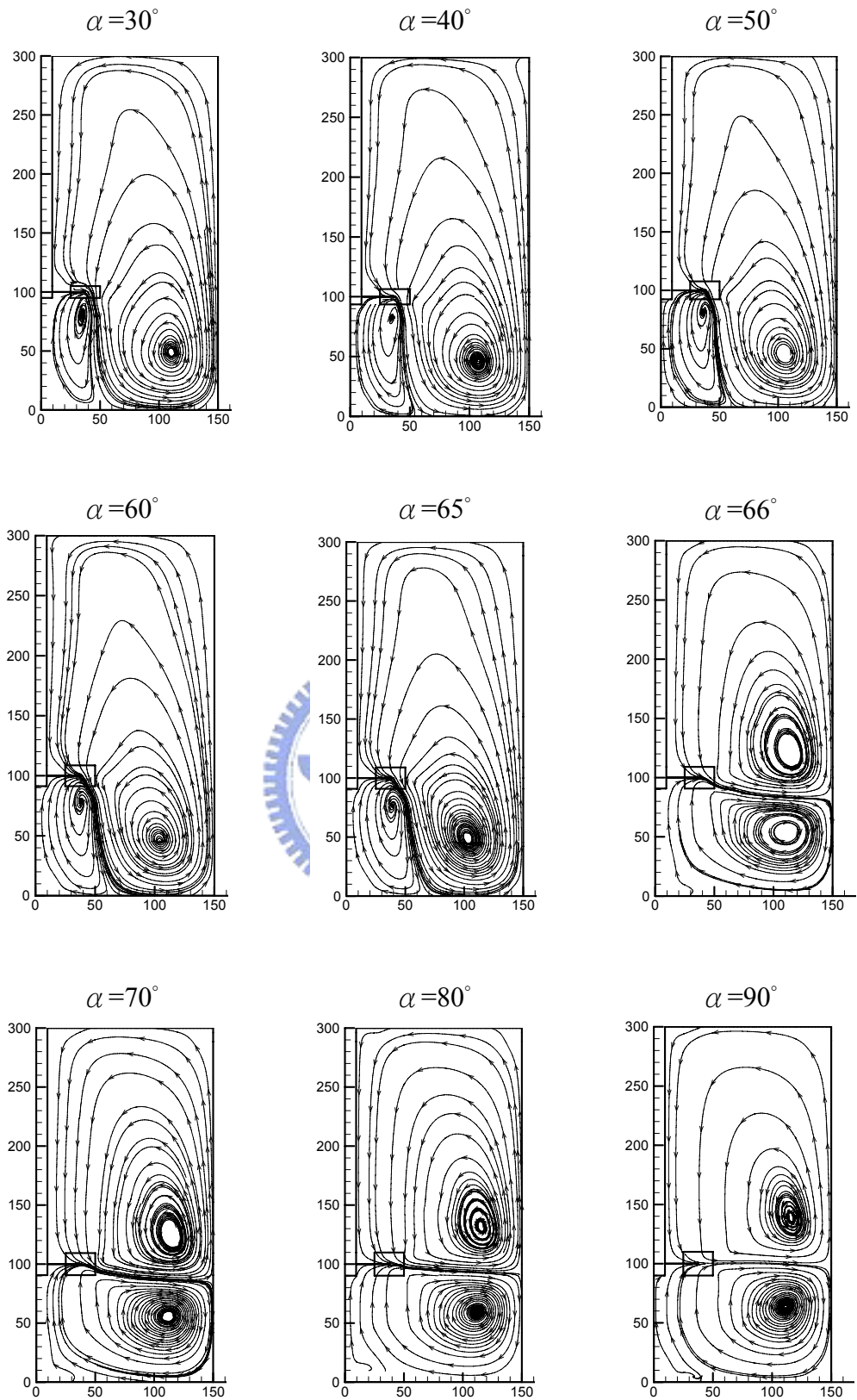


Figure 4.26 Stream lines of various blade angles at the vertical plane of $\Phi = -30$.
 ($D=T/3$ $d=3D/4$ $C=T/3$)

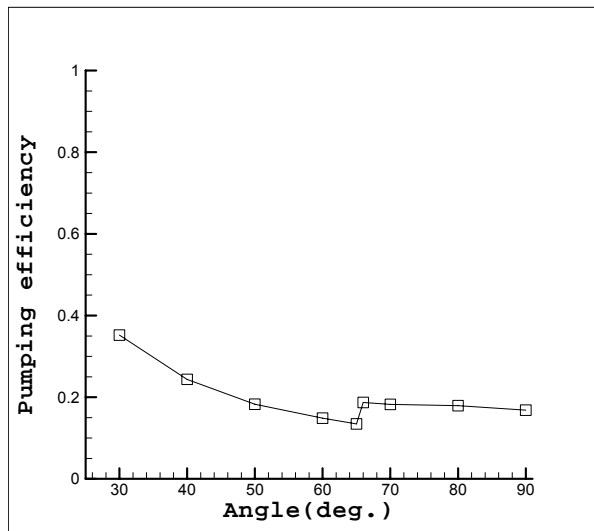
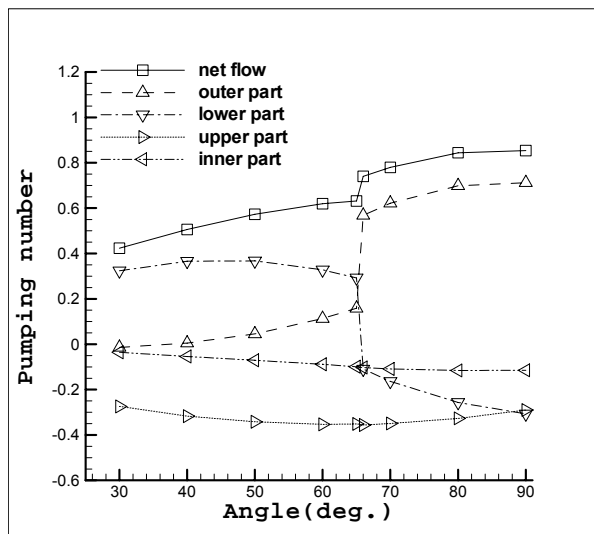
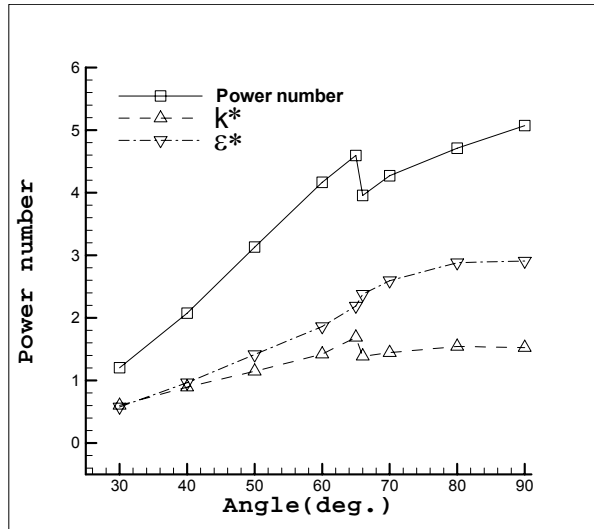


Figure 4.27 The Power number, Pumping number, and Pumping efficiency of various blade angles. ($D=T/3$ $d=3D/4$ $C=T/3$)

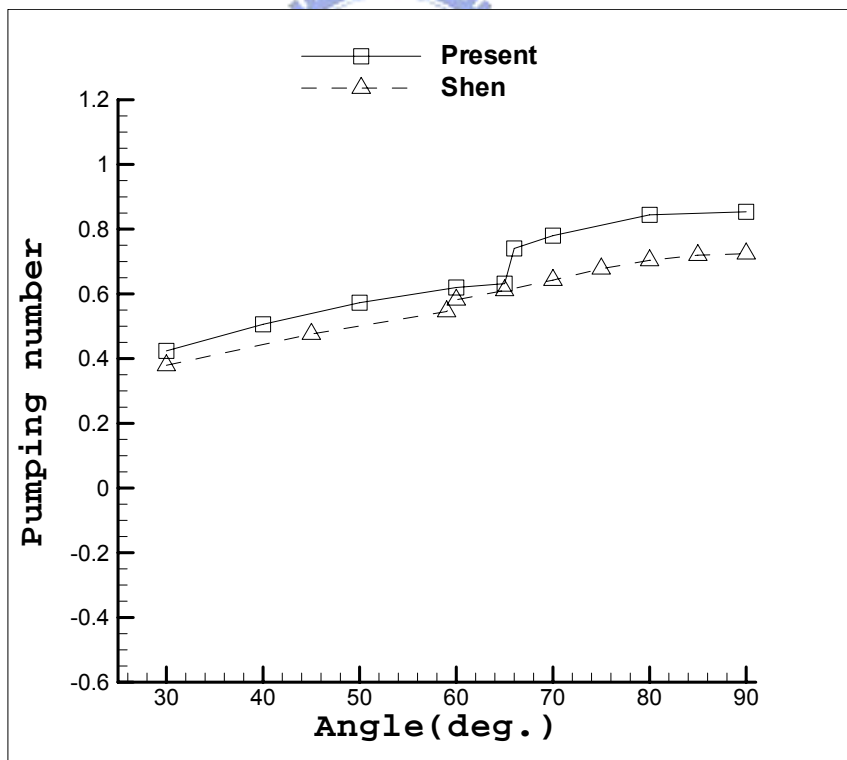
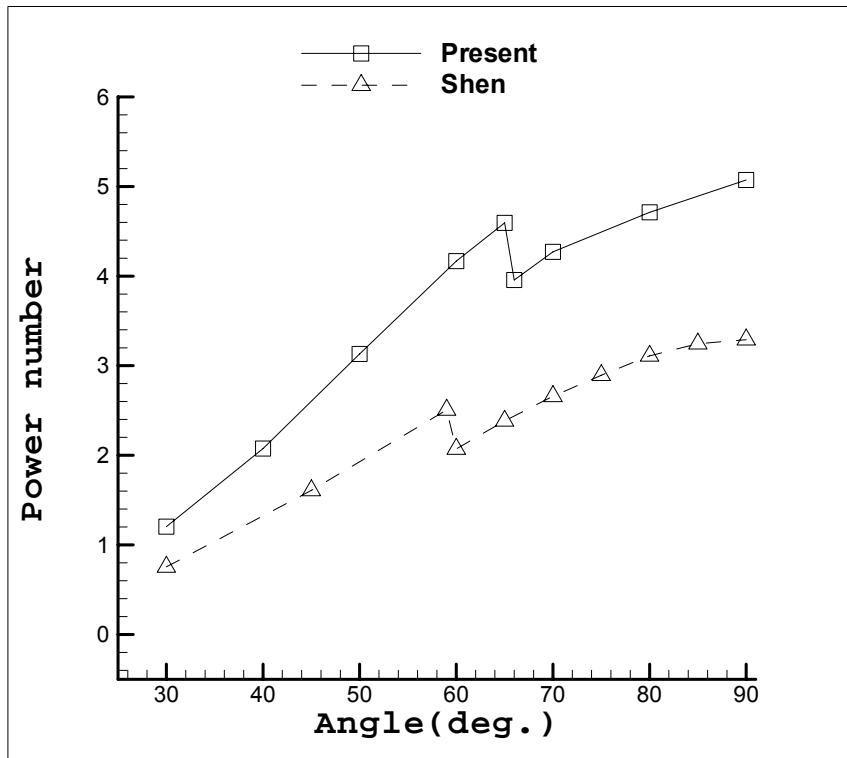


Figure 4.28 The angular profile of Power number and Pumping number compare with Shen's work. ($D=T/3$ $d=3D/4$ $C=T/3$)

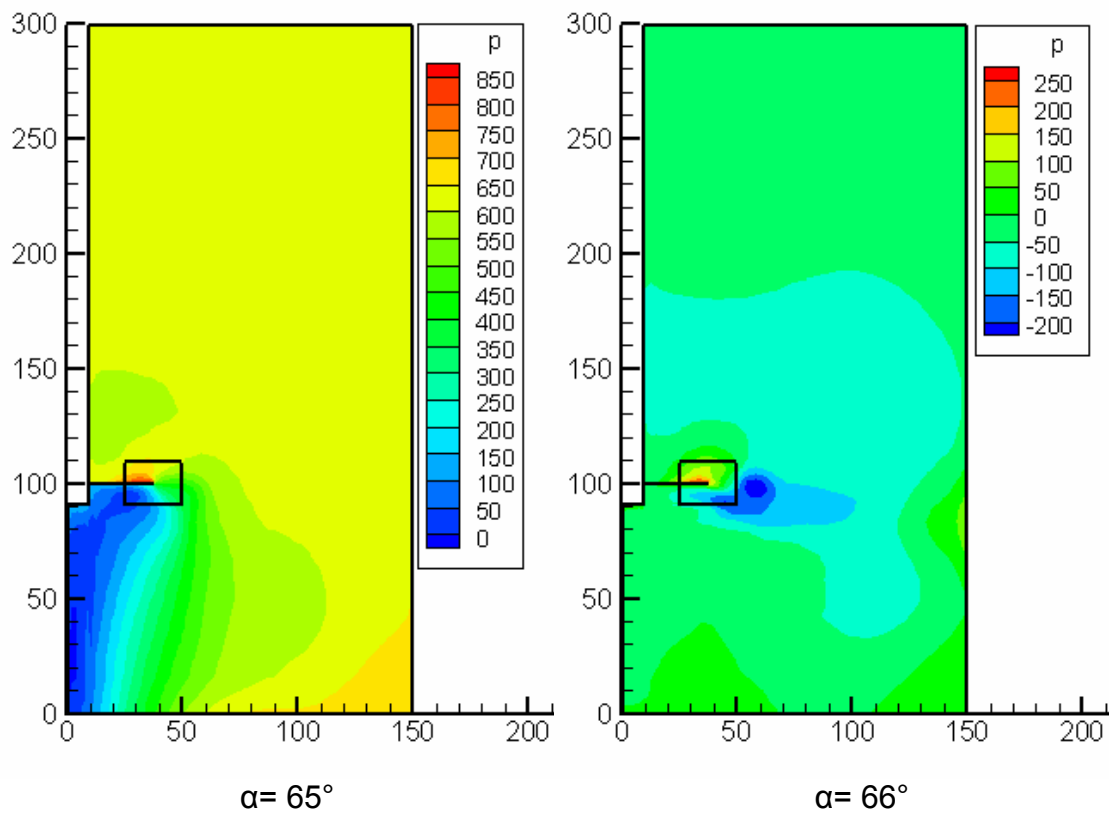


Figure 4.29 The pressure contour of $\alpha = 65^\circ$ and $\alpha = 66^\circ$ at the vertical plane of $\Phi = -30^\circ$.
 (D=T/3 d=3D/4 C=T/3)

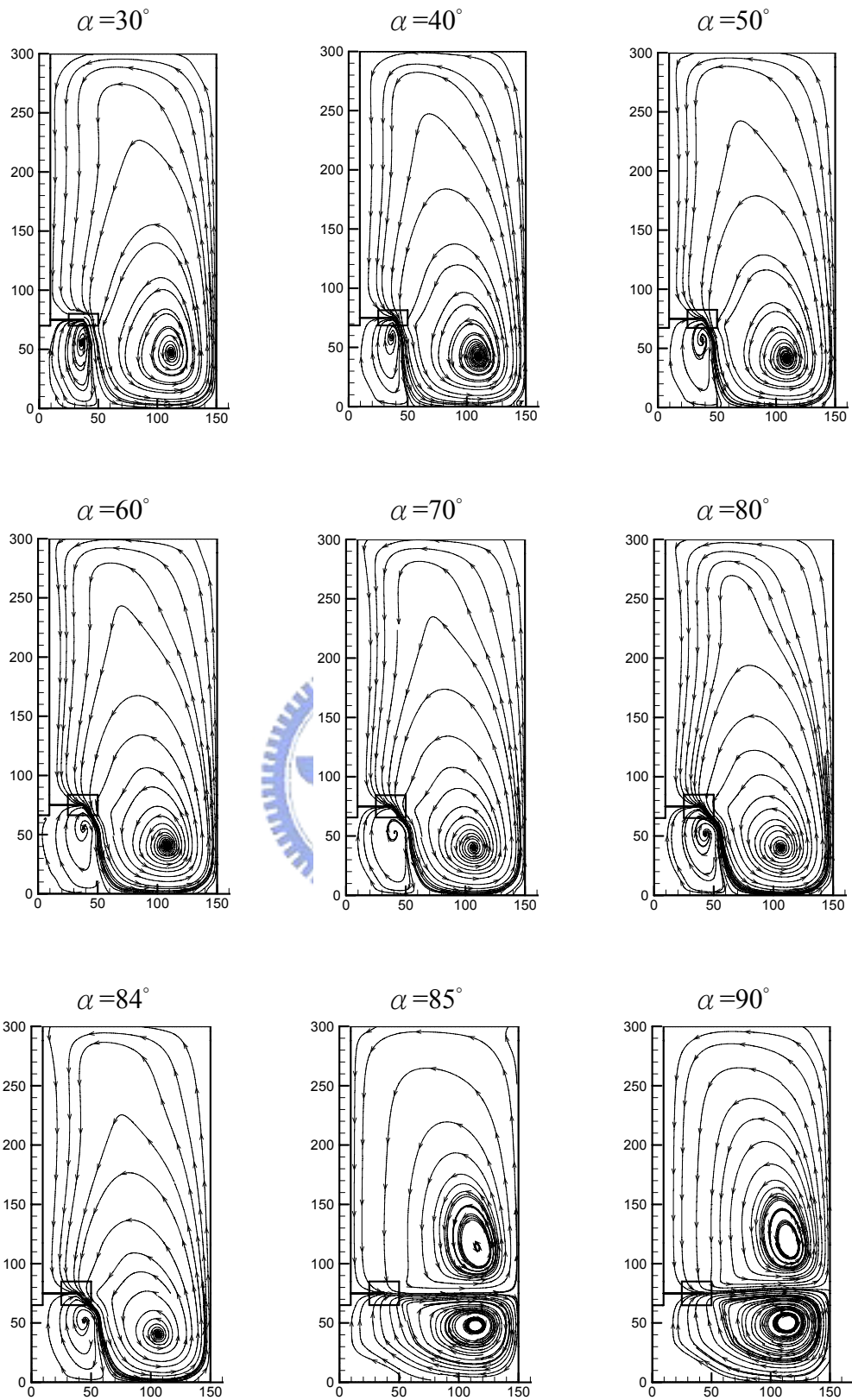


Figure 4.30 Stream lines of various blade angles at the vertical plane of $\varphi = -30^\circ$.
 ($D=T/3$ $d=3D/4$ $C=T/4$)

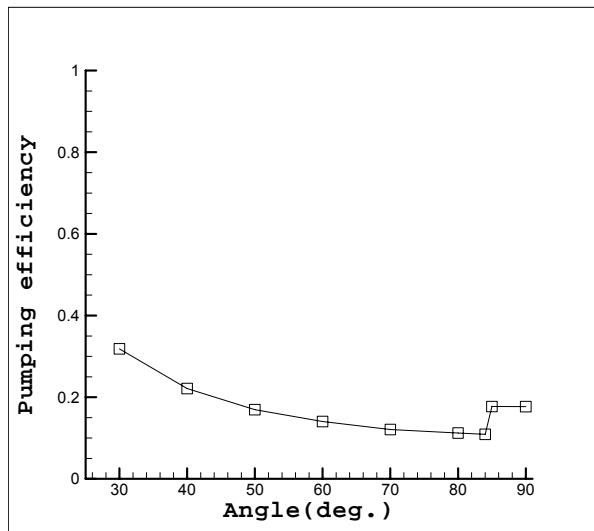
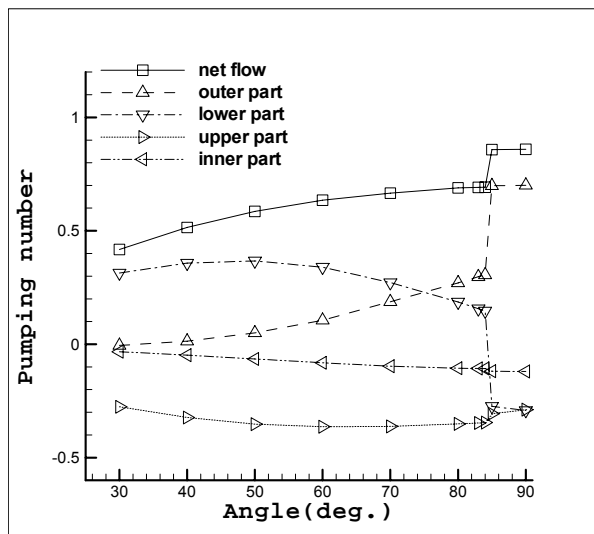
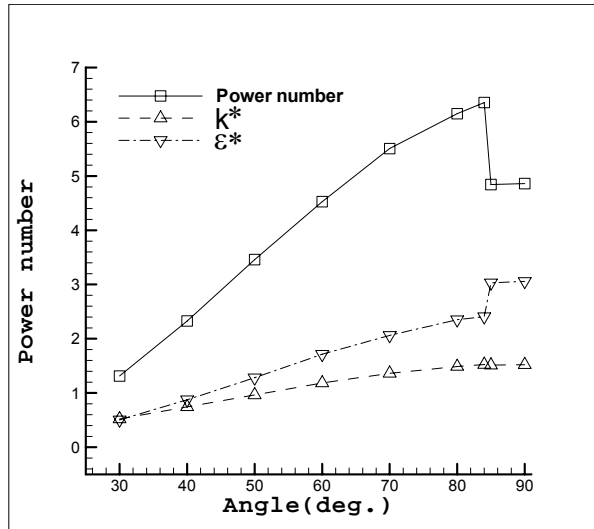


Figure 4.31 The Power number, Pumping number, and Pumping efficiency of various blade angles. ($D=T/3$ $d=3D/4$ $C=T/4$)

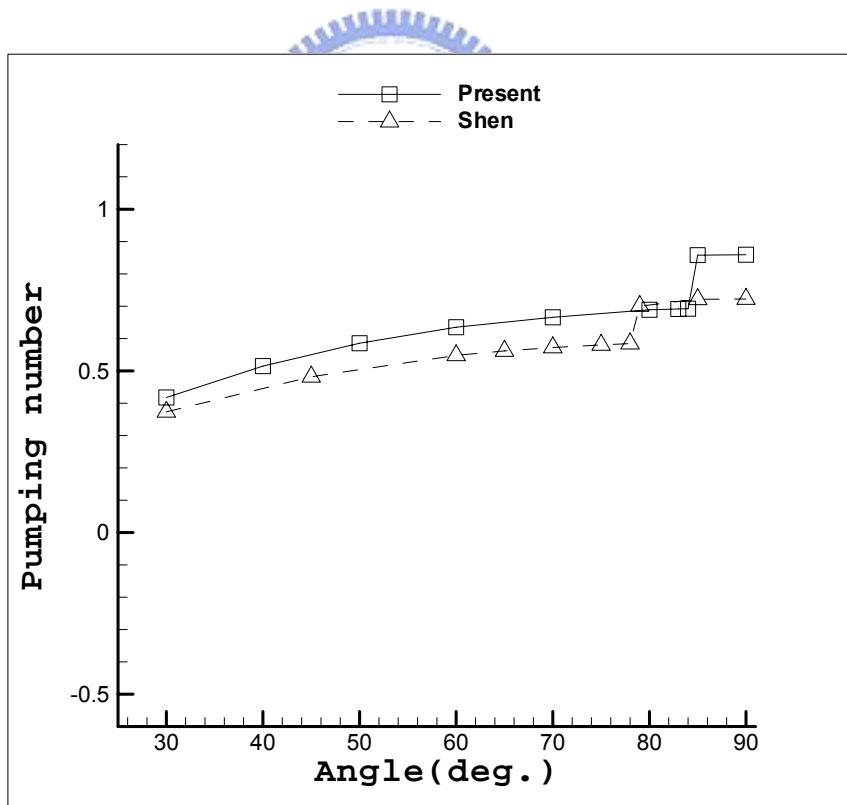
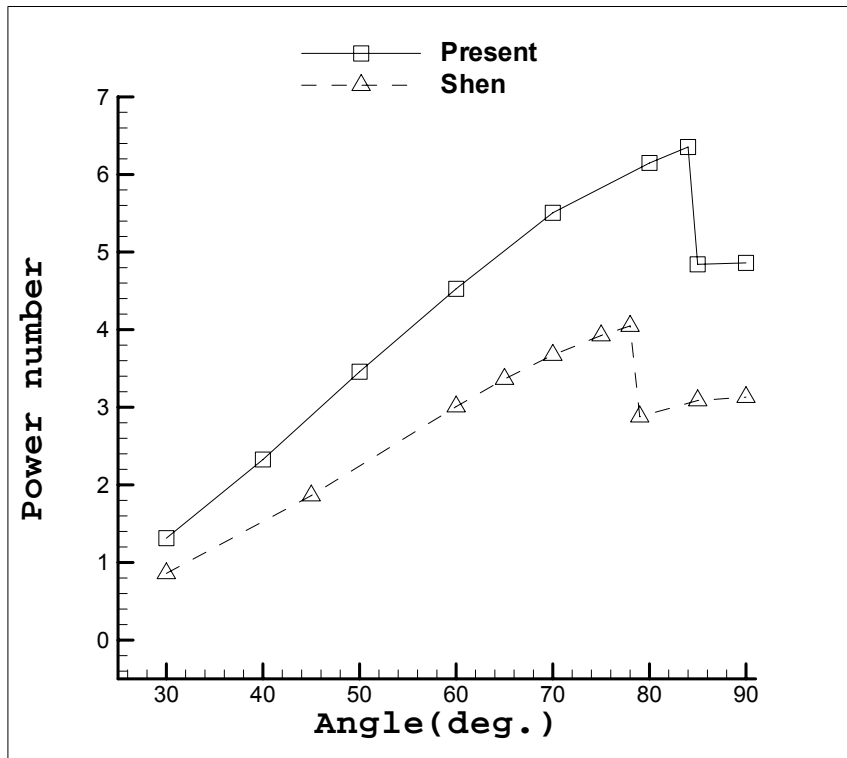


Figure 4.32 The angular profile of Power number and Pumping number compare with Shen's work. ($D=T/3$ $d=3D/4$ $C=T/4$)

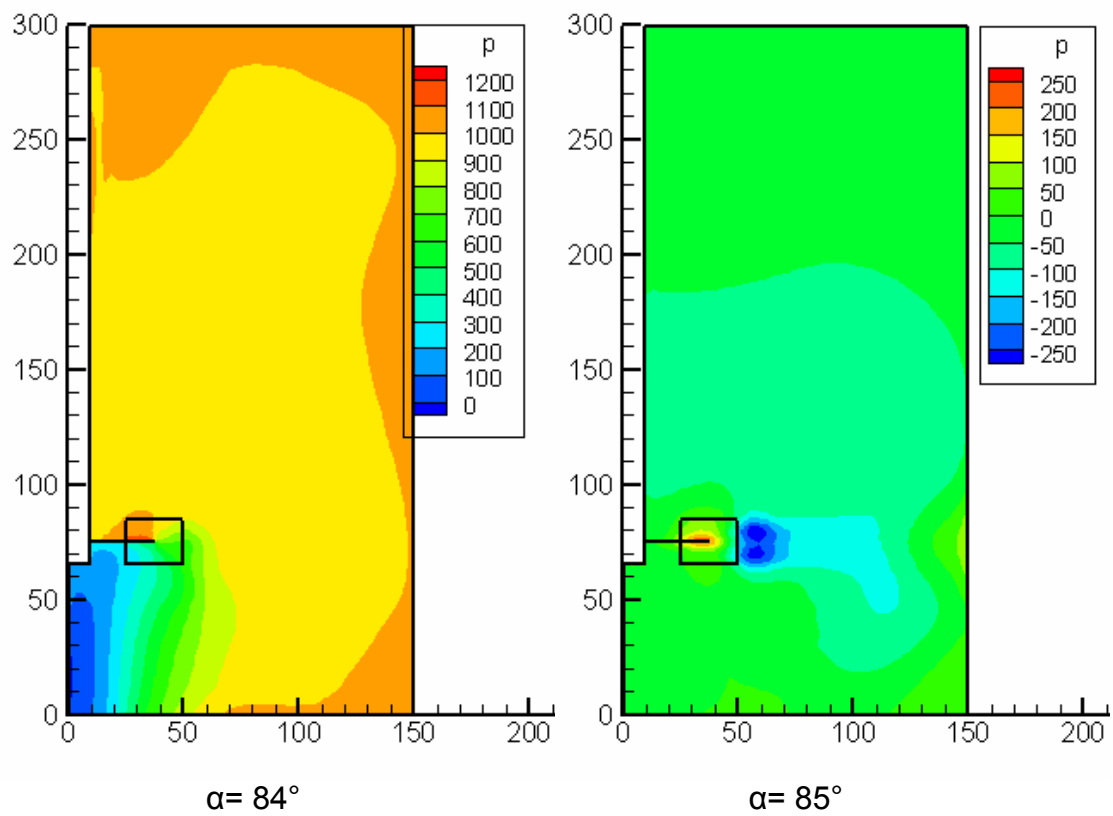


Figure 4.33 The pressure contour of $\alpha = 84^\circ$ and $\alpha = 85^\circ$ at the vertical plane of $\Phi = -30^\circ$.
 ($D = T/3$ $d = 3D/4$ $C = T/4$)

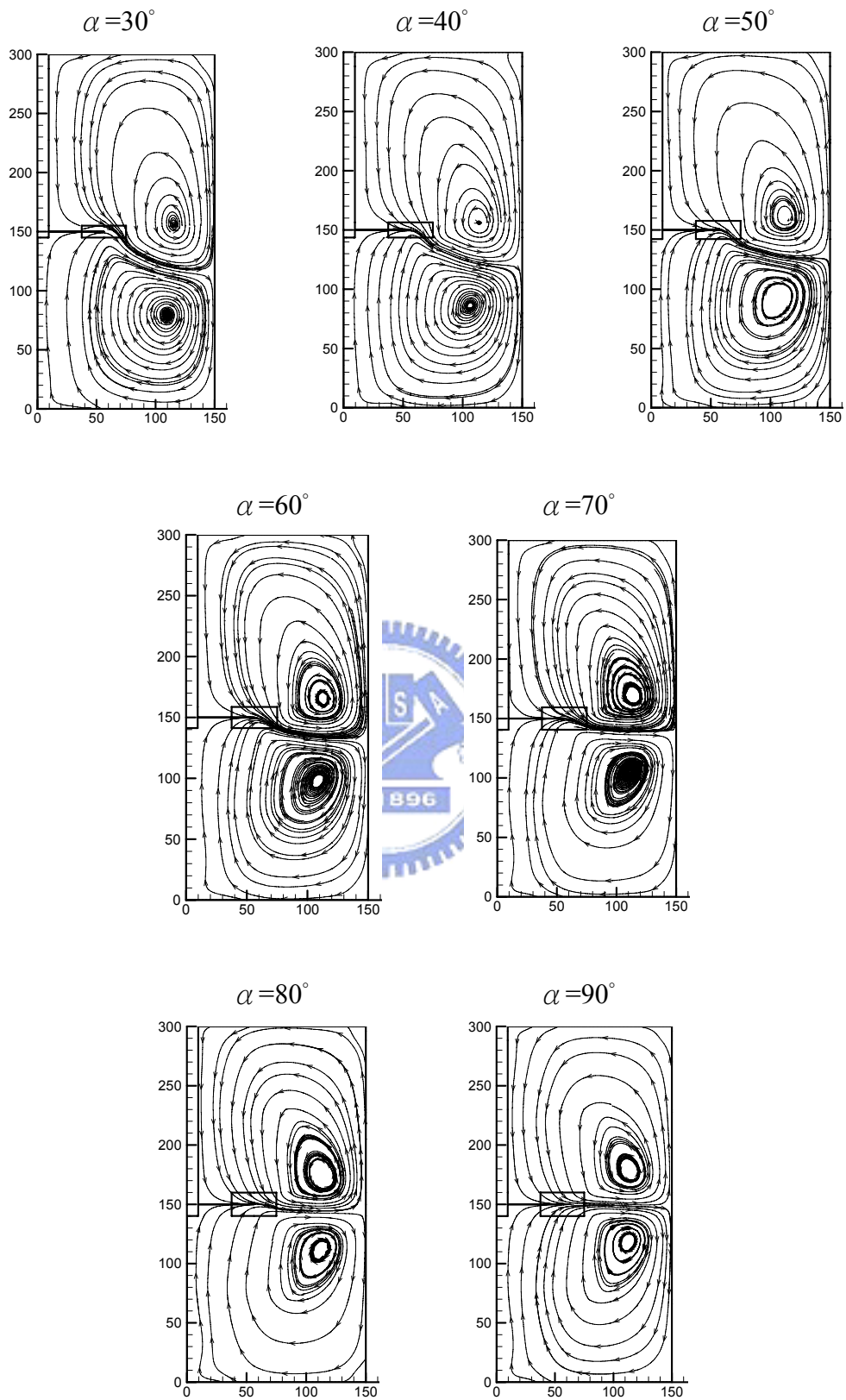


Figure 4.34 Stream lines of various blade angles at $\phi = -30^\circ$. ($D=T/2$ $d=3D/4$ $C=T/2$)

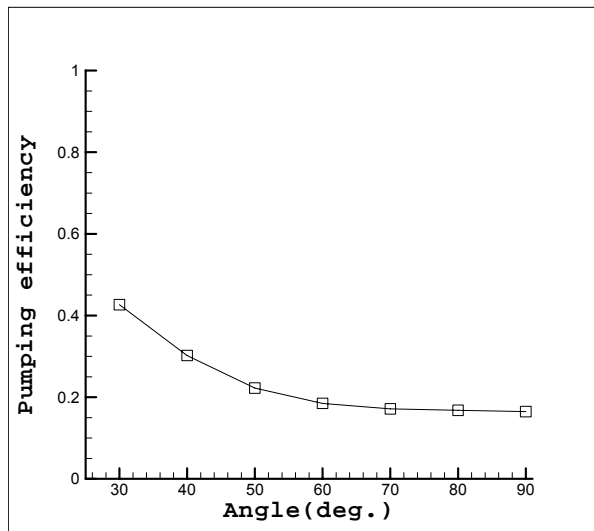
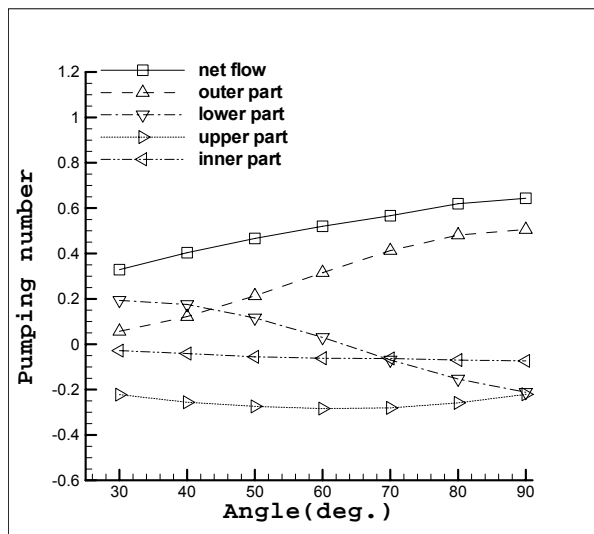
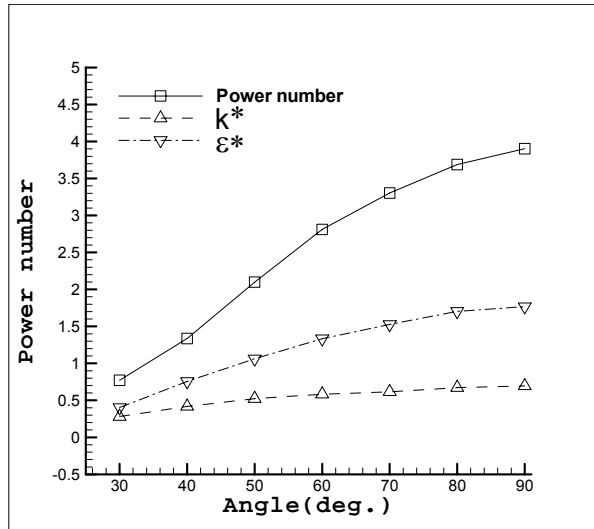


Figure 4.35 The Power number, Pumping number, and Pumping efficiency of various blade angles. ($D=T/2$ $d=3D/4$ $C=T/2$)

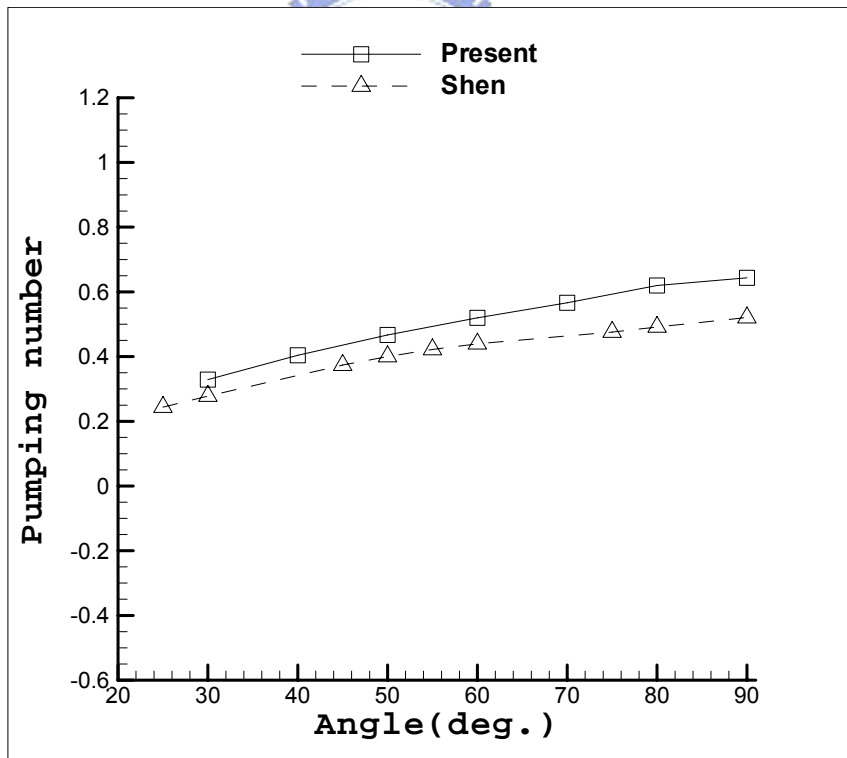
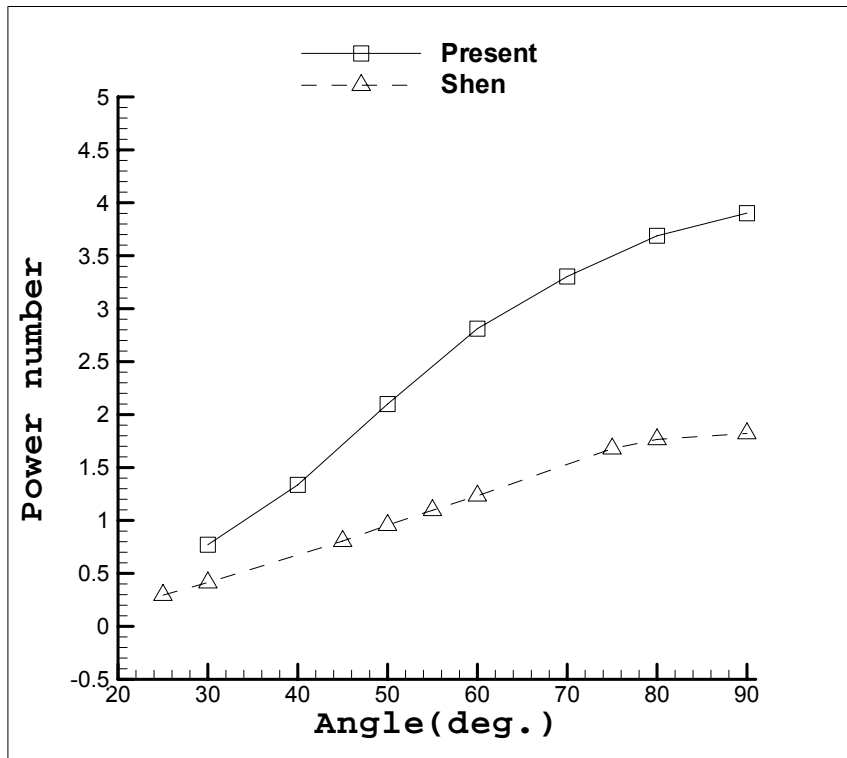


Figure 4.36 The angular profile of Power number and Pumping number compare with Shen's work. ($D=T/2$ $d=3D/4$ $C=T/2$)

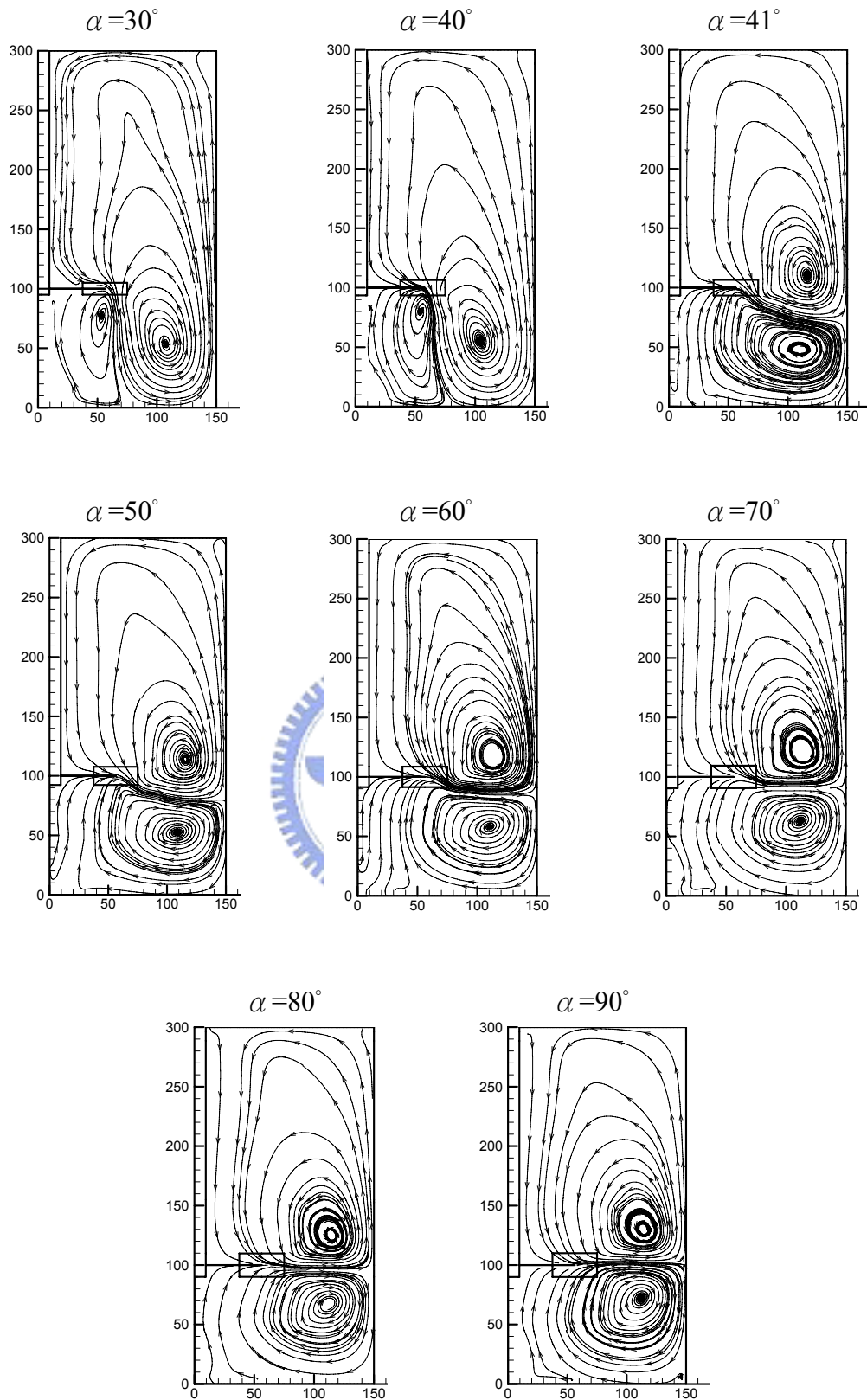


Figure 4.37 Stream lines of various blade angles at the vertical plane of $\varphi = -30^\circ$.
 ($D=T/2$ $d=3D/4$ $C=T/3$)

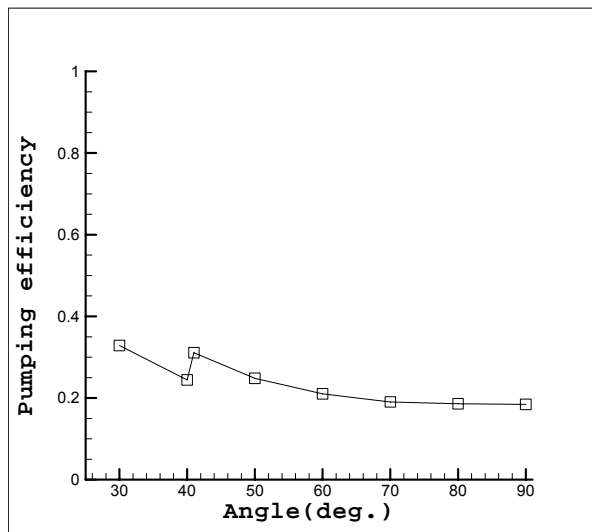
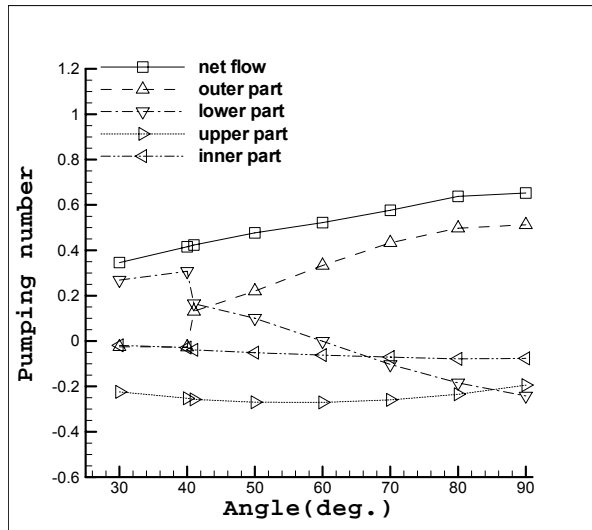
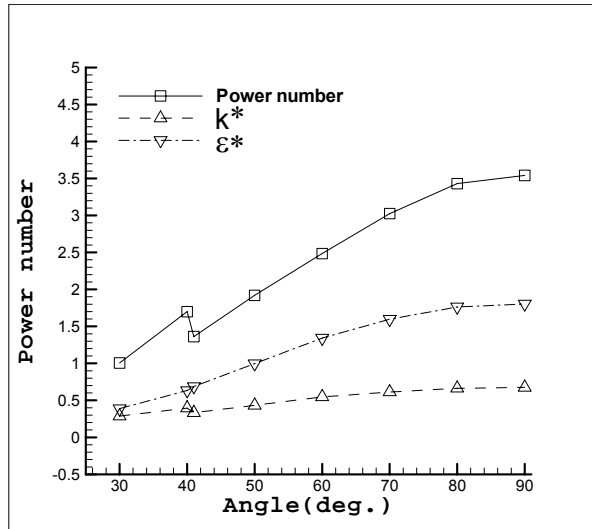


Figure 4.38 The Power number, Pumping number, and Pumping efficiency of various blade angles. ($D=T/2$ $d=3D/4$ $C=T/3$)

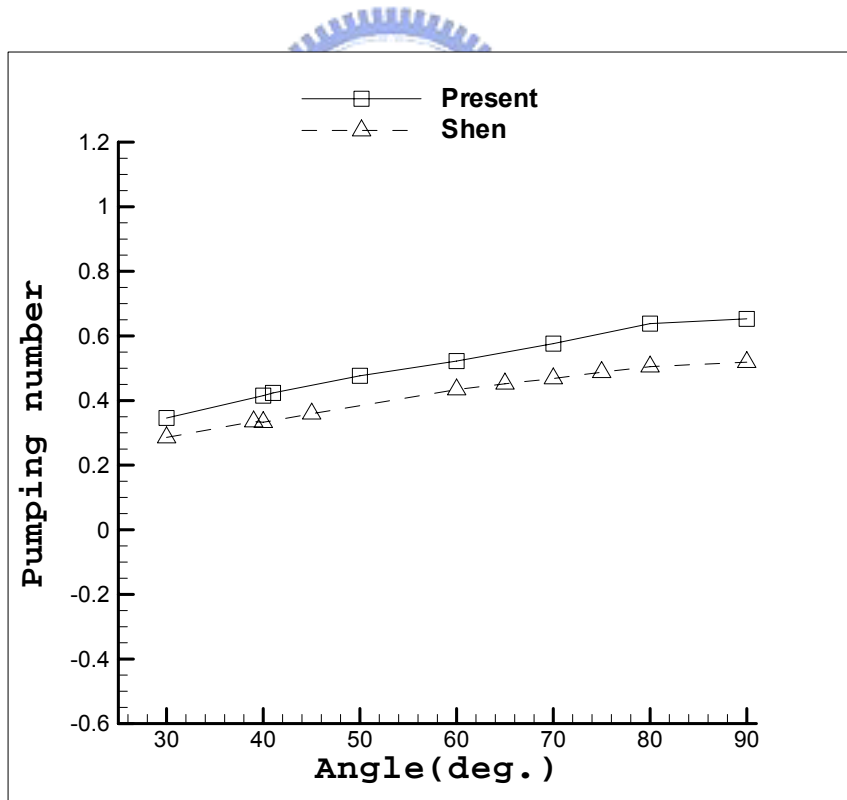
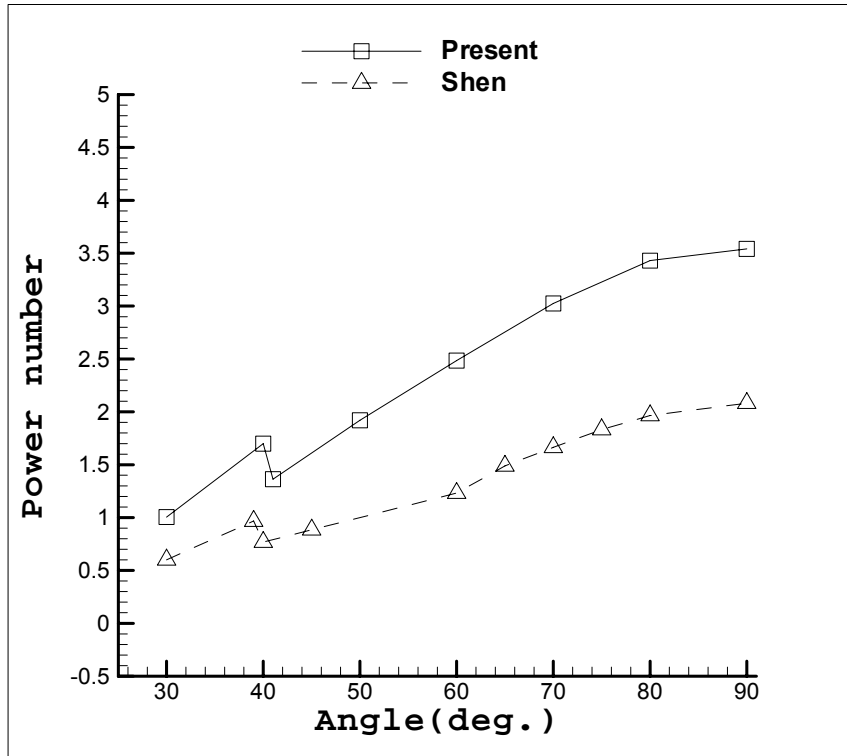


Figure 4.39 The angular profile of Power number and Pumping number compare with Shen's work. ($D=T/2$ $d=3D/4$ $C=T/3$)

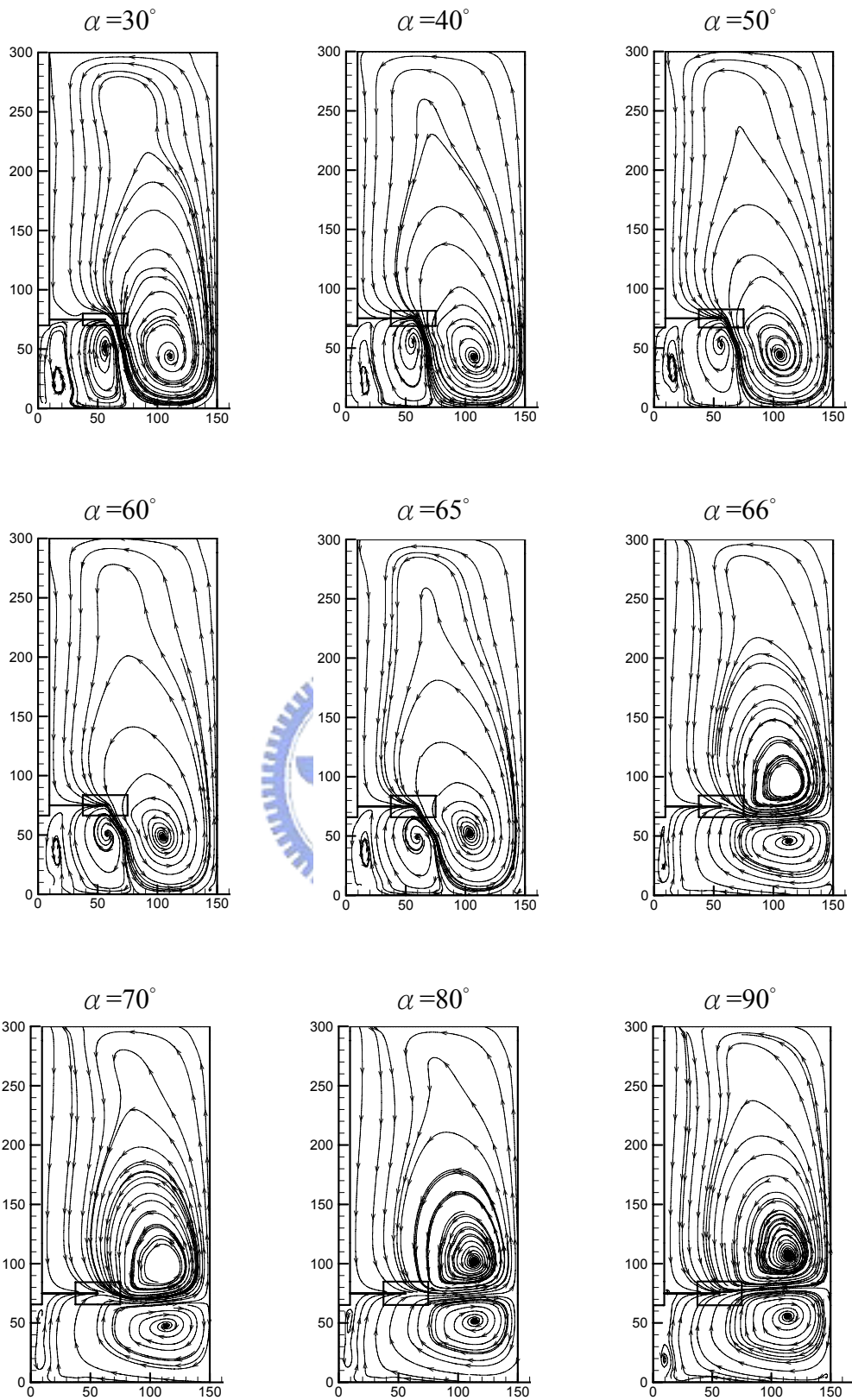


Figure 4.40 Stream lines of various blade angles at the vertical plane of $\varphi = -30^\circ$.
 (D=T/2 d=3D/4 C=T/4)

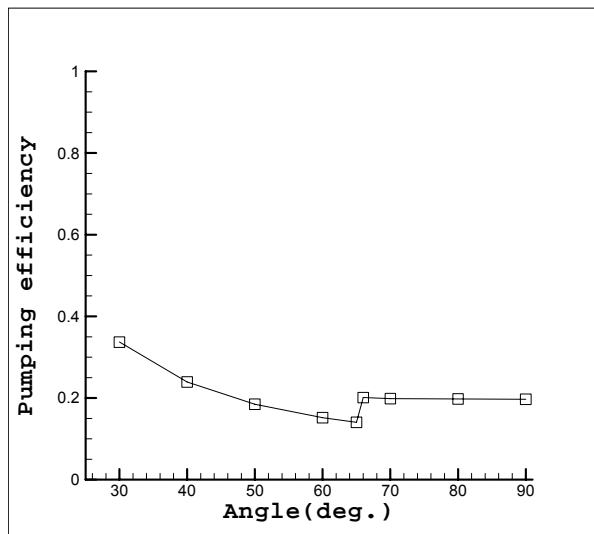
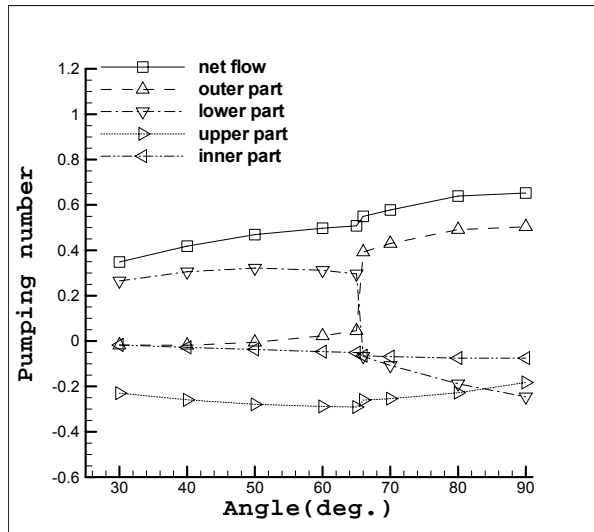
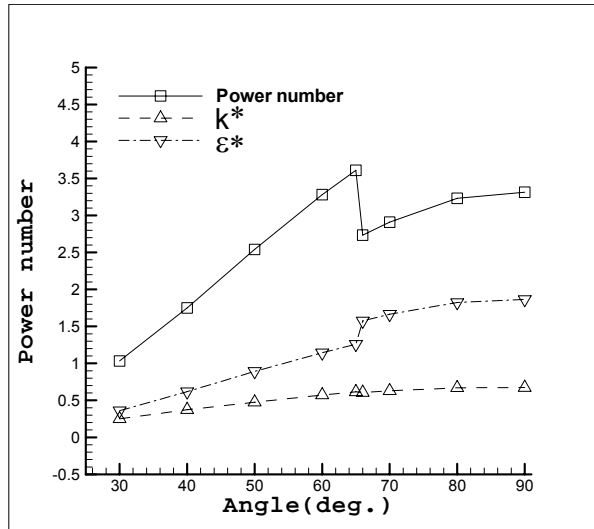


Figure 4.41 The Power number, Pumping number, and Pumping efficiency of various blade angles. ($D=T/2$ $d=3D/4$ $C=T/4$)

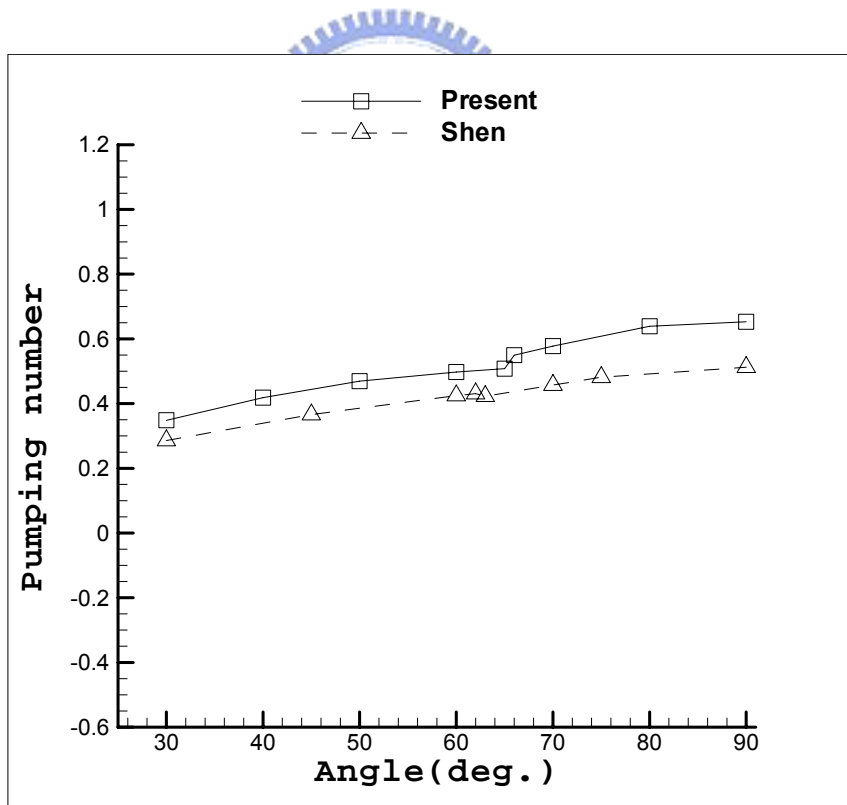
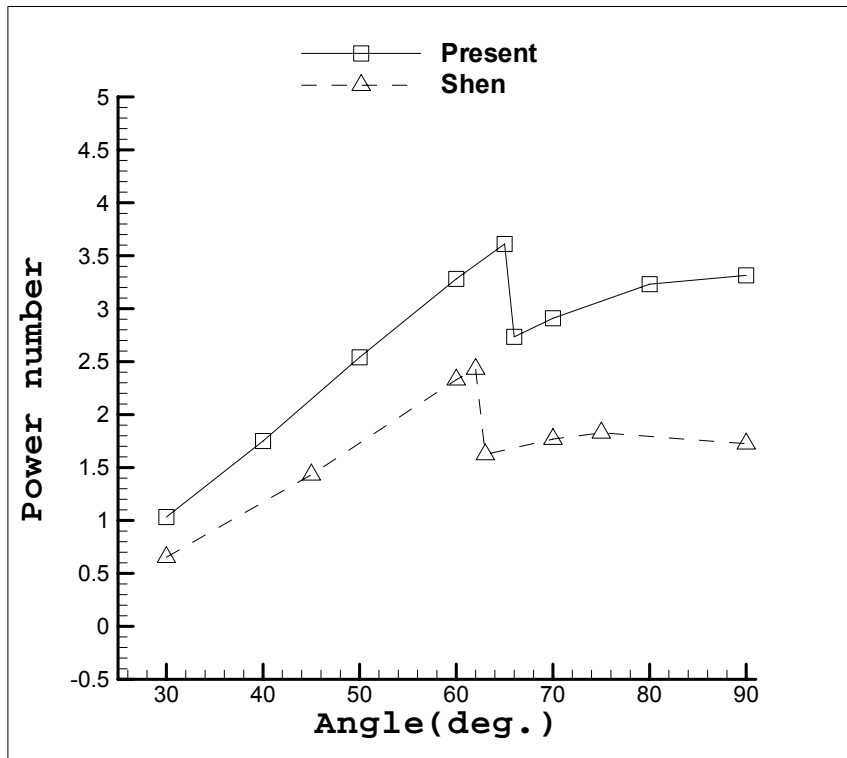


Figure 4.42 The angular profile of Power number and Pumping number compare with Shen's work. ($D=T/2$ $d=3D/4$ $C=T/4$)

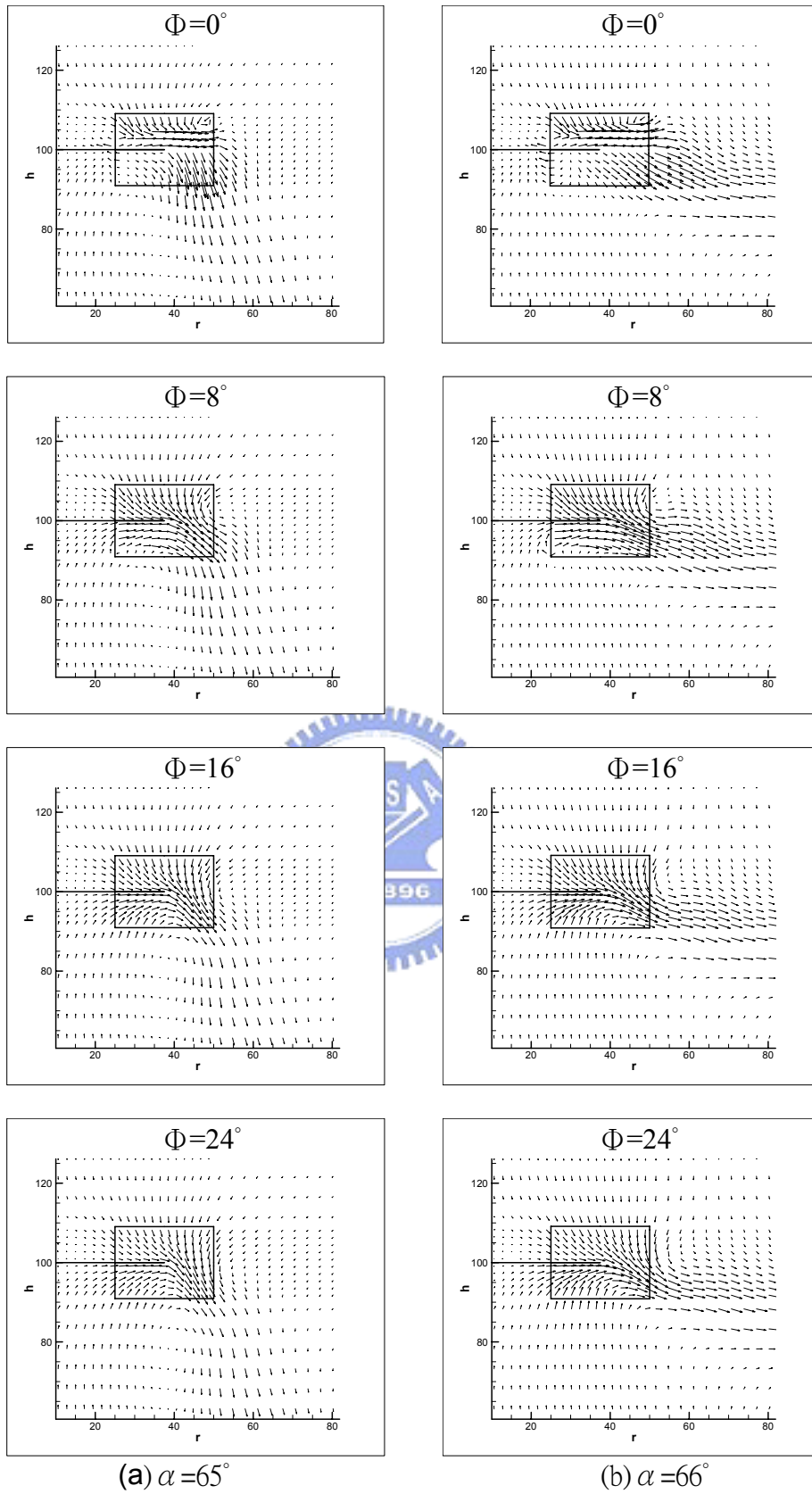


Figure 4.43 Flow field behind the blade ($D=T/3$ $d=3D/4$ $C=T/3$)

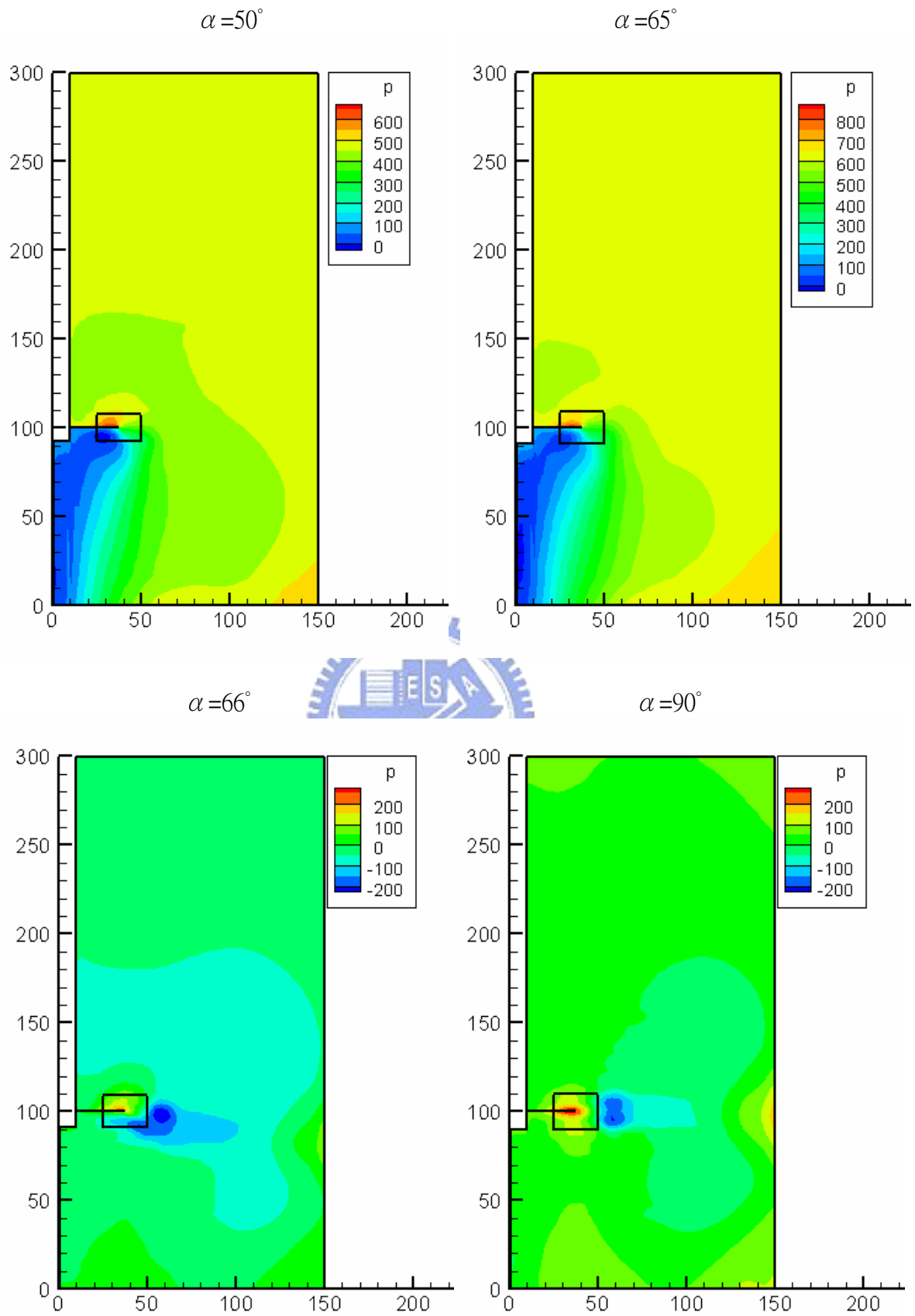


Figure 4.44 Pressure contours of different blade angles ($D=T/3$ $d=3D/4$ $C=T/3$)

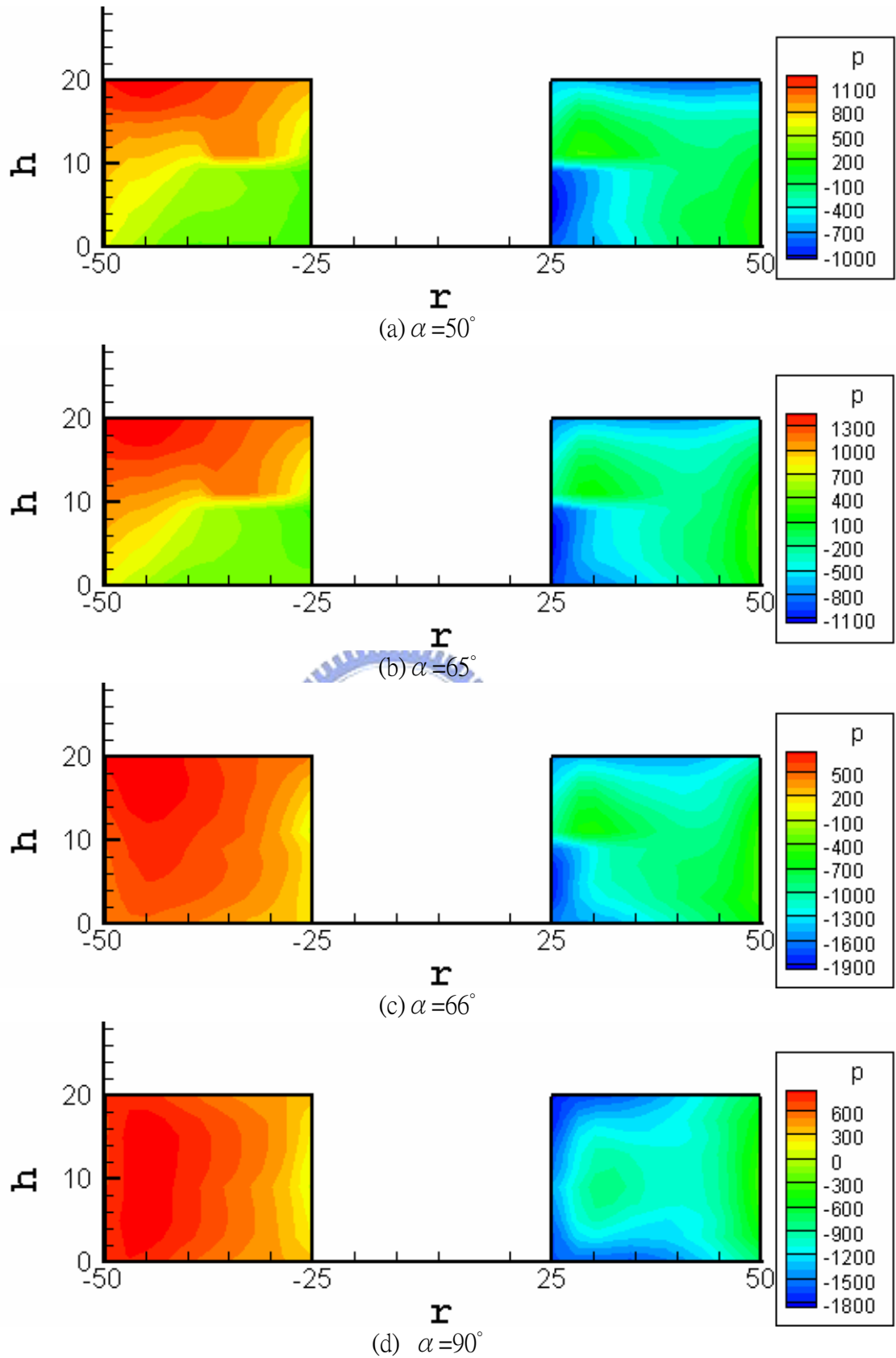
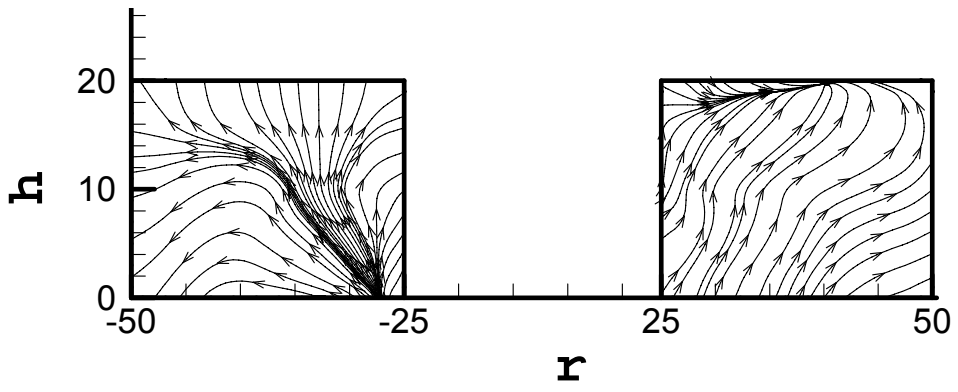
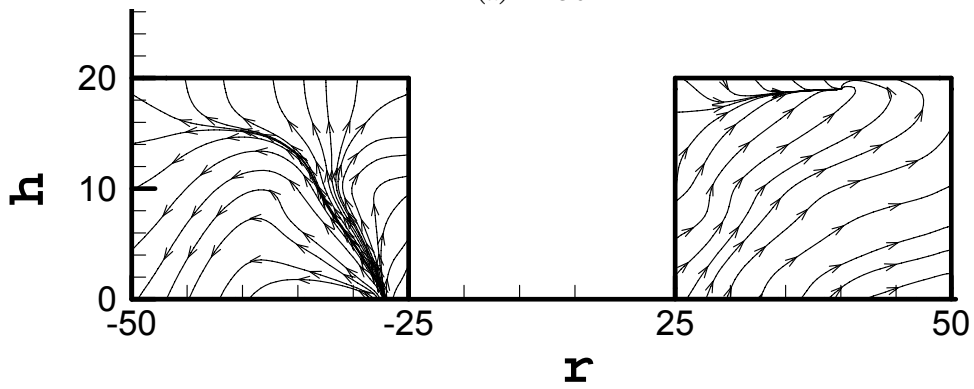


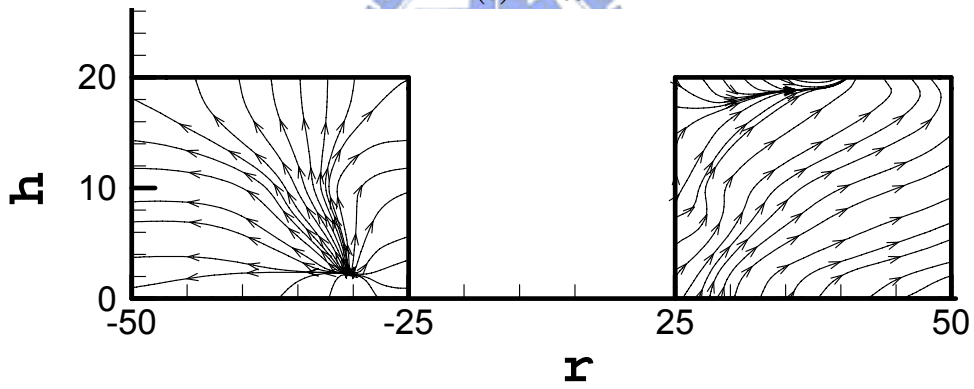
Figure 4.45 Pressure contours on blade surface for different blade angles ($D=T/3$ $d=3D/4$ $C=T/3$)



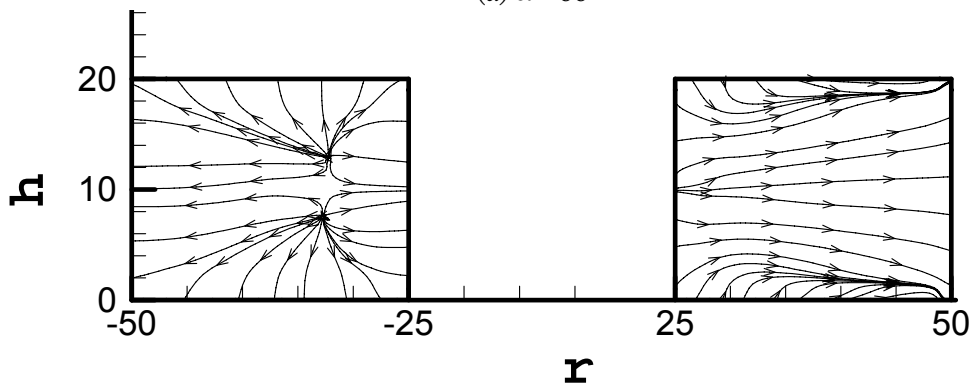
(a) $\alpha = 50^\circ$



(b) $\alpha = 65^\circ$



(a) $\alpha = 66^\circ$



(a) $\alpha = 90^\circ$

Figure 4.46 Stream lines on blade surface for different blade angles ($D=T/3$ $d=3D/4$ $C=T/3$)

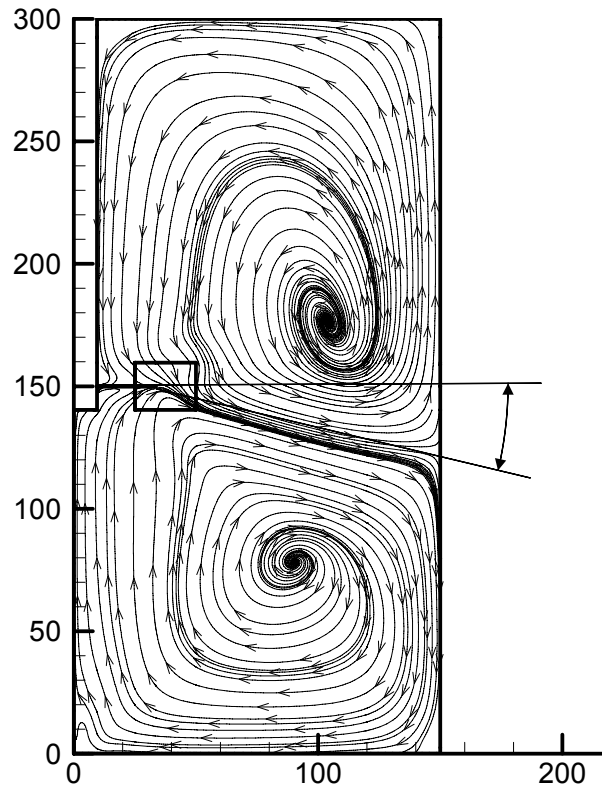
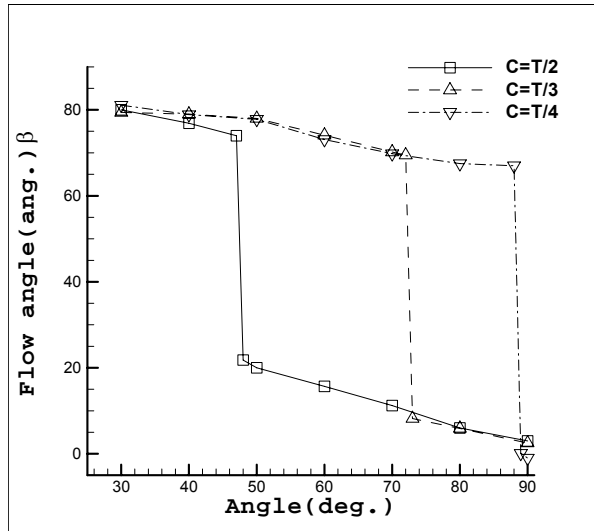
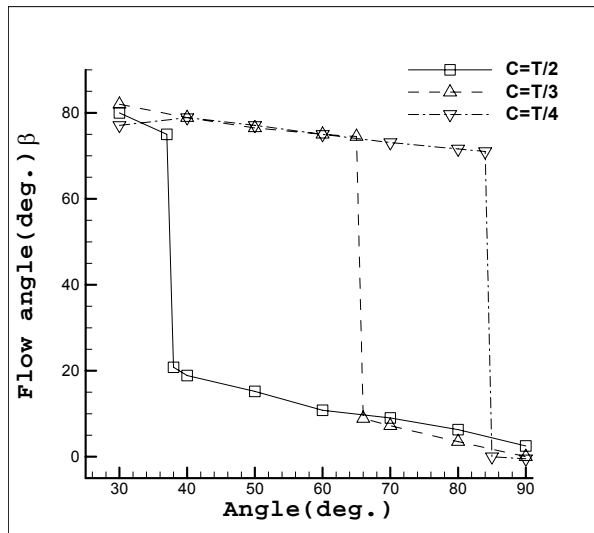


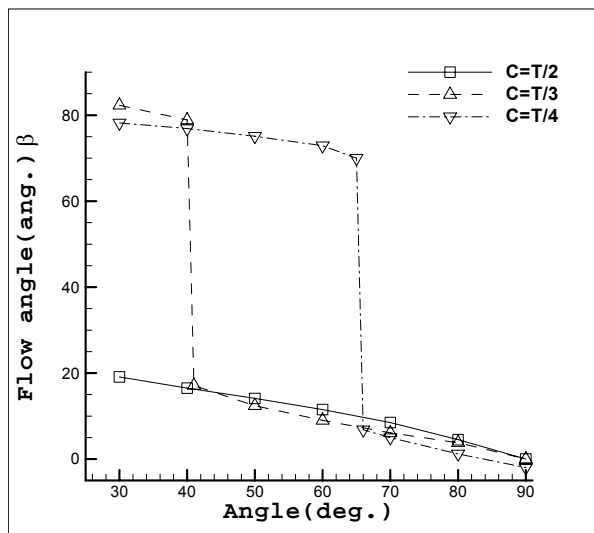
Figure 4.47 The definition of flow out angle



(a) $D=T/3$ $d=2D/3$

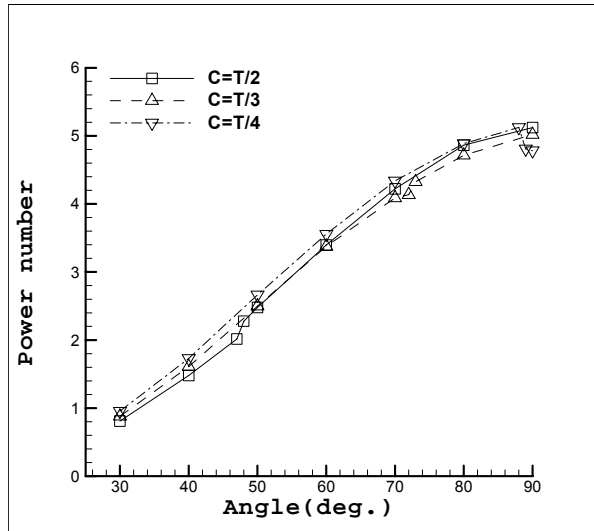


(a) $D=T/3$ $d=3D/4$

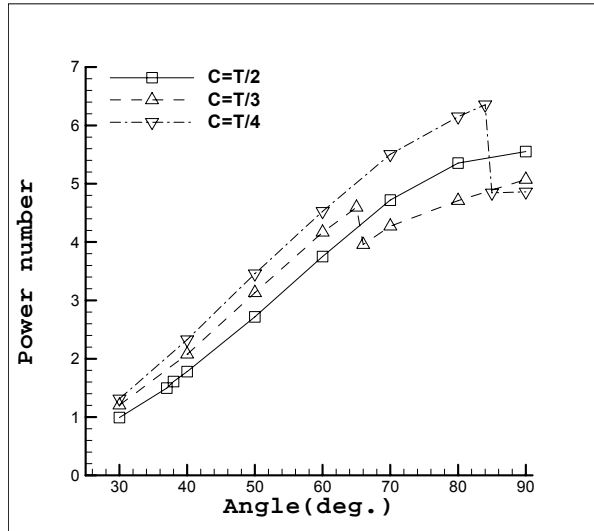


(a) $D=T/2$ $d=3D/4$

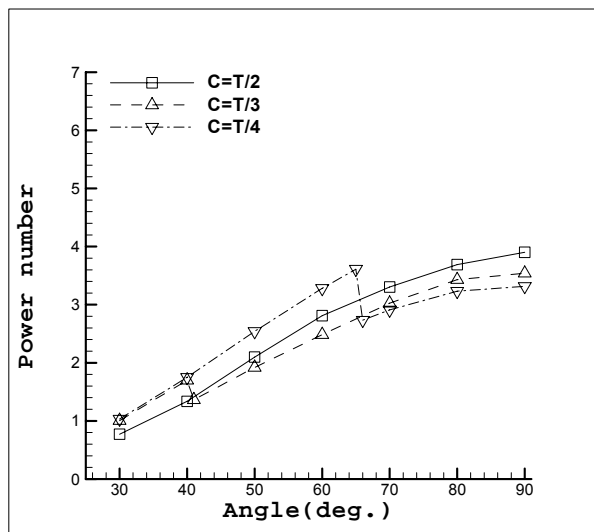
Figure 4.48 Angular profiles of flow out angle for different off-bottom clearance



(a) $D=T/3$ $d=2D/3$

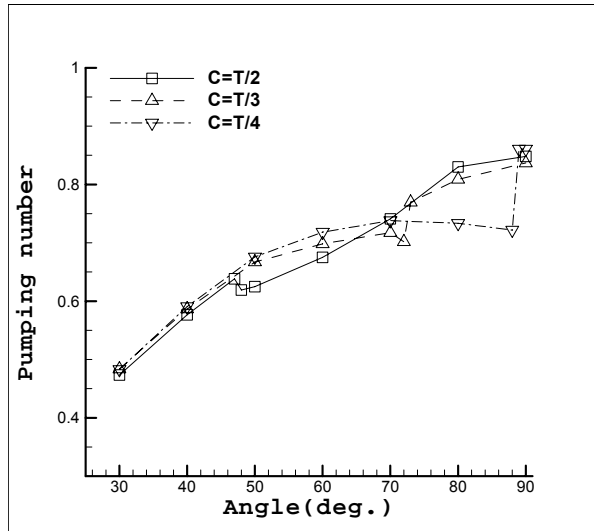


(b) $D=T/3$ $d=3D/4$

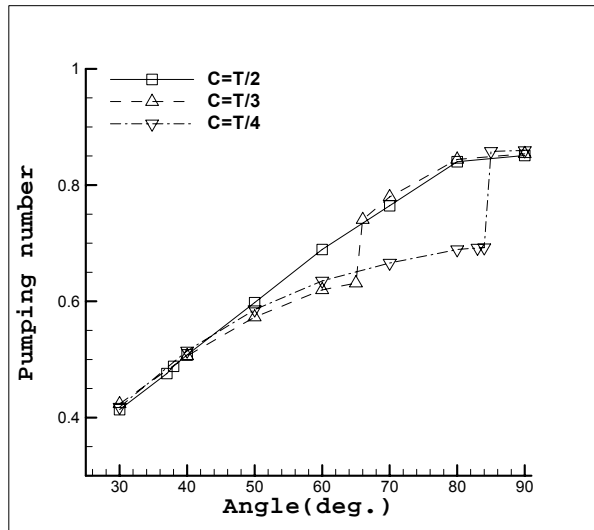


(c) $D=T/2$ $d=3D/4$

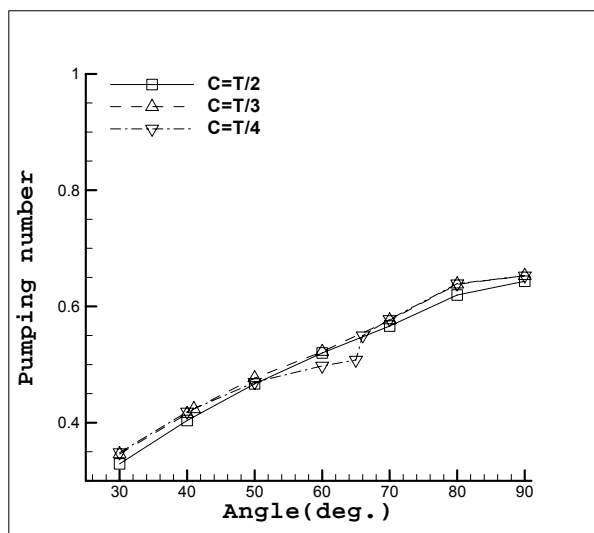
Figure 4.49 Radial profiles of Power number for different off-bottom clearance



(a) $D=T/3$ $d=2D/3$

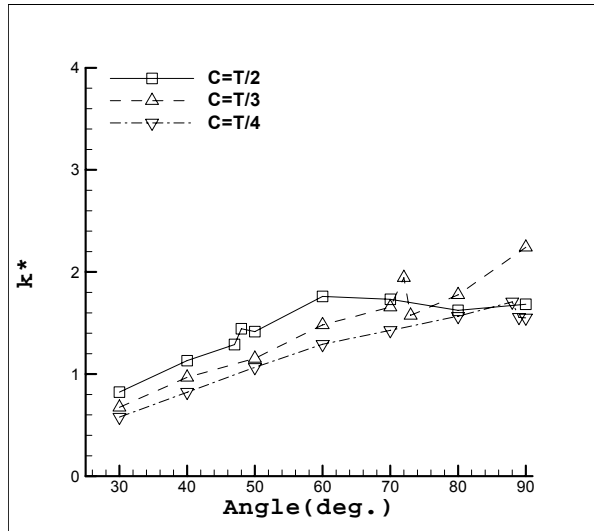


(b) $D=T/3$ $d=3D/4$

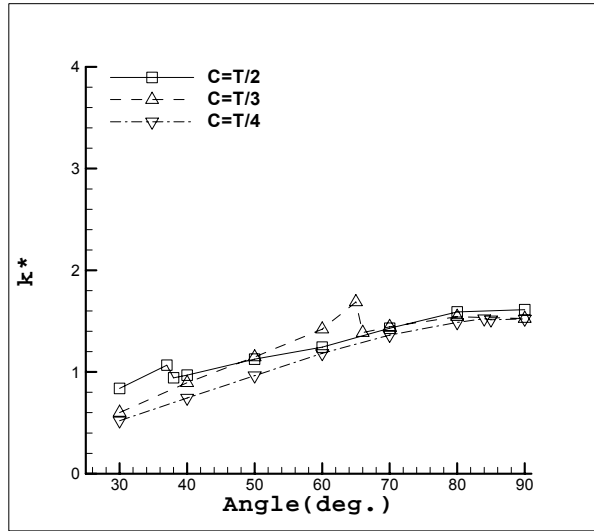


(c) $D=T/2$ $d=3D/4$

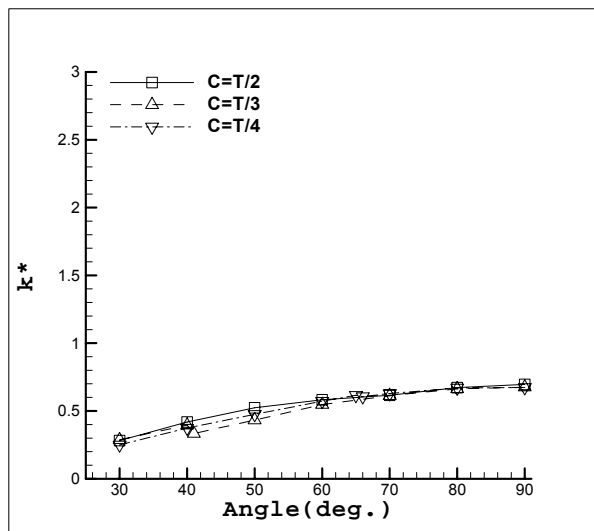
Figure 4.50 Radial profiles of Pumping number for different off-bottom clearance



(a) $D=T/3$ $d=2D/3$

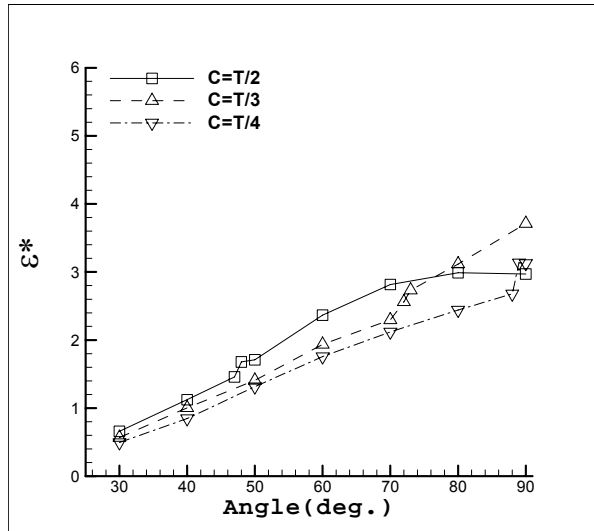


(b) $D=T/3$ $d=3D/4$

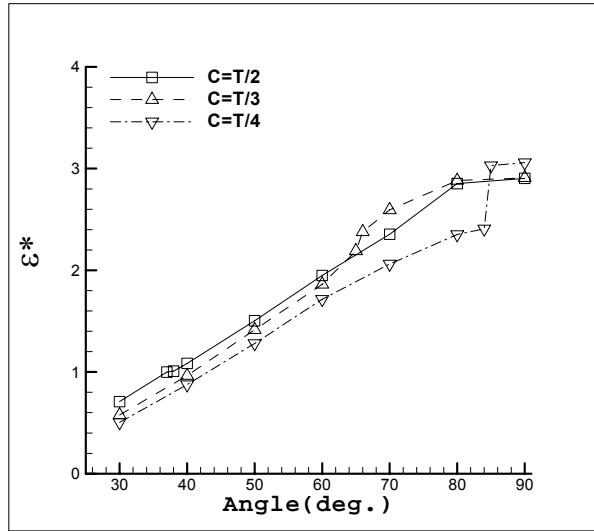


(c) $D=T/2$ $d=3D/4$

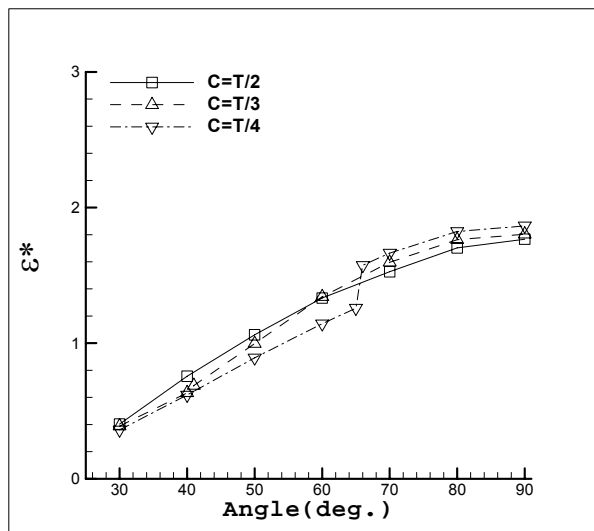
Figure 4.51 Radial profiles of k^* for different off-bottom clearance



(a) $D=T/3$ $d=2D/3$

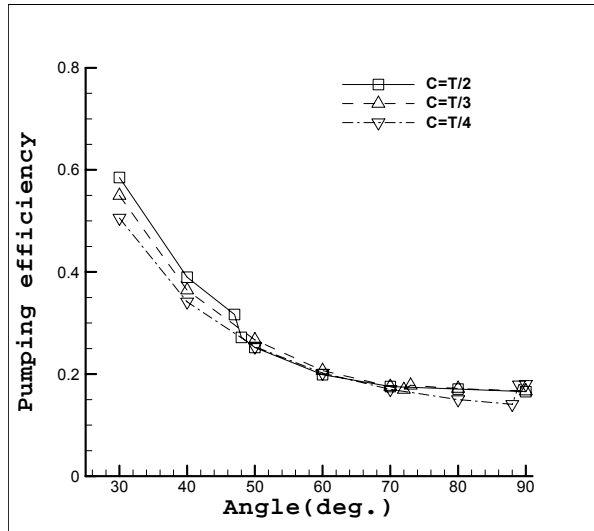


(b) $D=T/3$ $d=3D/4$

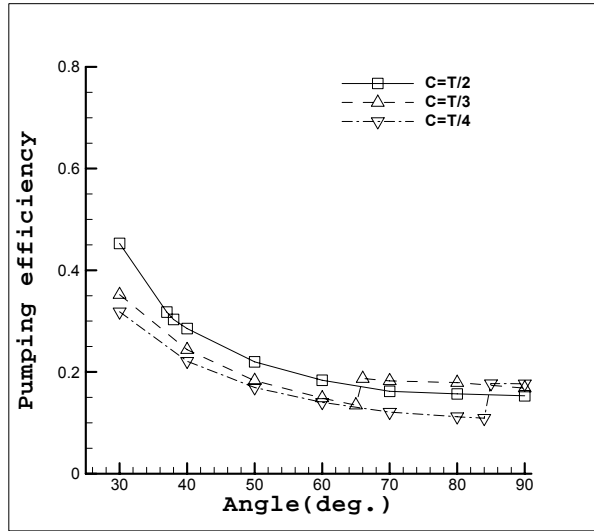


(c) $D=T/2$ $d=3D/4$

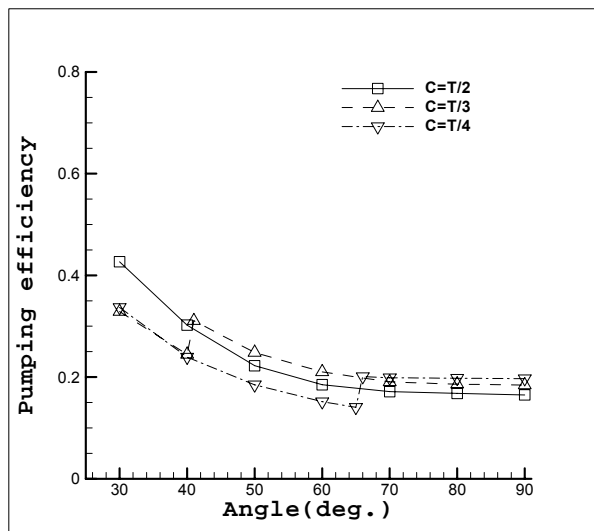
Figure 4.52 Radial profiles of ϵ^* for different off-bottom clearance



(a) $D=T/3$ $d=2D/3$



(b) $D=T/3$ $d=3D/4$



(c) $D=T/2$ $d=3D/4$

Figure 4.53 Radial profiles of pumping efficiency for different off-bottom clearance

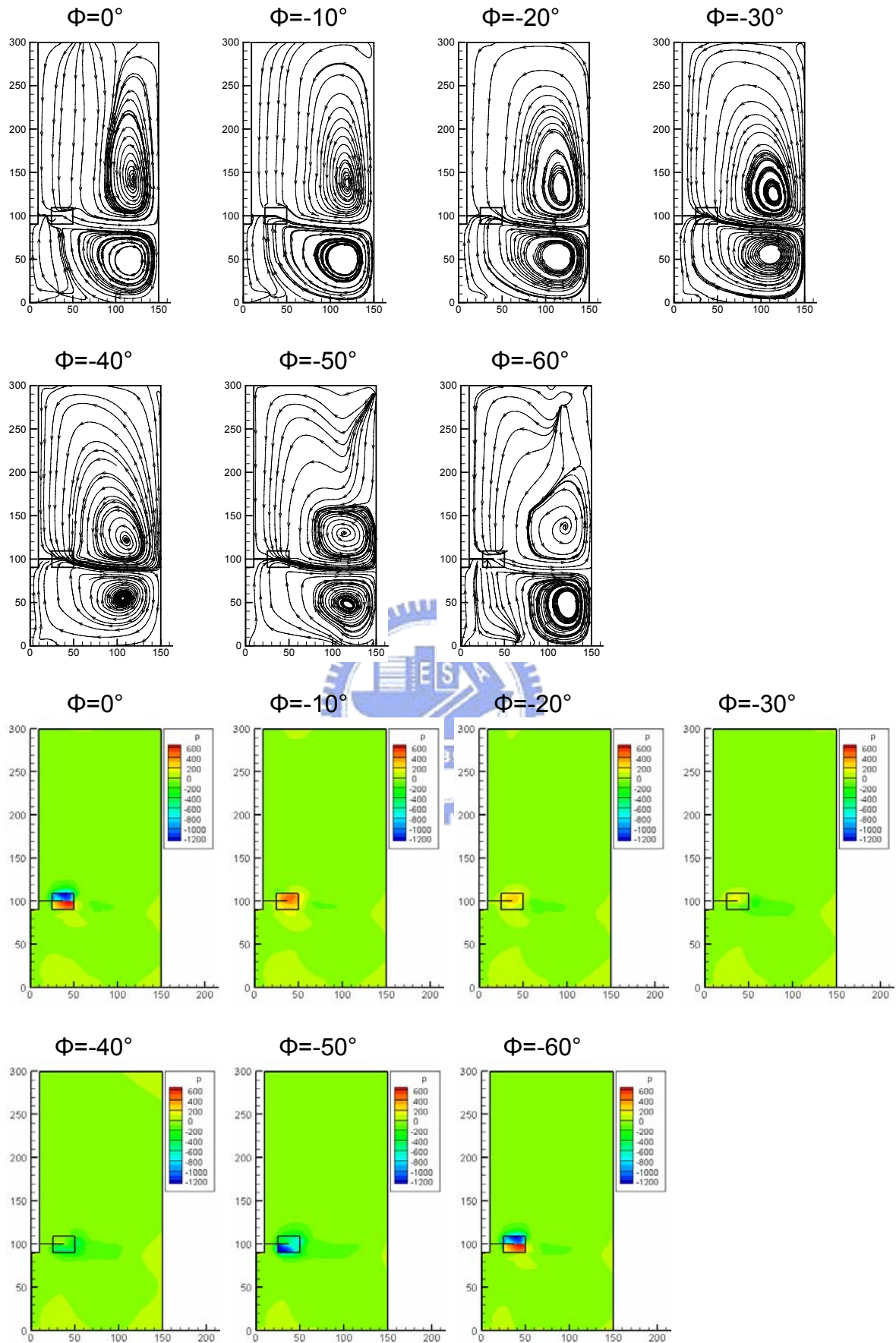


Figure 4.54 The stream lines and contours of stirred tank at different vertical plane when the blade angle $\alpha=70^\circ$ ($D=T/3$ $d=3D/4$ $C=T/3$)

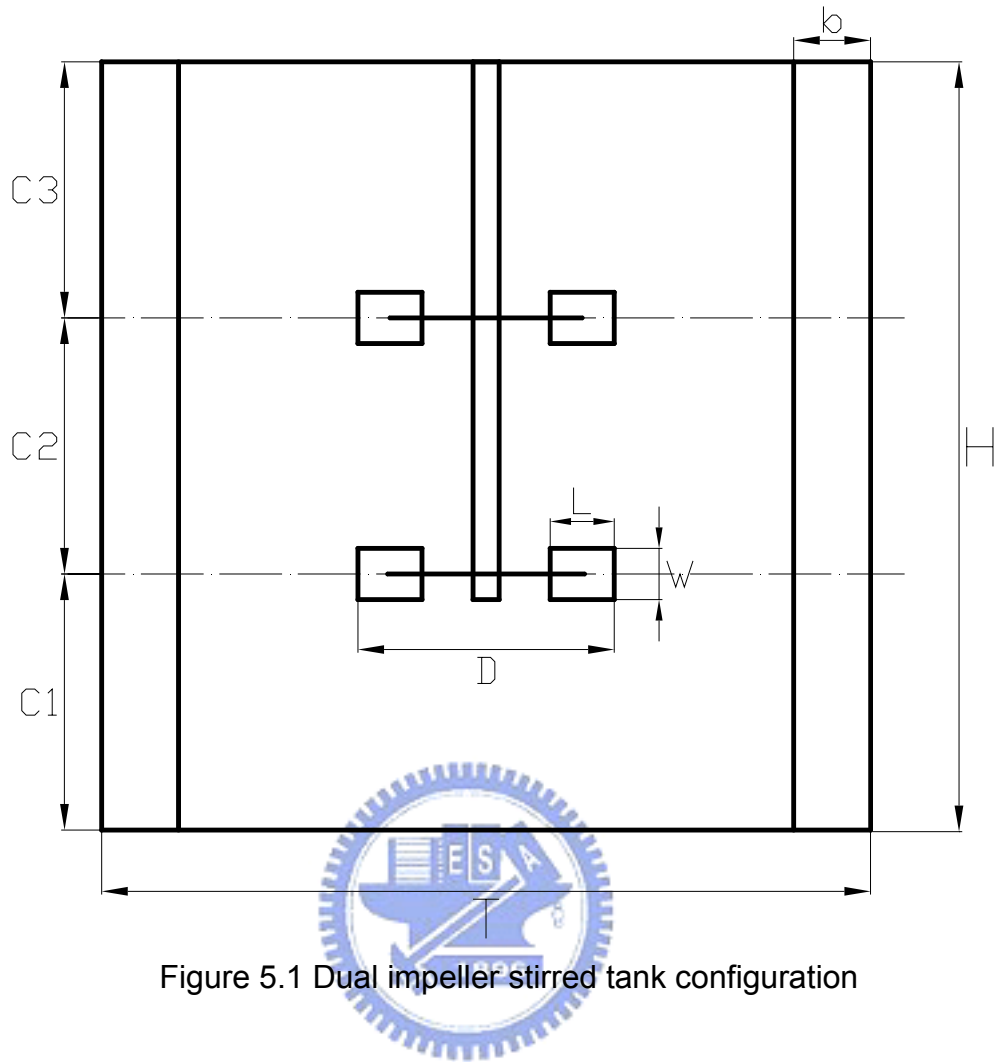


Figure 5.1 Dual impeller stirred tank configuration

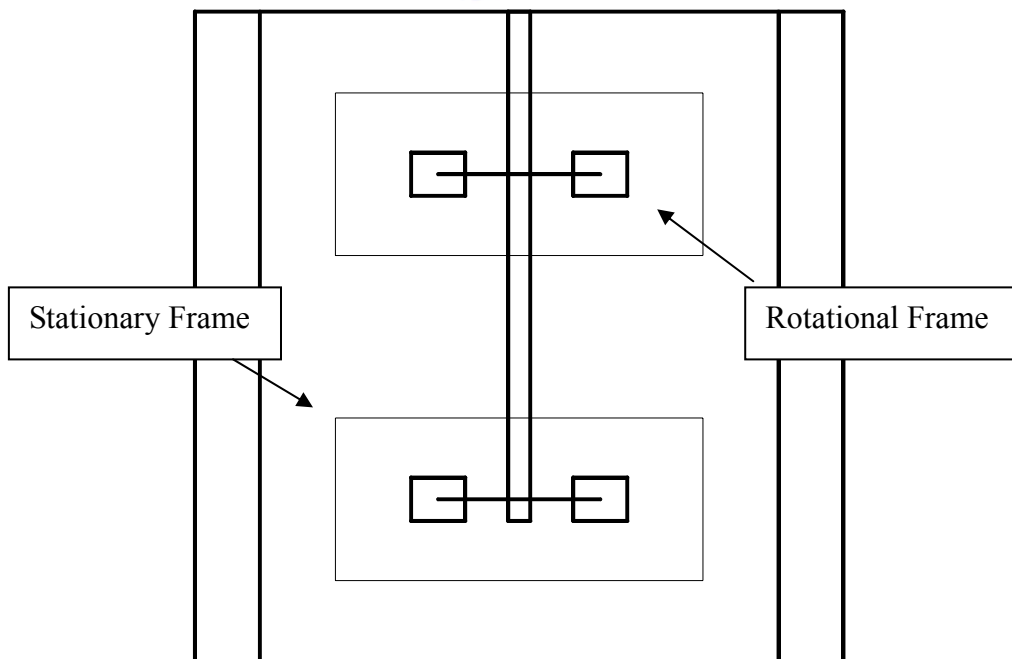


Figure 5.2 Multiple reference of parallel flow

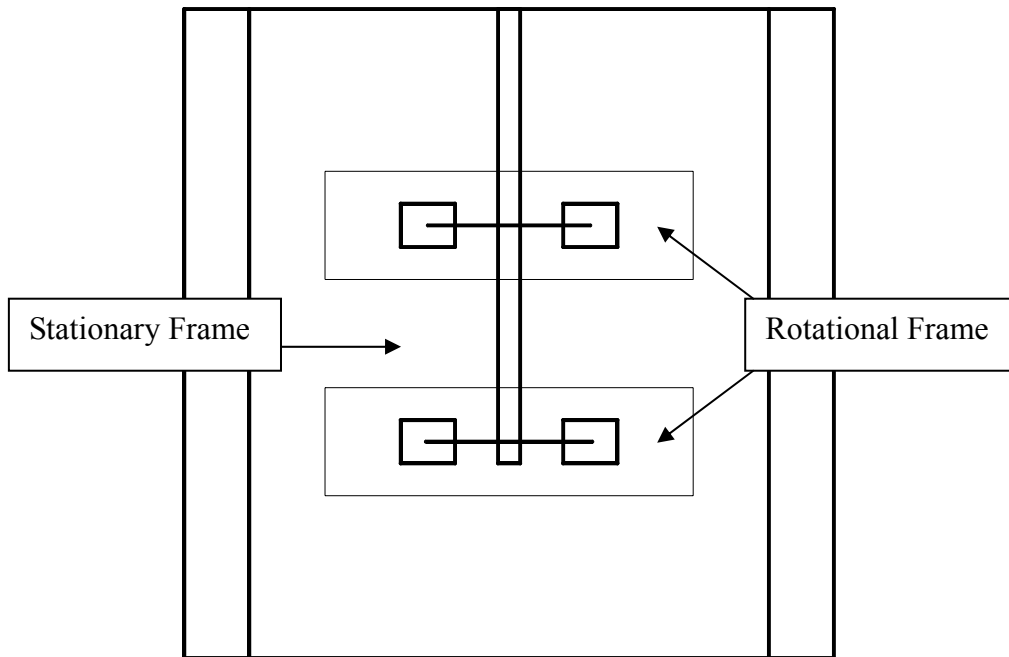


Figure 5.3 Multiple reference of merging flow

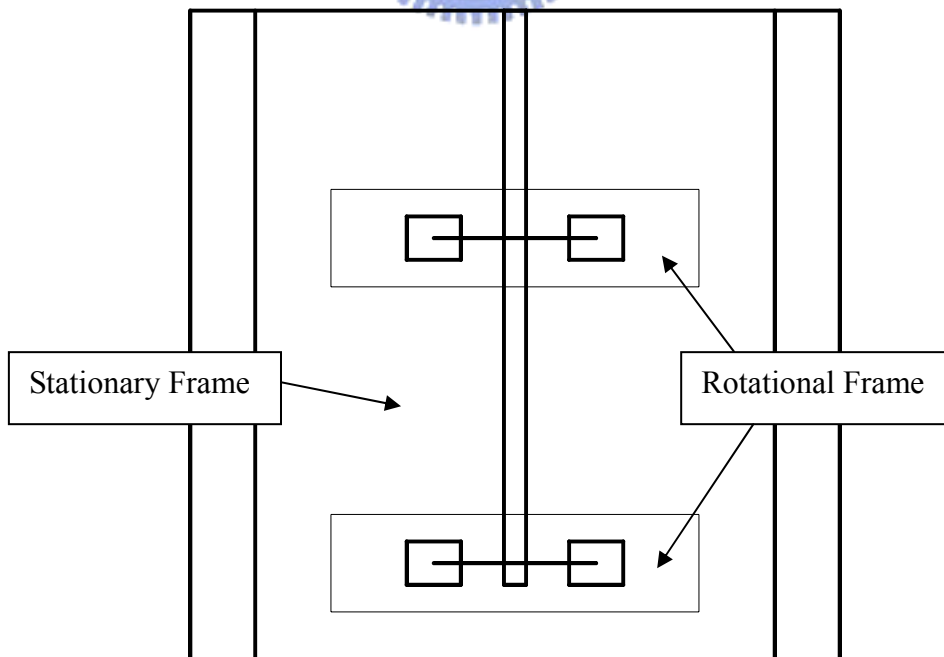
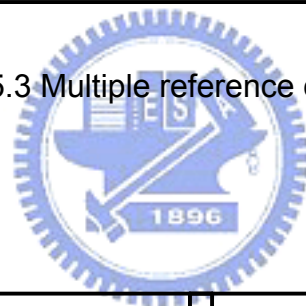


Figure 5.4 Multiple reference of diverging flow

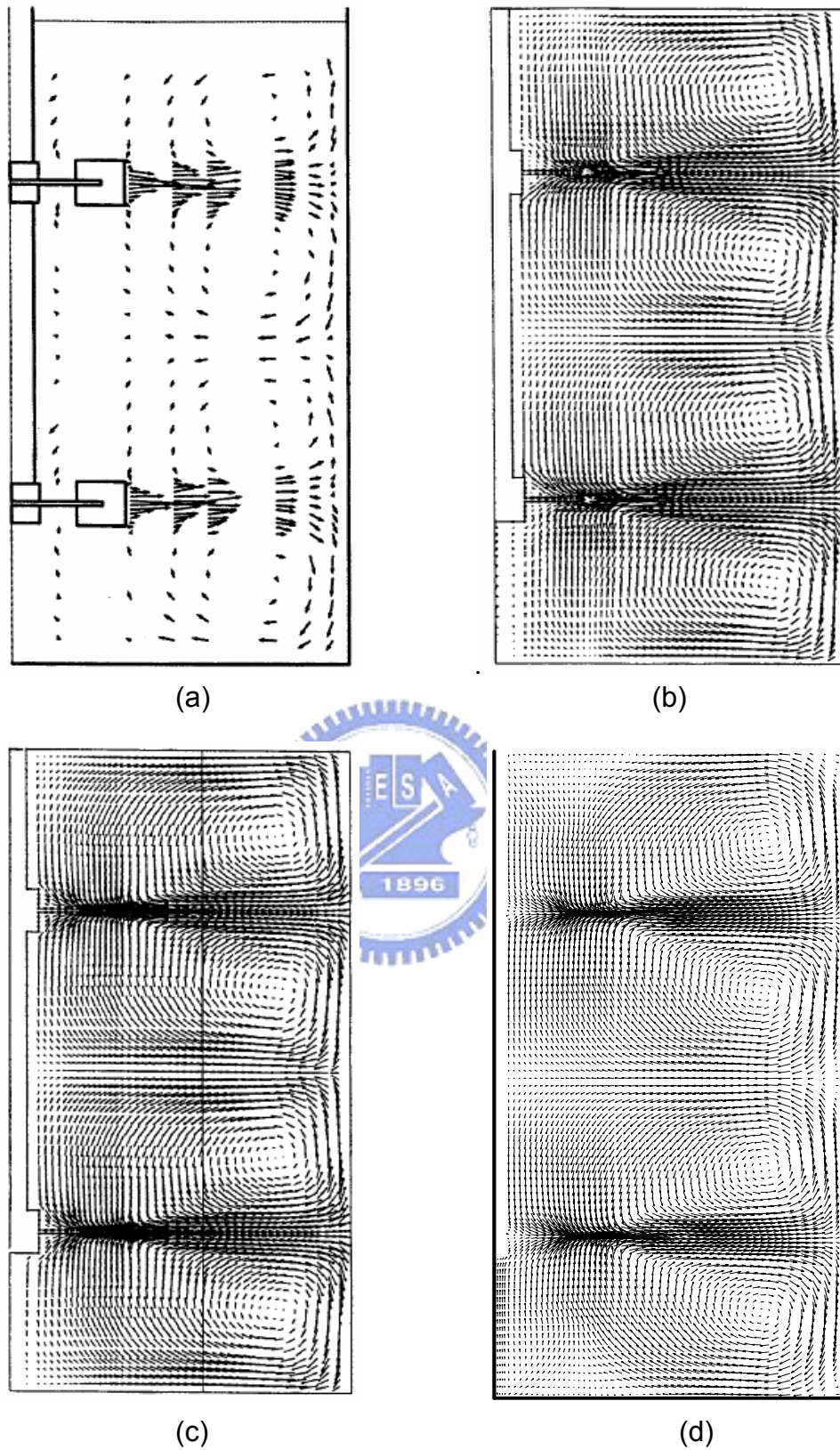


Figure 5.5 Parallel flow: comparison of velocity vector plots in a plane midway between baffles. (a) Experimental results [9] (b) Predictions, IO technique [22] (c) Predictions, SG technique [22] (d) Predictions, MRF technique (present)

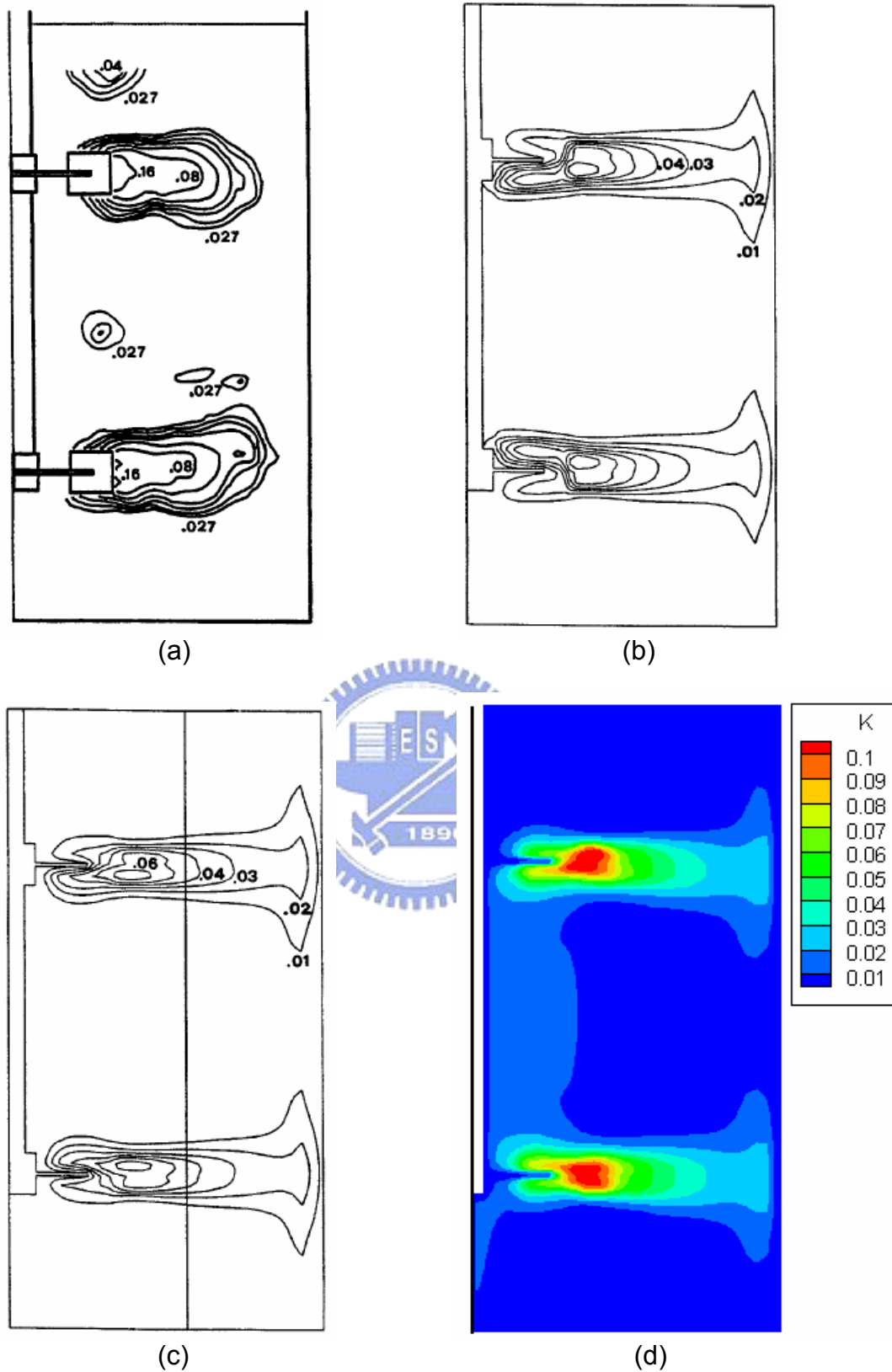
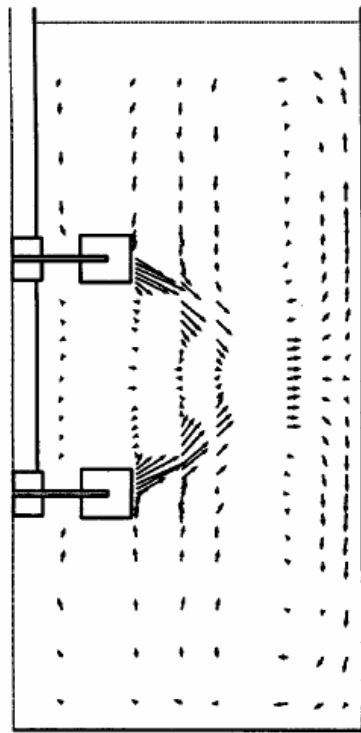
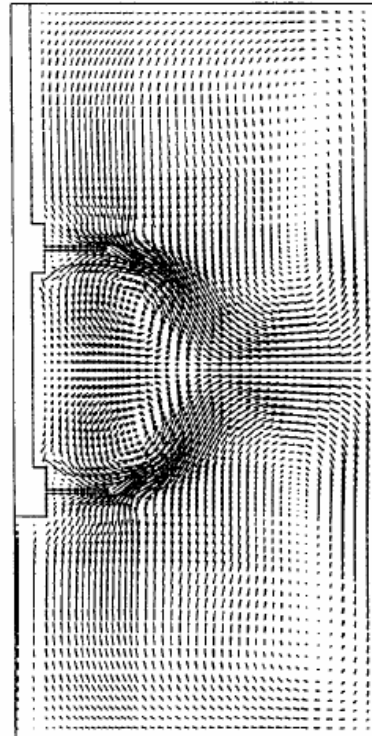


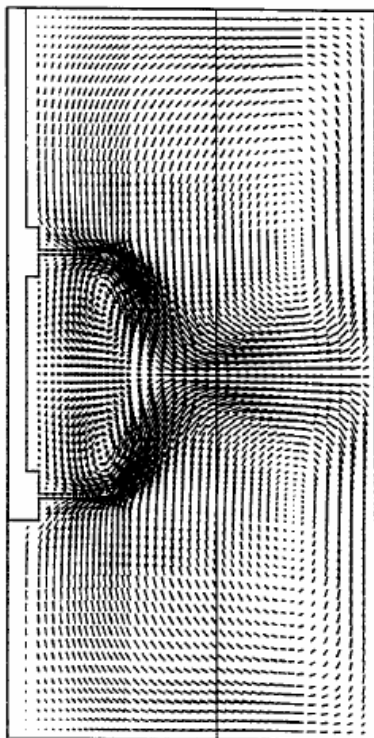
Figure 5.6 Parallel flow: Comparison of turbulence energy distribution in a plane midway between baffles (a) Experimental results [9] (b) Predictions, IO technique [22] (c) Predictions, SG technique [22] (d) Predictions, MRF technique (present)



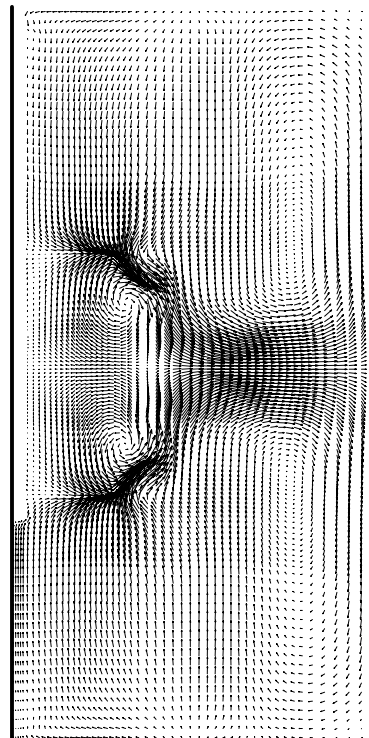
(a)



(b)



(c)



(d)

Figure 5.7 Merging flow: Comparison of velocity vector plots in a plane midway between baffles. (a) Experimental results [9] (b) Predictions, IO technique [22] (c) Predictions, SG technique [22] (d) Predictions, MRF technique (present)

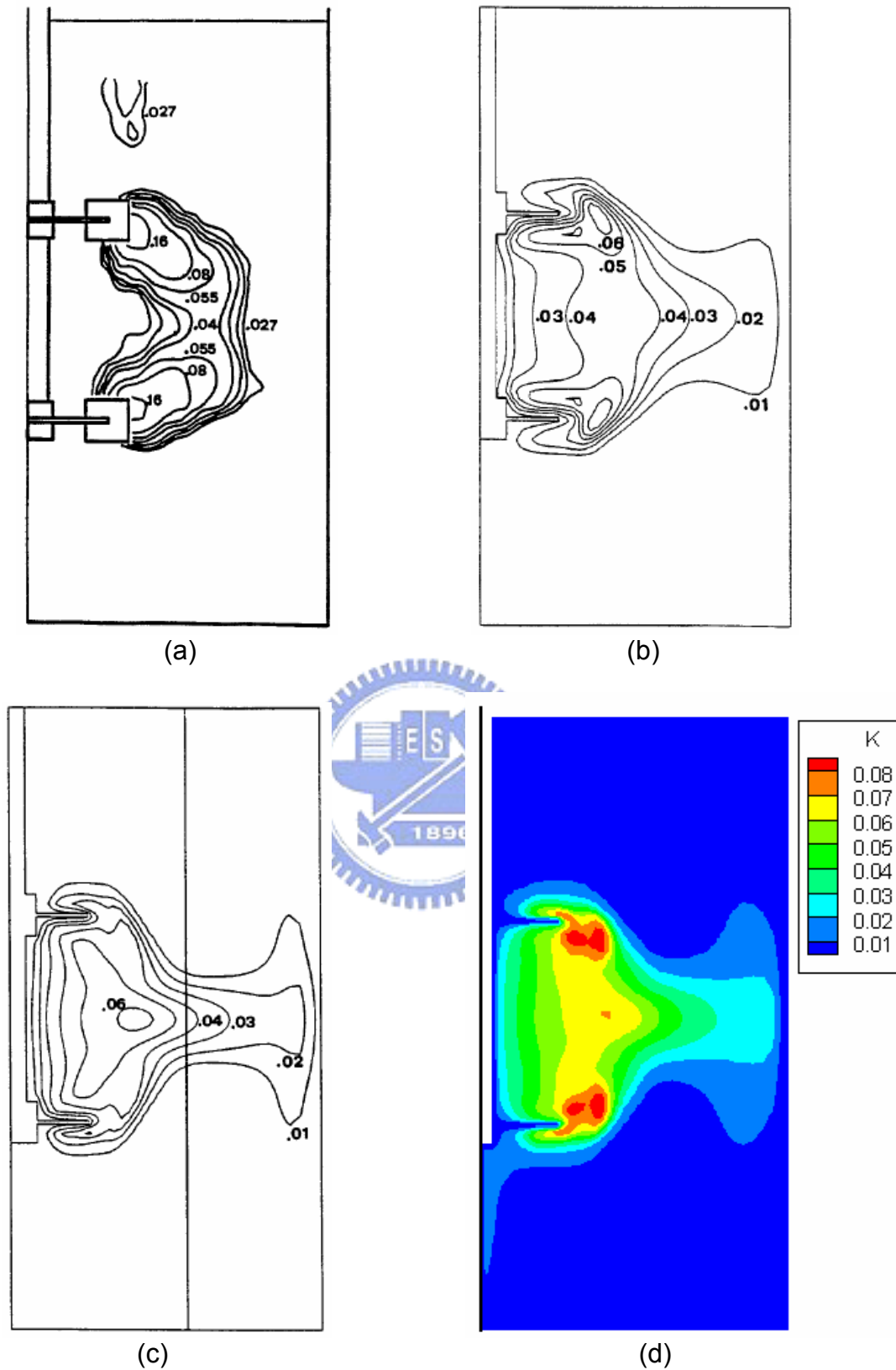


Figure 5.8 Merging flow: Comparison of turbulence energy distributions in a plane midway between baffles. (a) Experimental results [9] (b) Predictions, IO technique [22] (c) Predictions, SG technique [22] (d) Predictions, MRF technique (present)

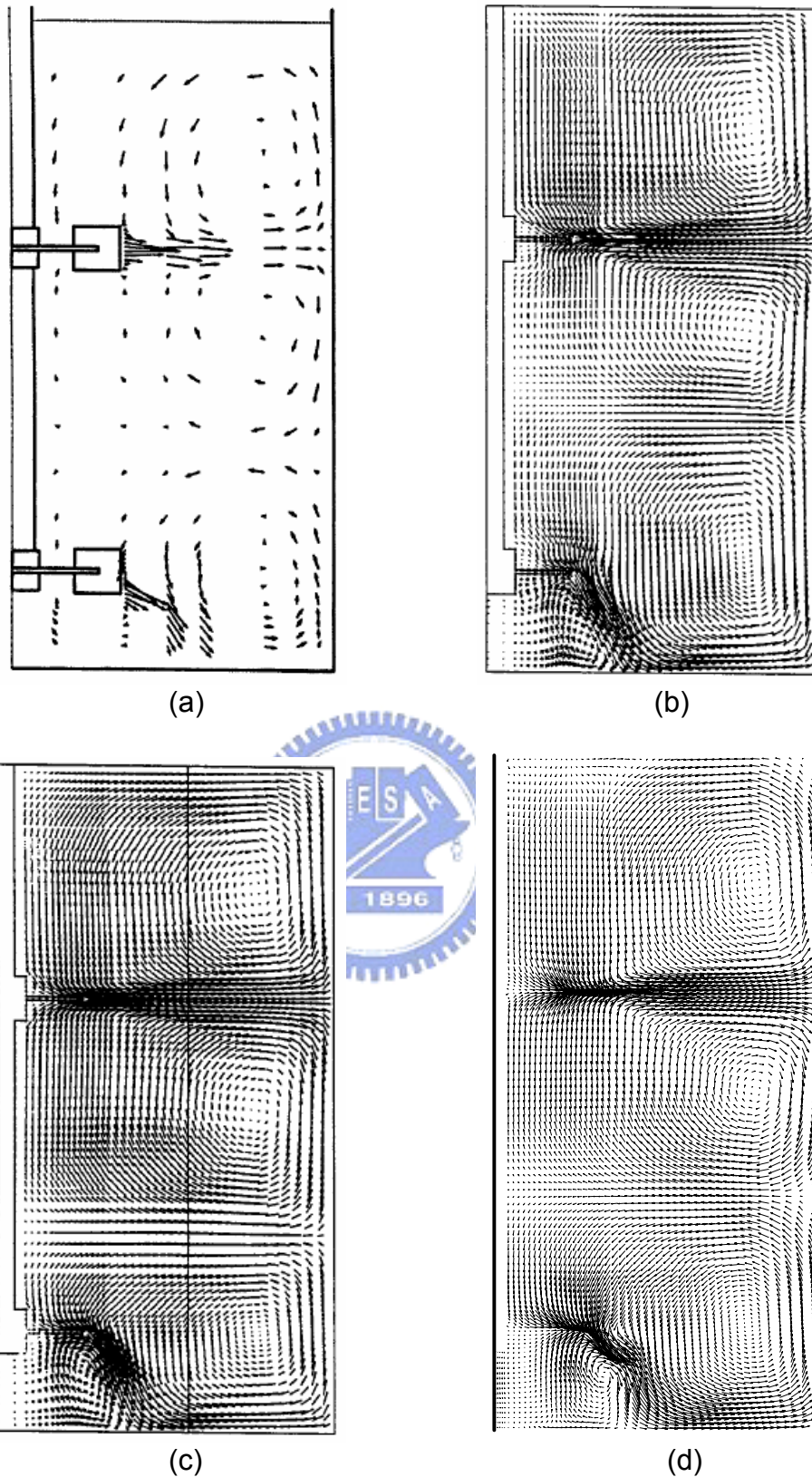


Figure 5.9 Diverging flow: comparison of velocity vector plots in a plane midway between baffles. (a) Experimental results [9] (b) Predictions, IO technique [22] (c) Predictions, SG technique [22] (d) Predictions, MRF technique (present)

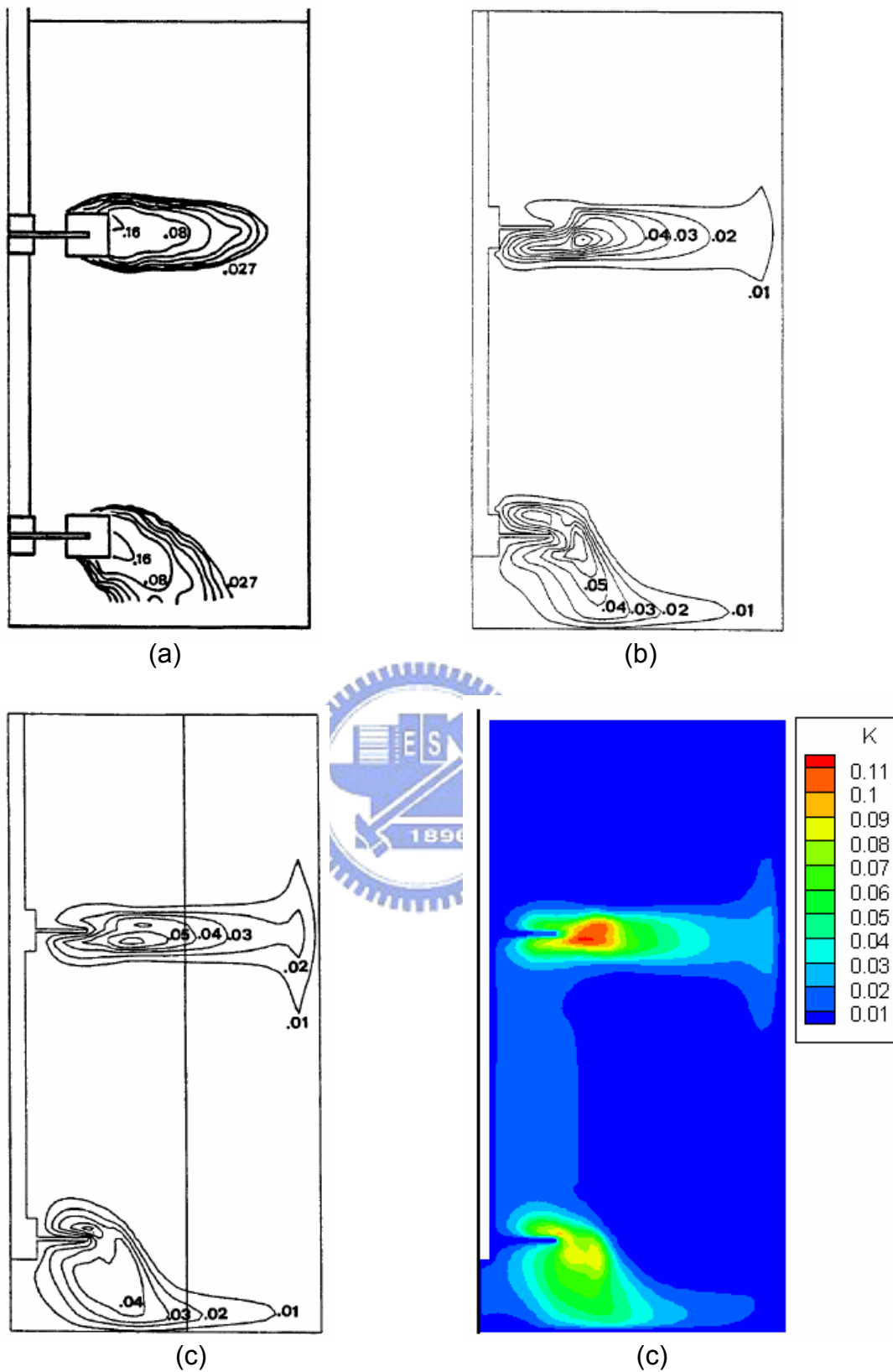


Figure 5.10 Diverging flow: Comparison of turbulence energy distributions in a plane midway between baffles. (a) Experimental results [9] (b) Predictions, IO technique [22] (c) Predictions, SG technique [22] (d) Predictions, MRF technique (present)